UNIVERSITY OF SOUTHAMPTON

Probing the System Parameters of Cataclysmic Variable Stars

Rachel Caroline North

A thesis submitted for the degree of Doctor of Philosophy

FACULTY OF SCIENCE
DEPARTMENT OF PHYSICS AND ASTRONOMY

February 2001

Errata

North, R. C. 2001

A thesis submitted for the degree of Doctor of Philosophy

Page 13. Corrected y-axis label of Figure 1.5 to 'normalised Flux'.

Page 14. Word 'disc' corrected to 'companion'.

Page 15. Inserted equation (1.23) for clarity.

Page 15. Inserted missing sin i factor into equation (1.11).

Page 28. Inserted 'Note μ is defined as '$M_1 = \mu(M_1 + M_2)$' into the caption of Figure 1.13.

Page 33. '$\sim v_K$' corrected to '$\sim \tau dyn$'.

Page 36. Corrected the descriptions of the accretion disc state in outburst and quiescence. 'Hot, low-viscosity state' was changed to 'hot, viscous state' and 'cool, viscous state' became 'cool, low-viscosity state'.

Page 46. Corrected '0.05' to '0.005'.

Page 53. Inserted 'This was' after 'analyses.' and before 'unfortunate'.

Page 76. Added footnote 'Inclination value taken from the literature, our preferred value is determined in section 3.2.4.' to Table 3.2.

Page 116. 'Values' replaced with phrase 'Corrections to apply to the heliocentric γ-velocities'.

Page 117. 'Values' replaced with 'Values for the γ-velocities'.

Page 121. Added ^{2} sign to 'NS^2/σ'.

Page 124. Replaced the phrase 'similar in magnitude to that of SU UMa-type dwarf novae' with 'smaller in magnitude even than those of SU UMa-type dwarf novae'.

Page 128. Replaced 'start of the outburst' with 'end of outburst'.

Page 157. Added 'Velocities of the white-dwarf, mass donor and centre-of-mass of the system are marked with crosses. Open circles denote (in units of 0.1 R_{L_1}) the path of the gas stream. The rings marked on the Doppler maps represent the outer disc velocity for a disc of size $0.8R_{L_1}$' to caption of Figure 6.2 for clarity.

Page 158. Replaced '392 $\mathrm{km\,s^{-1}}$' with '430 $\mathrm{km\,s^{-1}}$'.

Page 164. Added missing 'sin i' factor to equation (1.11).

Page 169. Removed irrelevant paragraph.

Page 173. Replaced 'spurious' with 'different'.

UNIVERSITY OF SOUTHAMPTON

ABSTRACT

FACULTY OF SCIENCE

DEPARTMENT OF PHYSICS AND ASTRONOMY

Doctor of Philosophy

PROBING THE SYSTEM PARAMETERS OF CATACLYSMIC VARIABLE STARS

by Rachel Caroline North

Cataclysmic Variables (CVs) are close binary stars in which a low mass star is losing material onto its companion, a white dwarf, via an accretion disc. This thesis presents an analysis of the optical spectra of these objects.

New orbital parameters are presented for a particular system, EM Cygni, which was previously thought to contain a white dwarf accreting material from a more massive companion, a dynamically unstable configuration which should not have existed according to theory. The new parameters remove the instability, which was due to spectral contamination from a third star, but introduce a further dilemma; is this third star physically associated with the CV?

Accurate centre-of-mass velocities are calculated for four CVs as an initial step towards completing a full statistical analysis of this parameter for the CV population. These are to be used as a direct test of the magnetic braking mechanism, an essential part of the present theory describing CV evolution.

Measurements of the outer velocities of the accretion discs in Dwarf Novae (DN, a subclass of CVs) and in a related group of interacting binary stars the Soft X-ray Transients (SXTs), are analysed to compare with the theoretical predictions. This tests whether observations of SXTs support the irradiation model created to explain the outbursts in these systems. Initial results suggest the observations present difficulties for the irradiation model, as no discs are seen close to the theoretical circularisation limit as is predicted from this theory.

Finally, the technique of Doppler tomography is applied to the Balmer Hα emission from long-period quiescent DN to discern its origins and to obtain accretion disc parameters. None of the resulting Doppler maps appear as predicted, reasons for this are discussed.

Contents

List of Figures

List of Tables

Acknowledgements

My first note of thanks must go to my supervisor, Dr. Tom Marsh, for putting up with my stupid questions for three years, and for really getting me motivated again about astronomy when it mattered. Thanks to the University of Southampton, for providing me with money to live on whilst researching this tome, and for having a good Astronomy group with a nice atmosphere! That made the transition much easier. Thanks also to PATT for most of my observing experience, Dr Pierre Maxted for sharing most of it with me, and to the European TMR network for getting it started in the first place!

I am now forever indebted to Garrath, without whom I think I might have gone slowly mad through the final months (perhaps I did?), and who put up with an awful lot whilst I faffed about writing this thing. We can start having some fun now! I just hope I'll be able to repay the debt in this lifetime... Secondly, enormous thanks to my Mum and Dad, for never questioning my decisions even though I didn't just get a '*normal*' job.... I know you must have wondered what on earth I was thinking at times. Sometimes, I did too. Cheers Hannah, for keeping my feet on the ground and making me laugh, and Katie, thanks for all the teasing, and your support of course! Gran and Grandad, much love and thanks for your support too.

My poor office mates also deserve a mention, for distracting me at regular intervals, in order that I didn't go blind from the stress. Special thanks to Dr. Luisa Morales-Rueda; those helpful discussions were a success at stress relieving, even when that wasn't the aim...

Chapter 1

Introduction

Summary

Cataclysmic Variable stars are interacting binary stars in which one of the stellar components (a late spectral-type star, hereafter mass donor) is losing mass onto its companion (a white dwarf). The mass transfer occurs through the inner Lagrangian point of the potential field, but due to the high angular momentum of the gas leaving the mass donor, the material cannot fall directly onto the white dwarf and instead forms an accretion disc around it. The presence of the accretion disc causes many of the visible characteristics of these objects which are used to classify them. In this thesis I will be exploring the general parameters of a particular subset of these objects, dwarf novae (DN), and using this information to determine the level of support the observations give to the theories.

In this chapter Cataclysmic Variable stars are introduced and the effects that each component of the system has on their behaviour and appearance are discussed. I will then go on to introduce the content of the subsequent five chapters, and present background information and theory relevant to their content. Methods which are used throughout this thesis to determine physical parameters, such as stellar masses

and outer-disc velocities, are described here.

Chapter 2 discusses the observations which were obtained and describes the various data sets, giving reasons why certain procedures were followed. It also provides an insight into the data reduction methods, and problems which were overcome.

The scientific results start in **Chapter 3** with the presentation of data which solve the mystery surrounding the enigmatic dwarf nova, EM Cygni. From previous radial-velocity measurements, the conclusion was drawn that the white dwarf was less massive than the mass losing star, a situation which according to the theory should have been dynamically unstable. The better resolution of this data revealed the presence of a contaminating spectrum due to another late-type star, and once this was removed, so was the dynamical instability (calculated from the radial velocities). This work has been published in the journal *Monthly Notices of the Royal Astronomical Society*

Chapter 4 presents the results of an initial project to try and accurately determine the centre-of-mass velocities for a selection of long-period dwarf novae. The motivation behind this project is to attempt to test directly the disrupted magnetic braking mechanism (currently assumed to be the explanation for the existence of the period gap in the orbital-period distribution of Cataclysmic Variable stars) using a method which is independent of the observational selection effects which plague comparisons between observations and theory in the CV regime. Current theory (Kolb and Stehle, 1996) predicts that the objects below the period gap ($P_{\rm orb} < 2\,{\rm hr}$) are older than those above it ($P_{\rm orb} \gtrsim 3\,{\rm hr}$).

In **Chapter 5** a compilation of parameters from the current literature is analysed to determine whether the irradiated disc model of King & Ritter (King and Ritter, 1998) is supported by observations. Many of the results used have been deduced from observations described in this thesis, and are described. A prediction of the

expected observations given the current theory is presented, and then a plot of the actual results follows with a discussion of the implications for the theory.

Chapter 6 concentrates on analysing the $H\alpha$ emission from the objects studied in Chapters 3 and 4. Doppler tomography is used as a method to map the emission, and deduce its origins. Measurements of the outer velocity of the accretion discs are attempted, however these lead to apparently sub-Keplerian motions. The unusual Doppler images which result are discussed and potential mechanisms which could explain their appearance are presented.

Finally, **Chapter 7** reviews each chapter of results and presents potential future work.

1.1 Cataclysmic variable stars

Cataclysmic Variable stars (hereafter CVs) are short period ($78\,\mathrm{min} < P_{\mathrm{orb}} < \sim 5\,\mathrm{days}$) interacting binary stars. Figure 1.1 indicates the standard components which are assumed to constitute the binary star (Robinson, 1976). Due to the fact that the mass donor (indicated on Fig. 1.1 as 'cool star') is overfilling its Roche lobe, matter is being lost to the white dwarf out through the inner Lagrangian point of the potential field.

The mass donor is co-rotating with the binary star, and at the point where the stream of gas thrown out by the mass donor hits the accretion disc, a shock-heated region of emission is created at the disc edge, usually referred to as the bright spot, or hot spot. The white dwarfs in CVs typically have masses of $\sim 0.5-1\,M_{\odot}$ (Warner, 1995), although they tend to be dependent on the orbital period of the system. Their radii are around one hundredth of the solar radius. The radii of the mass donors (assuming they are main-sequence stars) should range from $\sim 0.3 - 0.9\,R_{\odot}$, with corresponding masses $0.2 - 0.8\,M_{\odot}$ (Allen, 1973). The binary separation, a, defined

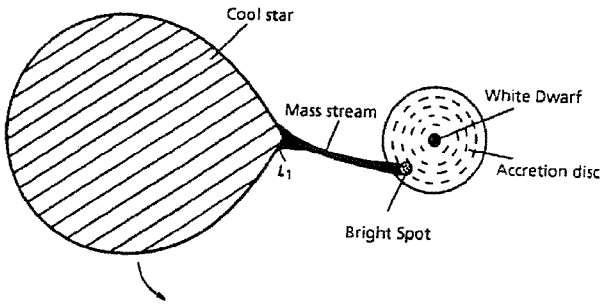

Figure 1.1: A schematic of a standard CV. From Robinson (1976)

as the distance between the centres-of-mass of the two stars is of the order of a few solar radii in CVs. Equation 1.1 gives a (in solar radii) as a function of the white dwarf mass, M_1, the orbital period, $P_{\rm orb}$, and the mass ratio, q, which is defined here as, and used hereafter in this thesis to mean $q = M_2/M_1$.

$$\frac{a}{R_\odot} = 0.506 \left(\frac{M_1}{M_\odot}\right)^{1/3} (1+q)^{1/3} \left(\frac{P_{\rm orb}}{1{\rm hr}}\right)^{2/3} \tag{1.1}$$

Equation 1.1 is derived from Kepler's third law, which states that the cube of the orbital separation is proportional to the square of the orbital period.

1.2 Classification of CVs

Semi-detached interacting binary stars, where the accretion is onto a white dwarf, fall naturally into four subclasses of object which are classified on the observed behaviour of the light curves, and spectroscopic characteristics. Figure 1.2 shows the subclasses of non-magnetic CVs. Starting from the extreme left of Fig. 1.2, the first subgroup of CVs are **dwarf novae**. This group consists of systems which experience a temporary increase in brightness of amplitude typically 2–5 visual magnitudes. This luminosity increase is connected to the behaviour of the accretion disc. In this high state (outburst) the disc is large and hot. These outbursts are thought to be initiated by a disc instability (see section 1.7.2). In between successive outbursts

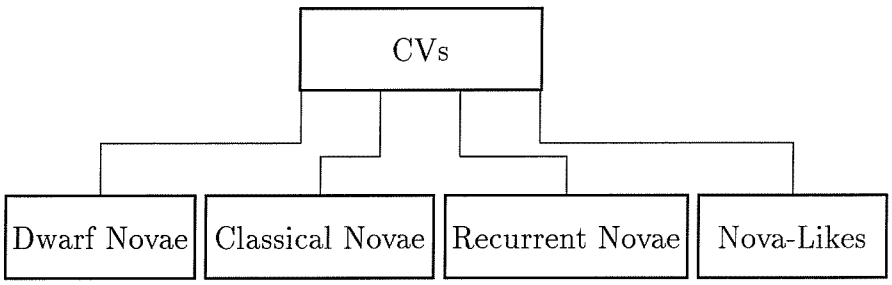

Figure 1.2: The subclasses of 'non-magnetic' CVs

they experience cool disc states (referred to as quiescence). Each object has a specific time scale on which the disc outbursts recur. Typical recurrence times for outbursts are of the order tens of days to tens of years. The duration of each outburst is of the order two to twenty days, and is correlated with the recurrence time. The light curves of dwarf novae in outburst were used to further subdivide the group, although the patterns which emerged can be attributed to the effects of different physical parameters which tend to control the behaviour of each subgroup. The groups are:

SU UMa types: These objects occasionally undergo *superoutbursts* during which the star achieves a brighter magnitude than in a 'normal' outburst (by about 0.7 magnitudes). They remain in superoutburst for approximately five times as long as the duration of a normal outburst. The SU UMa stars are short-period ($P_{orb} <$ 2 hours) systems.

Z Cam types: Z Cam subtypes experience longer periods of time when the system

appears to be stuck in a semi-high state (approximately 0.7 magnitudes lower than outburst levels) for a period of perhaps tens of days to years. During this time no outbursts are seen. All of the known Z Cam examples have orbital periods longer than three hours.

U Gem types: This category encompasses every other dwarf nova.

Classical novae (CN) are those systems which have only had one observed eruption. The change in brightness observed in the object from before identification to at maximum light ranges from six to about nineteen magnitudes. The mechanism of energy release in classical novae is also different to that in dwarf novae. In classical novae, the more explosive outburst is caused by a thermonuclear runaway due to the deposition of hydrogen-rich material onto the white dwarf.

Recurrent Novae (RN) are just those objects which having been classified as classical novae, were then observed undergoing another outburst. The difference between RN and DN is made spectroscopically: RN show signs of shell-loss.

Nova-like variables (NL) include all the non-eruptive CVs. In other words, all the pre-novae, post novae and even Z Cam-type DN. For these variables our baseline of observations (typically in the region of 50-100 years, maximum) is perhaps too short to reveal any cataclysmic events. This group can be further subdivided into three classes of object (Warner, 1995). The first is the UX UMa subgroup, which have persistent broad Balmer absorption spectra. Those nova-likes which do not show this absorption, and whose spectra consist of Balmer emission lines (which may have sharp absorption cores to them) are denoted the RW Tri subset. The SW Sex stars were introduced as a subclass by Thorstensen et al. (1991). These are highly inclined NL which show large phase lags in the emission lines compared to photometric conjunction. The emission lines themselves are only single-peaked, which is unusual for eclipsing systems. The strength of the He II λ4686 emission line is also comparable to that of Hβ. They show transient absorption events at phases when the side of the mass donor facing the white dwarf is visible. Recently, LS

Pegasi (Martinez-Pais et al., 1999; Taylor et al., 1999) and V795 Herculis (Casares et al., 1996; Dickenson et al., 1997) have been cited as possible examples of low inclination SW Sex objects.

In addition to the non-magnetic CVs illustrated in Fig. 1.2, there are examples of this type of interacting binary in which the magnetic field on the white dwarf plays an important role in the constitution and development of the system. **Magnetic CVs** are usually (rather dubiously) included in the nova-like category. They can be split into two definite subclasses; the polars and intermediate polars. The presence of a strong magnetic field on the white dwarf interferes with the disc-forming process and so either no disc is formed (for the case of polars) and the material accretes directly down the magnetic field lines onto the poles of the white dwarf, or the disc is truncated at its inner edge (in the case of intermediate polars) where the magnetic field of the white dwarf begins to dominate.

This thesis concentrates on optical spectroscopy of dwarf novae. Chapter 3 focuses upon an enigmatic example, EM Cygni, which was previously assumed to be in a state of unstable mass transfer. Chapters 4 & 6 concentrate on analysing data from dwarf novae with longer orbital periods, whilst Chapter 5 uses data collected for dwarf novae with a wide range of orbital periods to compare with data from another class of interacting binary stars, the Soft X-ray Transients, similar to Dwarf Novae in every respect bar the accretor: a black hole (see Section 5.1).

1.3 Roche lobe overflow

So, why are CVs described as interacting binary stars? Stellar evolution dictates that as stars pass through their life cycle their physical parameters, such as masses and radii, will change. Binary stars are not immune to this behaviour. Both components of the binary system will be independently evolving, a fact which can affect the

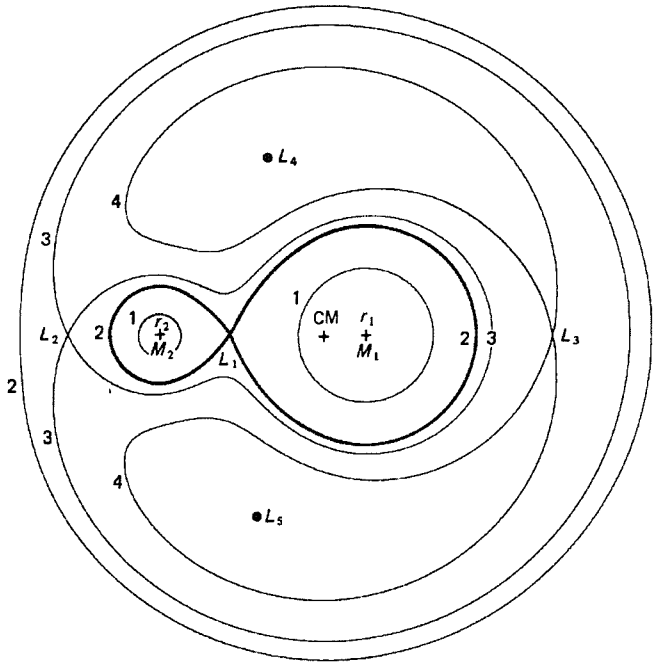

Figure 1.3: Roche equipotentials in the orbital plane for a system with a mass ratio of 0.2. From Frank, King & Raine (1985)

binary system as a whole. Once the binary has developed to the point where one star has evolved to a white dwarf – whilst the other one is still on or near the main-sequence – then other forces come into play which affect the subsequent evolution of the system. The stars in the binary system are orbiting each other so closely that one is affecting the outer material of the other, and then Roche lobe overflow may occur. This situation is seen in CVs. There are many parallels in astronomy, and indeed the pioneer of this work, Edouard Roche, used it to test the longevity of planetary satellites. The Roche approach considers the orbit of a test particle in the combined gravitational field of two mutually orbiting bodies. The assumption is made that the mass of the test particle is negligible compared to either of the other two bodies. In addition, the orbits are assumed to be circular. This is a good approximation for CVs since the proximity of the two stars means that tidal forces eliminate any orbital eccentricity.

Figure 1.3 shows a slice through the gravitational potential field in the orbital

plane of the binary system. The lines shown are those of constant potential (Φ_R). The centre-of-mass of the binary star is marked with a cross, and the points marked L_1 to L_5 are the Lagrange points of the potential field. The inner Lagrangian saddle point behaves as a spout between the Roche lobes surrounding each star, enabling material to flow from one to the other. L_2 is the outer Lagrangian point, another point where $\partial\Phi_R/\partial x = 0$. It lies on the largest closed equipotential for a contact binary system. L_4 and L_5 are local maxima of the potential field (the so-called Trojan asteroid points, which are only stable for extreme mass ratios). The equipotentials are labelled 1 to 4 in order of increasing potential. The position of the inner Lagrangian point on the line joining the two stars can be calculated from the aspect of the white dwarf using the relation (Silber, 1992)

$$\frac{R_{L_1}}{a} = (1.0015 + q^{0.4056})^{-1} \qquad 0.04 \leq q \leq 1. \tag{1.2}$$

Equation (1.2) is accurate to closer than one per cent.

Gas flow between the two stars is governed by the Euler equation (1.3).

$$\rho\frac{\partial \mathbf{v}}{\partial t} + \rho\mathbf{v}.\nabla\mathbf{v} = -\nabla P + \mathbf{f} \tag{1.3}$$

For the case of a CV, it is convenient to write this in a form which accounts for the rotation of the binary star; rewriting it in a frame of reference which is itself rotating with the CV. This simply introduces terms into equation (1.3) which account for the Coriolis and centrifugal forces present in the rotating frame.

$$\frac{\partial \mathbf{v}}{\partial t} + (\mathbf{v}.\nabla)\mathbf{v} = -\nabla\mathbf{\Phi_R} - 2\mathbf{\Omega} \wedge \mathbf{v} - \frac{1}{\rho}\nabla\mathbf{P} \tag{1.4}$$

The second term on the right-hand side (RHS) of equation (1.4) is the Coriolis force per unit mass. The gravitational and centrifugal forces are both included in the first

term on the RHS of equation (1.4). Φ_R is the Roche potential and is described by

$$\Phi_R(r) = -\frac{GM_1}{|\mathbf{r}-\mathbf{r_1}|} - \frac{GM_2}{|\mathbf{r}-\mathbf{r_2}|} - \frac{1}{2}(\mathbf{\Omega} \wedge \mathbf{r})^2 \tag{1.5}$$

where $\mathbf{r_1}$ and $\mathbf{r_2}$ are the position vectors of the centres of the two stars. The shape of the equipotentials is ruled purely by the mass ratio, q. For material at a large distance from the binary ($r \gg a$) the equipotentials are just those of a point mass viewed in a rotating frame. For material orbiting closely to either $\mathbf{r_1}$ or $\mathbf{r_2}$, the controlling gravitational field is that of the star which it is closest to. Hence, a deep potential well exists around each star, influencing material located there. The heavy line drawn in Fig. 1.3 is the figure-of-eight equipotential which connects the potential wells of each star. The part of this line surrounding each star is called its *Roche Lobe.* The point where one lobe meets the other is called the inner Lagrangian point, L_1, which is a saddle point of Φ_R. Basically, this means that if material is located near L_1 then it will find it easier to pass through into the other Roche lobe than to escape the 'critical surface' altogether. In CVs, one of the stellar components has reached its critical Roche surface, and so material is spilling through into the Roche lobe of its companion and accreting on to it. There are three scenarios in which Roche lobe overflow (RLOF) can occur. Case A RLOF involves a star which is still burning hydrogen on the main-sequence at the time it comes into contact with its Roche lobe. This is the case for CVs, and for all the objects discussed in this thesis. Alternatively there are Case B Roche lobe overflow (where the star filling it's Roche lobe has ceased to burn hydrogen in its core, but has not yet ignited core-helium burning) and Case C overflow, which covers those stars which are burning helium in their cores at the point when they come into contact with their Roche lobes. Late Case-C overflow is used to describe stars which have already started shell helium burning when they come into contact with their Roche lobe.

Calculations of the size of the Roche lobes around each star can only be solved numerically, due to the form of equation (1.5). However, approximations have been developed; see equations (1.2) and (1.8), for example. The size of the Roche lobe

around the mass donor can be determined as follows. Due to the transfer of mass and the proximity of the two stars, the shape of the mass donor is distorted from purely spherical. Its shape is affected by two factors, its rotation (which flattens it along its rotation axis) and the tidal force which stretches it towards its companion along the line joining the two stars. A good estimate of the radius of the mass donor can be found from the volume radius of the Roche lobe. Calculations of the volume radius of the Roche lobe can be made using the formulae of Paczynski (Paczynski, 1971) which state that

$$\frac{R_L(2)}{a} = 0.38 + 0.20 \log\, q \qquad 0.3 < q < 20 \tag{1.6}$$

and

$$\frac{R_L(2)}{a} = 0.462 \left(\frac{q}{1+q}\right)^{1/3} \qquad 0 < q < 0.3 \tag{1.7}$$

Eggleton (1983) deduced that the volume radius of the Roche lobe of the mass donor can be approximated using

$$\frac{R_L(2)}{a} = \frac{0.49 q^{2/3}}{0.6 q^{2/3} + \ln(1 + q^{1/3})}, \qquad \text{for } 0 < q < \infty. \tag{1.8}$$

Equation (1.8) is accurate to better than one per cent over the full range of mass ratios and it allows an estimate of the mean density of the mass donor to be calculated using

$$\overline{\rho} = \frac{3M_2}{4\pi R_L^3(2)}. \tag{1.9}$$

This can be useful for determining whether the main-sequence assumption made for the mass donors of many CVs is a valid one. For those systems with $1 < P_{\rm orb} < 10$ hours, equations (1.8) and (1.9) show that stars with densities typical of those on main-sequence can indeed fill their Roche lobes. Those systems with $P_{\rm orb} > 10\,{\rm hr}$ must contain an evolved mass donor.

1.4 Spectra from cataclysmic variables

Many physical parameters can be deduced from spectroscopic observations. In this thesis, optical spectroscopy (see Chapter 2 for full details) is used to determine accurate system parameters for a selection of Cataclysmic Variable stars. Chapter 3 uses spectroscopy of EM Cygni to investigate its potential triple-system nature. Chapter 4 uses spectra to attempt to directly test the disrupted magnetic braking hypothesis which is used to explain the existence of the period gap in the orbital-period distribution of CVs (see Section 1.6). Chapter 5 uses spectroscopic parameters collected from the literature (and observations) to see whether optical observations support particular models for Soft X-ray Transient outbursts. Finally, the parameters determined from the spectra are used in Chapter 6 to construct Doppler images of the accretion discs in the observed systems.

Spectra of CVs are composite in nature. Different components of the CV dominate in different objects. The white dwarf contributes a broad Balmer absorption-line spectrum, and manifests itself more obviously at shorter wavelengths whilst the mass donor prefers longer wavelengths and appears as a narrower absorption line spectrum, molecular bands, and sometimes chromospheric emission lines. The accretion discs dominate the optical light from CVs, and to the spectra they provide wide double-peaked emission lines (see Section 1.4.1) in quiescence, whilst in outburst they contribute broad absorption (see Figs. 1.4 & 1.5). The disc also provides the blue continuum. The impact region between the gas stream and the disc-edge manifests itself within the Balmer (and calcium) lines as a narrow emission component. Other parts of the binary star contribute most to the spectrum at other wavelengths. The optical region of the spectrum can be used to target information about the accretion disc and mass donor. Figure 1.4 shows the resultant spectrum from the dwarf nova SS Cyg at optical wavelengths whilst the system was in a quiescent state. Figure 1.5 shows a spectrum of SS Cyg whilst at outburst maximum (Morales-Rueda, 2001). The differences between the two spectra are obvious,

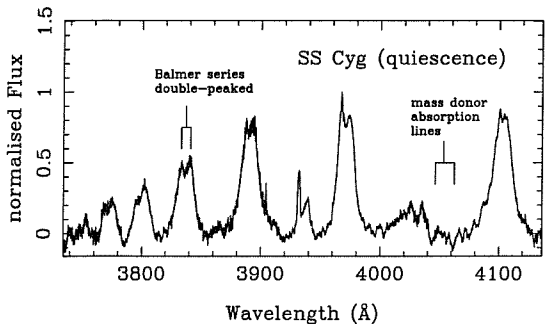

Figure 1.4: Example spectrum of a CV in quiescence. SS Cyg in the range $\sim 3730 - 4340$Å showing higher members of the Balmer series and Ca II H and K in emission, and absorption lines from the mass donor

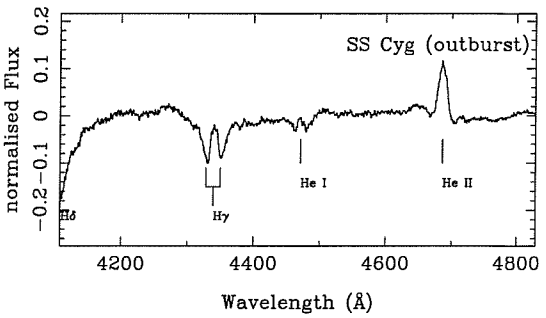

Figure 1.5: Example spectrum of a CV in outburst. SS Cyg in the range $\sim 4100 - 4800$Å. The Balmer series are now in absorption, as is He I. Spectrum provided by Morales-Rueda (2001)

and are due to the physical conditions which prevail in each state. In Fig. 1.4 the Balmer lines are in emission, and double-peaked. In the outburst spectrum $H\gamma$ has turned into an absorption line (with an emission core), and now He II emission is seen (which is apparently single-peaked: possibly due to a wind component). The increasing continuum quenches the emission lines, and absorption cores develop which have widths similar to the quiescent emission.

1.4.1 Emission line spectra in cataclysmic variables

If the vertical optical thickness in the continuum is less than one, but the thickness in the lines is significant, then an emission line spectrum occurs. Due to the low temperatures in the outer disc regions ($T < 7000$ K) hydrogen is mainly in its neutral state, which means that the continuum opacity from free-free and bound-free processes is low. The Balmer lines are assumed to be produced in local thermodynamic equilibrium (LTE) by an outer disc which is transparent in the Paschen continuum but opaque in the lines. The emission lines are superimposed onto a flat continuum, and are mainly from low ionization species, for example H I, He I, He II and Ca II. The excitation of the lines tends to increase with the mass transfer rate. These lines are thought to form in different regions of the disc, dependent on the physical conditions there. For example the He I emission in U Gem comes mainly

from the bright spot region (Honeycutt et al., 1987), and the Ca II emission in most CVs originates in the outermost, cooler parts of the disc (Persson, 1988). These emission lines are assumed to have an origin in the accretion disc for the following reasons. Firstly, their line widths, which are typically several thousand kilometres per second support a disc origin, and secondly, the double-peaked line profiles are characteristic of Doppler shifted flux from a rotating disc (Smak, 1981; Horne and Marsh, 1986). Line formation in accretion discs falls into two regimes which control the appearance of the line profile. The first is the **local** radiative transfer problem, which determines the spectral and angular distribution of emergent radiation from the disc surface. The **global** line profile is then created by summing these contributions whilst accounting for the Doppler shifts which appear due to the rotation of the disc as seen at the observer, and which have largest magnitude at the extremities of the disc. Orbital velocities in the disc are generally much greater than the speed of sound in the medium, and so this global Doppler broadening dominates over any local thermal broadening in the line profile. This has allowed an explanation for the double-peaked line emission seen in accretion discs without considering in depth the local radiative transfer problem. The double peaks are just symptomatic of a rotating disc (see Fig. 5.3 and section 5.4). Eclipsing CVs are useful for determining the location of emission-line producing regions. If the emission line being analysed shows an eclipse, then the place of emission can be constrained to lie near the orbital plane of the binary, somewhere which disappears behind the disc around phase zero (see Chapter 3).

1.4.1.1 Information about accretion discs from line profiles

Spectral line profiles are important in that many physical parameters can be deduced both from their appearance and their kinematic behaviour. Measurements of the peak separations in the emission lines from accretion discs give an indication of the

outer disc velocity

$$v_K(r_d)\sin\,i = (0.95 \pm 0.05)V_d(I_{max}) \tag{1.10}$$

where $v_K(r_d)$ is the velocity at the outer edge of a disc, with radius r_d. $V_d(I_{max})$ is the velocity of the points of maximum intensity in the double-peaked profile. Knowing that $q = M_2/M_1 = K_1/K_2$ then

$$M_1 = \frac{K_2}{K_2 + K_1}(M_2 + M_1)$$

Substituting this into equation (1.23) $[v_K(r) = (GM_1/r)^{1/2}]$ gives

$$v_K(r_d) = \left(\frac{GK_2(M_1 + M_2)}{(K_2 + K_1)r_d}\right)^{1/2}$$

From Kepler's third law, $(M_1 + M_2) = \Omega^2 a^3/G$, so

$$v_K(r_d) = \left(\frac{GK_2\Omega^2 a^3}{G(K_2 + K_1)r_d}\right)^{1/2}.$$

Therefore, since $\Omega a = (K_1 + K_2)/\sin i$, provided measurements of the radial velocity amplitude from both absorption and emission lines are available, then the predicted projected Keplerian velocity of the outer edge of the disc can be calculated using

$$v_K = \sqrt{K_2\,(K_2 + K_1)}\left(\frac{a}{r_d}\right)^{\frac{1}{2}}. \tag{1.11}$$

Accretion disc spectra also vary according to the optical properties of the gas which makes up the disc. Figure 1.6 (Horne and Marsh, 1986) shows synthetic emission line profiles calculated for a) optically thin emission lines at various inclination angles, and b) optically thick emission lines at the same inclination angles. The Keplerian velocities at the inner and outer edges of the disc are $2200\,\mathrm{km\,s^{-1}}$ and $700\,\mathrm{km\,s^{-1}}$ respectively. The profiles have been convolved with a Gaussian to simulate an instrumental profile (of magnitude $150\,\mathrm{km\,s^{-1}}$). The main difference between the two sets of line profiles is the shape of the valley between the double

peaks. In the optically thin case, the valley is U-shaped, whereas for the optically thick case that valley is V-shaped (Horne and Marsh, 1986). In quiescence, the inner part of the accretion disc ($r < 1 \times 10^{10}$ cm) in dwarf novae is generally optically thin (Warner, 1995) whilst the rest of the disc is optically thick. At sufficiently high

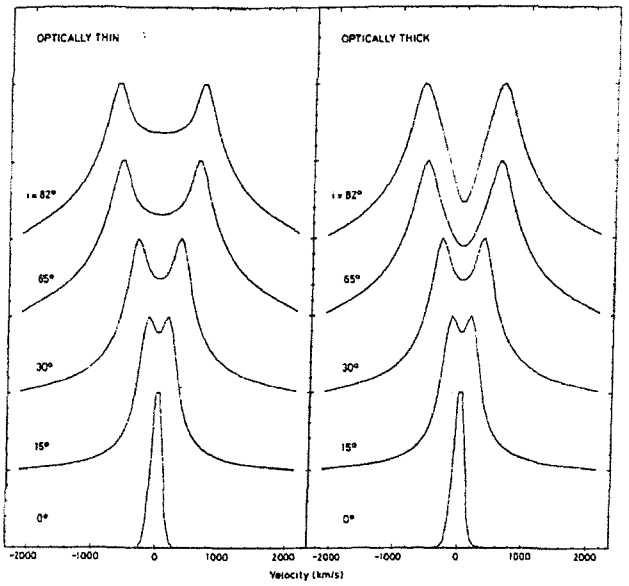

Figure 1.6: Synthetic line profiles from optically thin and optically thick emission lines. From Horne & Marsh (1986)

inclinations, however, the accretion disc is optically thick in the continuum and so the emission lines are expected to be weak. This is not observed to be the case, so optically thin emission is not enough to account for the lines in low $\dot{M}(d)$ binaries.

1.4.2 Absorption line spectra

Mass donors in Cataclysmic Variables can be studied through an absorption line spectrum, and/or chromospheric emission lines. The absorption line spectrum is similar to that from single K- or M-dwarf stars. However, the absorption lines from the mass donor in CVs are usually rotationally broadened (to a value somewhere in the region of $100\,\mathrm{km\,s^{-1}}$, because the rotation of the star is tidally locked to that of the binary system) whilst those lines from field stars are usually quite narrow, and

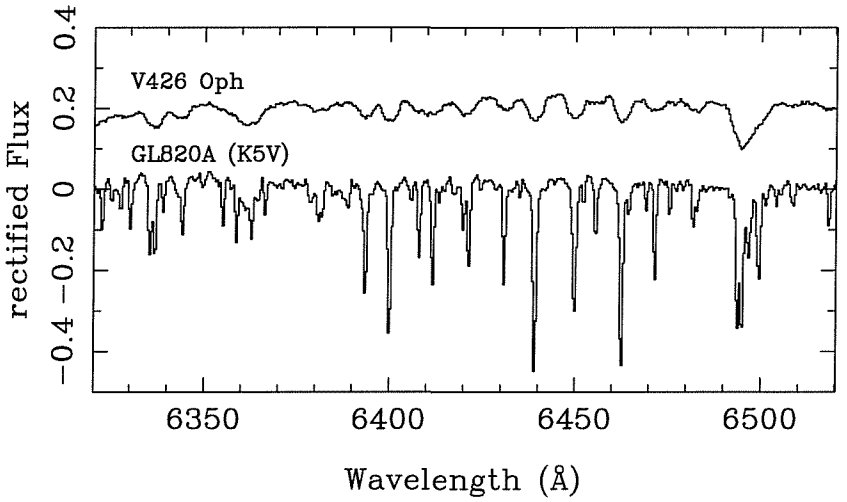

Figure 1.7: Absorption lines from low mass stars. The top spectrum (V426 Oph) illustrates how the absorption lines from the mass donor in CVs are more broad than those in a field K-dwarf (GL 820A, bottom spectrum)

only broadened to 5 or 10 $\mathrm{km\,s^{-1}}$ (Fig. 1.7). The absorption lines seen in Fig. 1.7 are mainly from low ionization metal species, like Ca I and Fe I. The feature at $\sim$ 6495Å is a blend of lines from the two species, which require a higher resolution than that used here to separate them into individual lines. In CVs, the radial velocities of these lines change over time scales of minutes to hours following the orbital motion of the mass donor over a complete revolution. The difficulty with late spectral-type stars is that the spectral lines all crowd together, and may even disguise the true continuum because of their blending. This problem worsens with lower spectral resolving power. So accurate equivalent widths may not be attainable from absorption line spectra. In this thesis, the observations of single stars (standards) have been artificially broadened, in order to determine the amount of rotational broadening in the mass donors of the CVs. Across a spectral line profile the absorption coefficient changes, being larger towards the centre of the line. The place where the source function and the surface flux are equal ($\tau_\nu = \tau_1$) is true higher up in the atmosphere for frequencies nearer the line centre, and holds for progressively deeper layers for frequencies far into the wing. So the centre of the line comes from higher stellar layers than the wings. If the source function decreases outward through the stellar photosphere then an absorption line is formed. Photospheric velocity fields

can produce Doppler shifts which alter the depth at which the source function and surface flux are equal. Small scale motions can affect radiation transfer. Large scale motions and rotation produce line broadening mechanisms, altering the line profiles. In CVs, rotation is the dominant line-broadening mechanism in the absorption lines too.

1.5 Radial velocity curves and subsequent mass determinations

In Chapters 3 & 4 radial velocity variations are widely used as a tool for determining system parameters. This section will describe the variations expected to be seen in CV spectra, and detail the particular methods chosen for this thesis to determine variations. Plotting spectra in a two-dimensional fashion, with wavelength on the x-axis and time on the y-axis and representing the intensity variations as a greyscale allows the sinusoidal wavelength variations of the spectral lines to be seen (hereafter called trailed spectra). Time-resolved spectroscopy of CVs allows measurements of the variations in radial velocity of the spectral lines to be made. A trace of the orbital motion of the CV component being observed is then compiled, which reflects the variation from negative to positive velocities as the star moves around the binary star's centre-of-mass. Due to the relatively short orbital periods of these objects a whole revolution can be observed in one night.

The radial velocity amplitude can be expressed via the following two equations:

$$K_1 = \frac{2\pi a \sin i}{P_{\rm orb}} \left(\frac{q}{1+q} \right) \tag{1.12}$$

$$K_2 = \frac{2\pi a \sin i}{P_{\rm orb}} \left(\frac{1}{1+q} \right). \tag{1.13}$$

K_1 and K_2 correspond to the radial velocity amplitudes of the white dwarf and

mass donor respectively. K_2 can be measured by observing the absorption lines from the mass donor over an entire orbital period. However, not all CVs are double-lined spectroscopic binaries (Ritter and Kolb, 1998), and so measurements can only be made with those objects in which contributions to the spectra are made by the mass donor too (see Appendix A). The radial velocities measured from the absorption lines due to the mass donor vary sinusoidally over the course of an orbital revolution, and in the case of CVs, can be fit assuming a circular orbit solution

$$v_R(t) = \gamma + K \sin \frac{2\pi(t - t_0)}{P}. \tag{1.14}$$

By doing this, a precise orbital period for the system can be deduced and therefore accurate phasing applied. Accurate phasing is useful when Doppler tomography (see Chapter 6) is to be used to image accretion discs in CVs, as it enables an accurate picture of the disc parameters to be extracted. Deducing K_2 can also lead to a determination of the mass of the compact object in the binary star. This is done using the mass function for the compact object, $f(M_1)$

$$f(M_1) = \frac{P_{\rm orb} K_2^3}{2\pi G} \equiv \frac{M_1 \sin i^3}{(1+q)^2}. \tag{1.15}$$

K_2 and $P_{\rm orb}$ are measured, and then values for the inclination, i, and mass ratio, q used to determine M_1. A similar relationship exists to calculate the mass function of the mass donor from observations of the emission lines,

$$f(M_2) = \frac{P_{\rm orb} K_1^3}{2\pi G} \equiv \frac{M_2 q^2 \sin i^3}{(1+q)^2}. \tag{1.16}$$

An estimate for K_1 can be made using the emission lines which originate at the accretion disc (see Section 1.4.1.1). The accretion disc is assumed accurately to reflect the white dwarf motion. However, asymmetries in the emission lines can disturb measurements made using this method, and so inaccurate K_1 values result. For systems with a dominant bright spot, a narrow emission component which is not phased with the white dwarf can interfere hugely with measurements (Stover

et al., 1980). Schneider & Young (1980) developed a way of measuring the radial velocities of emission lines to account for this problem using a double Gaussian technique. The algorithm compares the emission line flux in two Gaussian bandpasses separated by a velocity interval S. The Gaussian bandpasses are described by their FWHM measurement, a. The resulting radial velocities can then be fit in the normal way with a sinusoid to represent the orbital motion. Plotting the resulting variables, namely $\Delta K_1/K_1$, ϕ_0 and γ, as a function of the separation used (known as a diagnostic diagram) allows selection of the value of S which obtains the closest value of K to the actual K_1. An alternative method is to use a *light centre diagram*, proposed by Marsh (1988). If the emission lines are distorted by the S-wave from the bright spot, then asymmetries will be introduced. If the disc is discussed in terms of velocity space (see Chapter 6), then an undistorted accretion disc will sit symmetrically around the $(0, K_1)$ point, the white dwarf velocity. Any bright spot interference will pull the light centre of the accretion disc towards the position of the bright spot. Using a larger Gaussian separation will reduce the contribution from the bright spot and so the light centre of the disc will be closer to the actual K_1 value, however the statistical noise increases appreciably here. The radial velocity curve $-K_x \cos\theta + K_y \sin\theta$ corresponds to a light centre (K_x, K_y), so the fit parameters K and ϕ_0 are plotted as $(-K \sin\phi_0, -K \cos\phi_0)$. A line joining the measured points can then be extrapolated to the K_y axis to deduce a value for the radial velocity amplitude of the white dwarf.

1.5.1 Determining mass donor radial velocities using cross-correlation

Chapters 3, 4 and 5 all make use of radial velocity curves determined using observations of absorption lines in CVs. The procedure chosen for this thesis is one based on the method used by Tonry & Davis (1979) to determine galaxy redshifts. To start with, reasons which could affect the quality of the results obtained are presented,

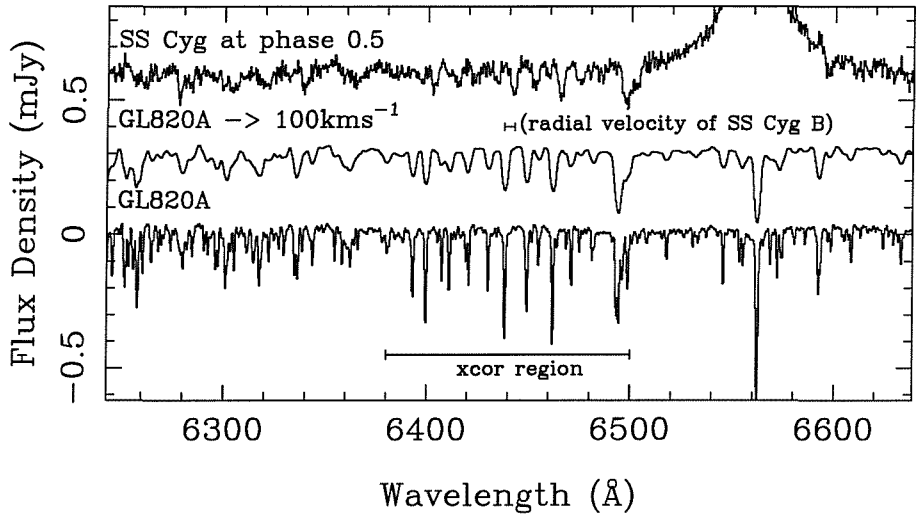

Figure 1.8: The radial velocity standard, GL 820A (bottom spectrum), artificially broadened to $100\,\mathrm{km\,s^{-1}}$ (middle spectrum). The average SS Cyg spectrum is shown (top spectrum) to show a) the broadness of the lines from the mass donor, and b) the shift of the absorption lines relative to those of the standard, due to the orbital motion of the mass donor.

and then the method chosen is described. The errors in the determination of K_2 are of a lesser magnitude than those in K_1 estimates, however certain processes do affect the fits obtained. For the radial velocity amplitudes of the mass donors, checks must be made to look for indications that the radial velocities are being affected by heating from the accretion disc/boundary-layer/white dwarf region. This effect, so-called 'irradiation', is much stronger in the soft X-ray transients discussed in Chapter 5 than in dwarf novae. However the panel which shows the radial velocity curve of V426 Ophiuchi in Fig. 4.7 betrays the presence of this effect, because of the departure of the data from the fit around phases 0.25–0.75. This effect can be diminished by cutting out the radial velocity measurements between these phases. With multiple orbit coverage, a good fit to the data points can still be obtained for the remaining phases.

The method used in this thesis to determine radial velocities for the mass donors uses the absorption lines which originate at the late-type star to obtain a measurement of their shift with respect to a radial-velocity standard star taken using the same instrument configuration. Figure 1.8 shows an example of a radial velocity standard (bottom), and a broadened version of itself (middle), compared with a CV

absorption line spectrum (top). The difference in radial velocity of the absorption lines between the standard and CV is indicated on the plot. The radial velocities can then be corrected for the radial velocity of the standard star and the Earth's orbital motion, in order to put them onto a heliocentric scale. Figure 1.9 shows the

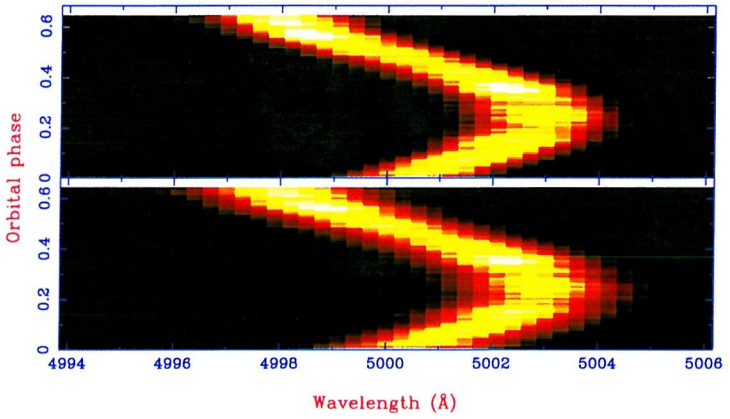

Figure 1.9: The cross-correlation functions plotted with time as the y-axis, to illustrate the radial velocity variations in SS Cyg

result of the cross-correlation procedure plotted with time on the y-axis, and shows clearly the sinusoidal motion of the mass donor, which is represented by a shift in position of the peaks of the cross-correlation functions. The top panel of Fig. 1.9 shows the cross-correlation functions resulting with a raw radial velocity standard. The bottom panel in Fig. 1.9 shows the resulting functions when the radial velocity standard is artificially broadened to match the rotationally broadened lines from the mass donor in SS Cyg ($\sim 100\,\mathrm{km\,s^{-1}}$). Figure 1.10 shows three out of the sixty-four cross-correlation functions used to produce Fig. 1.9, plotted in the form of spectra, with radial velocity on the x-axis and the correlation value on the y-axis. As is illustrated in Fig. 1.9, the measured radial velocities go from around zero at spectrum number one, out to around $200\,\mathrm{km\,s^{-1}}$ at spectrum twenty then back down to approximately -$150\,\mathrm{km\,s^{-1}}$ at spectrum number 64. These three spectra are shown in Fig. 1.10 to show the shape of the correlation peaks, and their variation in position.

This technique has the advantage that it can locate the spectrum of the mass donor even when it is not obvious to the eye. This is the case for the observations of AH Her in this thesis (Chapter 4), where the mass donor is not obvious in the spectrum until

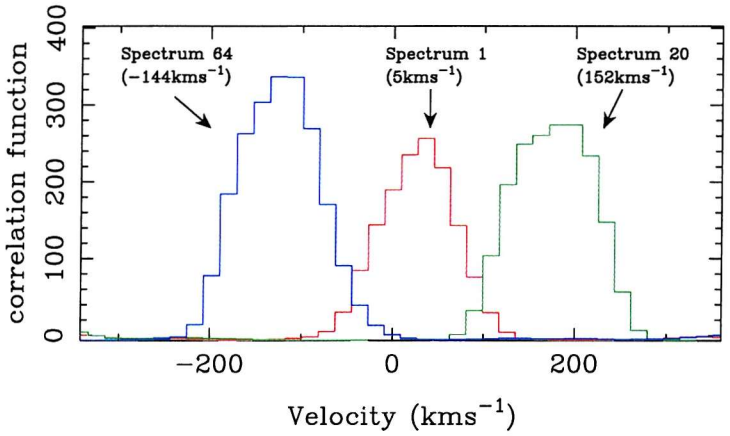

Figure 1.10: Three of the sixty-four cross-correlation functions plotted to illustrate the radial velocity variations in SS Cyg, and to show the correlation peaks

the individual exposures are Doppler-corrected for its motion, and then averaged.

1.6 The distribution of CVs with orbital period

In Chapter 4 I shall be examining a particular sample of dwarf novae, those with orbital periods above $P_{\rm orb} = 6$ hours to attempt to directly test CV evolution theory. In this section, I shall introduce the natural orbital-period arrangement of CVs, and comment upon the existence of various features within this distribution.

Non-magnetic CVs are clustered into two groups according to their distribution with orbital period, $P_{\rm orb}$. One of these has $\sim 1 < P_{\rm orb} \lesssim 2$ hours and the other has $P_{\rm orb} > 3$ hours (as can be seen in the top panel of Fig. 1.11). Orbital periods with lengths between two and three hours are sparsely populated, and those objects which do lie there tend to possess larger magnetic fields on their white dwarfs. The region where this dearth of objects appears is referred to as the **period gap** (King, 1988). The distributions shown in Fig. 1.11 are to some extent biassed by selection effects which operate on observations of CVs. Only one of these effects operates on the distribution within a given subgroup - the relative ease of detecting orbital brightness modulations in systems with $P_{\rm orb} \leq 6$ hours as compared to those with

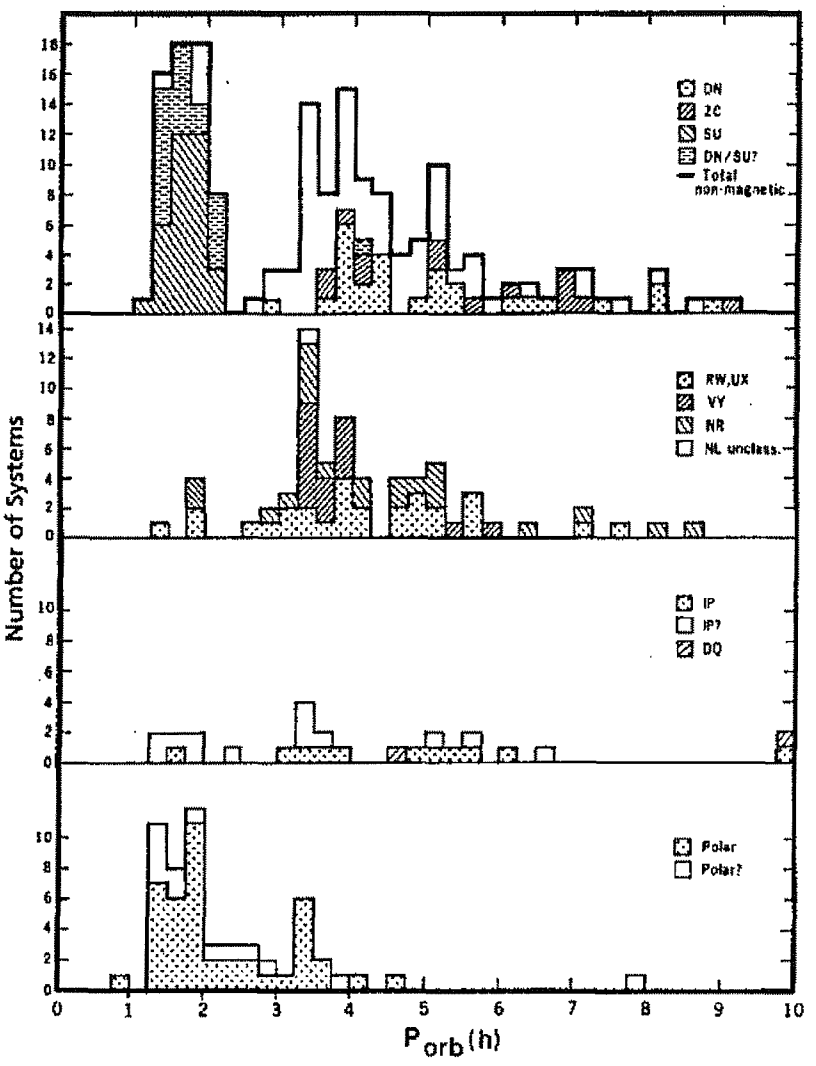

Figure 1.11: The orbital period distribution of CVs. From Warner (1995)

longer orbital periods. Other effects are related to the ease of detection of objects, for example, CN and DN can be easily classified due to their brightness variations whilst NL systems have to be discovered using survey techniques. In addition, researchers contribute to these selection effects by studying systems which are currently topical, for example most magnetic CVs are well studied.

The top panel in Fig. 1.11, which shows the distribution of dwarf novae with orbital period has a sharp lower cut-off at around 75 minutes. This can be understood from the response of a very low-mass mass donor to mass transfer (Rappaport et al.,

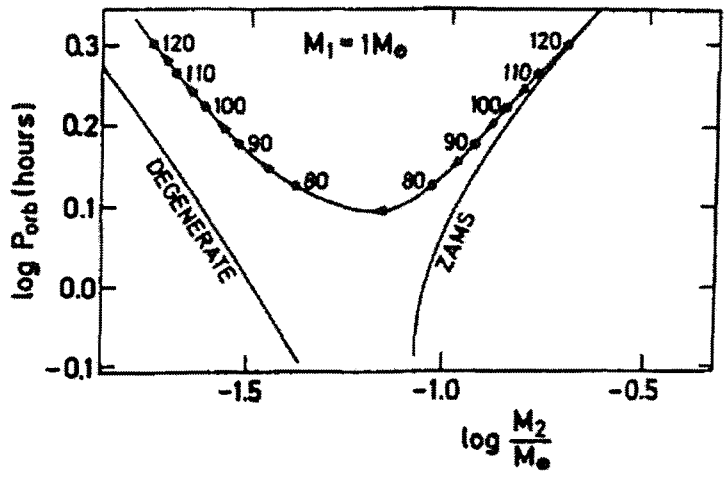

Figure 1.12: Evolution of a CV around the period minimum. From Ritter (1986)

1982). For mass donors with $M_2 \lesssim 0.08 M_\odot$ the star becomes fully degenerate and no longer burns hydrogen. It is effectively a very low mass hydrogen-rich white dwarf, and as such should obey the mass-radius relationship (Chandrasekhar, 1939) which states that

$$R(2) \approx 8.96 \times 10^8 (1+X)^{5/3} M_2^{-1/3} \qquad \text{[cm]} \qquad (1.17)$$

where X is the hydrogen fraction of the gas. Thus, any decrease of mass thus leads to an increase in the radius of the mass donor. Substituting equation (1.1) into equation (1.7) to replace the binary separation, a and then substituting $R(2)$ from equation (1.17) into the result gives

$$P_{\rm orb}({\rm hr}) \approx 1.29 \times 10^{-2} (1+X)^{5/2} M_2^{-1}. \qquad (1.18)$$

From equation (1.18) it can be seen that mass transfer results in an *increase* in orbital period. Obviously, this implies the existence of an orbital period minimum, see Fig. 1.12.

Several explanations have been invoked for the existence of the period gap, but the hypothesis currently favoured is the disrupted magnetic braking model (Spruit and

Ritter, 1983; Verbunt, 1984). Robinson et. al (1981) initiated this train of thought by noting that the period gap corresponded to the range of masses over which the mass donor changes from a star with a deeply convective envelope to a one with a fully convective one. Contraction of the mass donor to its thermal equilibrium radius, due to internal restructuring will then allow a cessation of mass-transfer until sufficient angular momentum has been lost to shrink the orbit and cause contact again at the lower edge of the period gap. Current models of disrupted braking are based on these ideas.

The top panel of Fig. 1.11 illustrates other properties of dwarf novae as we observe them. Practically all of the SU UMa systems are below the period gap. Most of the U Gem types are above the period gap, and all of the Z Cam systems are also above the period gap. The second panel down shows that most of the nova-likes are clustered around the $P_{\rm orb} \sim 3-4$ hours region. The bottom panel exhibits the distribution of the magnetic CVs with orbital period. It shows that most of the polar CVs are gathered around the 1-2 hour orbital period, just below the period gap.

1.7 Accretion theory

In Chapters 5 and 6, the emphasis is on investigating the accretion discs in dwarf novae. Consequentially, in this Section I will introduce 'standard' accretion theory, and describe the various natural disc time-scales that emerge from it, which are fortunately of a convenient duration to be recorded by a human observer.

Accretion is one of the most efficient mechanisms for liberating gravitational potential energy from an astrophysical system. The energy released by a mass, m, falling onto a central mass, M, from infinity to a distance, R, by accretion is equal to GMm/R. It is also one of the most common processes in the Universe, yet it is

still not adequately understood. CVs provide a laboratory for ground-based investigations into this phenomenon. Examples of steady discs, non-equilibrium discs and discs of varying optical thicknesses can all be found in CVs. In addition, the way the accretion discs are affected by changes in white dwarf mass or mass donor size can be observed. The majority of the visible light coming from a CV is from the accretion disc, especially in the outburst phase, when the disc completely overwhelms any contributions from the bright spot, white dwarf or mass donor. Obtaining physical parameters for these discs is important to help cohere the different hypotheses proposed to explain the observed behaviour of these objects.

A consequence of Roche lobe overflow is that the gas being lost from the mass donor has a high specific angular momentum. This prevents it from falling directly onto the white dwarf. At the inner Lagrangian point (L_1), gas is flowing out of the Roche lobe of the mass donor and into the gravitational hold of the white dwarf. The flow here behaves like gas escaping from the nozzle of a pipe into a vacuum, the quantity which controls the velocity of this flow is the thermal velocity of the atoms in the gas. Lubow & Shu (1975) discuss the behaviour of gas particles which flow in the vicinity of the L_1 point. The rate at which mass is lost from the mass donor is controlled by the equation

$$\dot{M}_2 = Q\rho_{L_1}c_s \tag{1.19}$$

where Q is the effective cross-section of the stream, ρ_{L_1} is the density at the inner Lagrangian point, and c_s is the isothermal sound velocity in the gas, which is given by the equation

$$c_s = \left[\frac{kT}{\mu_m m_H}\right]^{1/2}. \tag{1.20}$$

where μ_m is the molecular mass of the atom and m_H is the mass of a hydrogen atom. As the stream leaves the inner Lagrangian point, it is assumed to have a Gaussian density distribution, i.e. a dense core falling off to the outer edge of the flow. As this stream of gas flows away from the mass donor, and into the gravitational pull of the white dwarf, it makes an angle θ_s to the line joining the

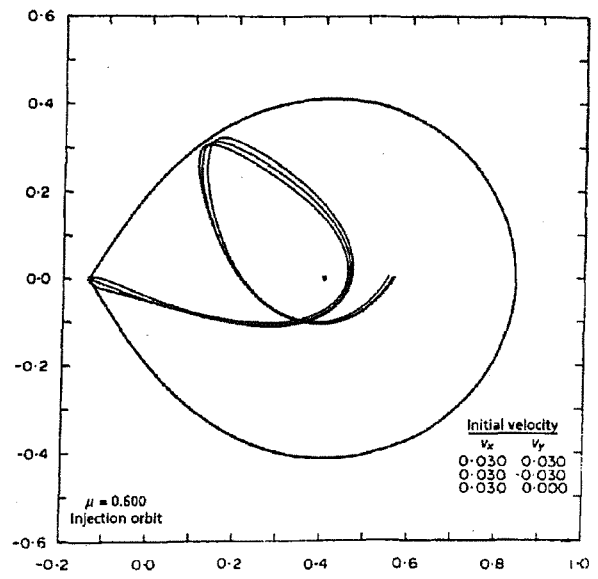

Figure 1.13: The particle trajectories in the orbital plane, originating with low velocities at the L_1 point for a binary with mass ratio $q = 0.67$. From Flannery (1975). Note μ is defined as $M_1 = \mu(M_1 + M_2)$

centres of the two stars, which depends only upon the mass ratio, q, of the binary star (Lubow and Shu, 1975). Once the gas stream is falling towards the white dwarf, the flow velocities become highly supersonic. Integrating the equations of motion for particles rotating in the frame of the binary system allows a determination of the stream trajectory (Flannery, 1975). It is governed by the equation

$$\frac{1}{2}\dot{r}^2 + \Phi_R = constant. \tag{1.21}$$

The ballistic trajectory of the gas stream carries it toward a closest approach point with the white dwarf. This stream has a closest approach distance which can be approximated by the formula

$$\frac{r_{min}}{a} = 0.0488q^{-0.464} \qquad 0.05 < q < 1 \tag{1.22}$$

which is accurate to one per cent (Warner, 1995). After leaving the closest approach point, the stream travels asymmetrically onwards. However because the stream obeys equation (1.21) and it was injected into the white dwarf Roche lobe at low

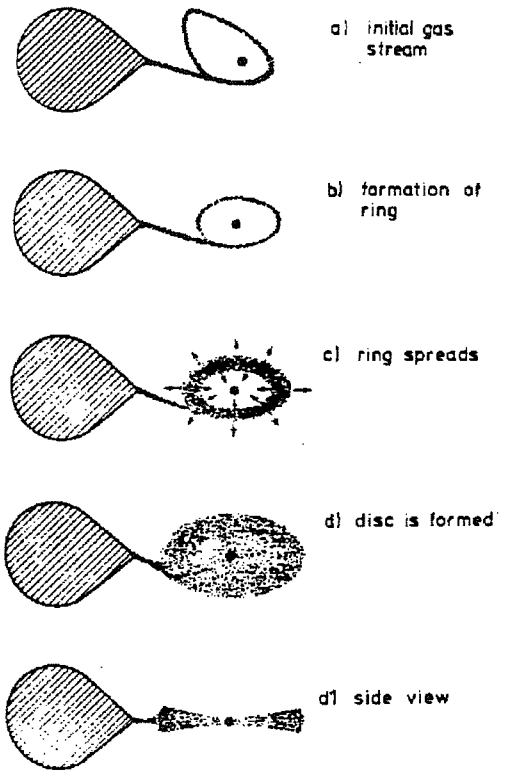

Figure 1.14: Illustration of the initial formation of a ring and it's evolution into a disc (Verbunt, 1982)

velocity, $\dot{r} = 0$, then it does not have sufficient energy to cross the Roche surface at any other point. So the stream trajectory stays within the Roche lobe of the white dwarf and material approaching it does so with $\vec{v} \rightarrow 0$. The stream then returns to impact with itself.Figure 1.13 illustrates particle trajectories from the point of injection into the Roche lobe of the white dwarf at the L_1 point with ballistic trajectories. The solid line depicts the Roche lobe of the white dwarf. At impact with itself, the kinetic energy of the stream is radiated away by shock-heated gas. The angular momentum of the material is conserved, and so the gas tends to redistribute itself into a ring (see Fig. 1.14). The arrangement of particles which has the least energy for a given orbit is a circular one, and so the material re-aligns itself naturally into this configuration. An estimate of the radius of this ring can be made assuming that the angular momentum of the gas as it leaves the L_1 point is

conserved. For a particle in a circular orbit,

$$v_K(r) = \left(\frac{GM_1}{r}\right)^{1/2}. \tag{1.23}$$

Particles which obey equation (1.23) obviously have different velocities at different distances from the white dwarf. A ring like this will therefore rotate differentially, causing a shearing force to develop. This means that viscous processes will heat up the gas and energy is then radiated away, forcing particles to move deeper into the potential well of the white dwarf. This is balanced by some particles moving outwards in order to conserve angular momentum. The outer ring gains angular momentum in this process, which forces the gas at that point to move outwards. The original ring of gas will therefore spread to both smaller and larger radii, into an accretion disc.

Conservation of angular momentum for a particle orbiting at radius r_r requires that

$$r_r v_K(r_r) \approx \frac{2\pi}{P_{\rm orb}} R_{L_1}^2 \tag{1.24}$$

Replacing $v_K(r_r)$ from equation (1.23) into equation (1.24), then using Kepler's third law to replace $2\pi/P_{\rm orb}$ and finally dividing each side by a (the binary separation) gives

$$\frac{r_r}{a} = \left(\frac{R_{L_1}}{a}\right)^4 (1+q). \tag{1.25}$$

R_{L_1}/a can be calculated using equation (1.2). A more accurate value of r_r/a can be determined by calculating single particle trajectories which allow for angular-momentum loss to the mass donor, resulting in

$$\frac{r_r}{a} = 0.0859 q^{-0.426} \qquad\qquad 0.05 \leq q < 1 \tag{1.26}$$

which is accurate to one per cent (Hessman and Hopp, 1990). From equation (1.22) and equation (1.26) it can be seen that $r_r \sim 1.76 r_{min}$. Equation (1.26) gives the **circularisation radius** for a binary system with mass ratio, q. This is the initial

radius at which the ring of gas will form. It gives the minimum size an accretion disc can reach if it is formed due to Roche lobe overflow (an alternative mechanism to initiate disc formation would be via a stellar wind, for example; this leads to a different circularisation radius). If radiation losses are neglected then accretion takes place on the dynamical time scale, τ_{dyn}, see equation (1.31).

1.7.1 Viscosity and its role in accretion discs

Assume cylindrical polar coordinates (R, ϕ, z) and that the disc material lies in the orbital plane ($z = 0$). The matter moves in circular orbits with angular velocity, Ω, around the white dwarf (which has a mass M_1 and radius R_1). Also assume that the material obeys a Keplerian relation regarding its velocity (equation (1.23)). In addition to its circular (orbital) Kepler velocity, v_K, the gas has a small radial drift velocity, v_{rad} which is negative near the white dwarf as gas is being accreted. This velocity is a function of both the its position in the disc, R, and the time, t. The surface density, $\Sigma(R, t)$ characterizes the disc, and is the mass per unit surface area, which is given by integrating the gas density ρ in the vertical direction, z.

$$\Sigma = 2 \int \rho \mathrm{d}z \tag{1.27}$$

These parameters can now be used to write conservation equations for mass and angular-momentum transport in the accretion disc due to the radial drift motions. Consider an annulus of material between radii R and $R + \Delta R$, which has a total mass $2\pi R \Delta R \Sigma$ and total angular momentum $2\pi R \Delta R \Sigma R^2 \Omega$. The rate of change of both of these is given by the net flow from neighbouring annuli. In the limit $\Delta R \rightarrow 0$ the mass reveals

$$R \frac{\partial \Sigma}{\partial t} + \frac{\partial}{\partial R}(R \Sigma v_{rad}) = 0 \tag{1.28}$$

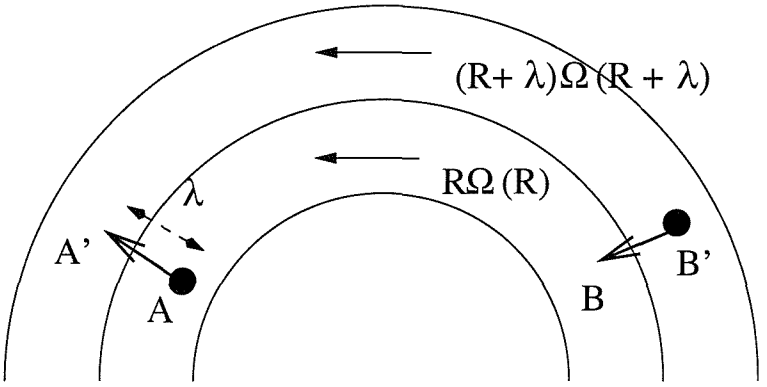

Figure 1.15: Viscous angular momentum transport in a shearing medium

which is the equation for the conservation of mass. For angular momentum considerations the transport due to the net effects of viscous torques $G(R,t)$ have to be included, and carrying this through to the limit where $\Delta R \to 0$ gives

$$R\frac{\partial}{\partial t}(\Sigma R^2\Omega) + \frac{\partial}{\partial R}(R\Sigma v_{rad}R^2\Omega) = \frac{1}{2\pi}\frac{\partial G}{\partial R} \tag{1.29}$$

which is the conservation of angular-momentum equation. Equations (1.28) and (1.29) along with the torque, $G(R,t)$ define the radial disc structure.

Disc structure may vary on different time scales. This viscosity has the effect of spreading in radius the original ring of gas on a typical time scale

$$\tau_{visc} = r/v_{rad}. \tag{1.30}$$

τ_{visc} is called the viscous time scale, and it gives an indication of the time it takes for gas particles to drift a radial distance, r in the disc due to viscous torques. In addition, the disc has a dynamical time scale (τ_{dyn}), which is the shortest of the characteristic disc time-scales and describes the duration over which orbital changes occur,

$$\tau_{dyn} \sim \frac{r}{v_K} \sim \Omega^{-1}. \tag{1.31}$$

Deviations from hydrostatic equilibrium in the z-direction are smoothed out on a

time scale

$$\tau_z = \frac{H}{c_s}. \tag{1.32}$$

This can also be written as $r/\mathcal{M}c_s = r/v_K \sim \tau_{dyn}$, ($\mathcal{M}$ is the Mach number in the disc [equation (1.35)], so τ_{dyn} also reveals the length of time taken to achieve hydrostatic equilibrium in the vertical direction of the disc. Finally, the thermal time scale can be introduced, which describes the time taken to establish thermal equilibrium in the disc,

$$\tau_{therm} \sim \frac{\Sigma c_s^2}{D(R)} \tag{1.33}$$

where $D(R) = 1/2\nu\Sigma(R\Omega')^2$ is the dissipation rate per unit disc area, ν being the disc viscosity. Provided $\Omega(R)$ changes slowly over the length scale of the chaotic motions, $\Omega'(R) = d\Omega/dr$. So τ_{therm} can also be expressed as

$$\tau_{therm} = \frac{R^3 c_s^2}{GM\nu} \sim \frac{c_s^2 R^2}{v_K^2 \nu} \tag{1.34}$$

Defining the Mach number, $\mathcal{M}$ as

$$\mathcal{M} = \frac{v_K}{c_s} \tag{1.35}$$

then the thermal time scale can be expressed in terms of the viscous time scale (equation 1.30) as

$$\tau_{therm} = \frac{1}{\mathcal{M}} \tau_{visc} \tag{1.36}$$

Using the α parameter of Shakura & Sunyaev (1973) (which parametrizes ν as $\nu = \alpha c_s H$), the viscous time scale, τ_{visc}, can be expressed in terms of the dynamical time scale, τ_{dyn}, as

$$\tau_{visc} \sim \frac{R^2}{\nu} \sim \frac{1}{\alpha}\frac{R}{H}\frac{R}{c_s} \sim \frac{\mathcal{M}^2}{\alpha}\tau_{dyn} \tag{1.37}$$

In general,

$$\tau_{visc} > \tau_{therm} \gtrsim \tau_{dyn} \sim \tau_z.$$

The time scale on which gas can redistribute its angular momentum (of the order

days to weeks for typical CV parameters) is longer than both the thermal-adjustment time scale and the dynamical time scale, which are of the order minutes.

1.7.2 Theories of dwarf nova outbursts

In Chapter 5 I will be investigating quiescent accretion disc radii in dwarf novae and soft X-ray transients, in order to differentiate between models created to describe their outbursts. As an introduction to this work I describe the competing theories which were created to explain the outbursts of dwarf novae.

Two main theories emerged to explain the reasons why periods of time exist when dwarf novae increase to a maximum brightness level. Just what initiates this increase in luminosity was a moot point for many years. All of the objects discussed in this thesis were intended to be observed in a quiescent state (at minimum light). This way, the contribution to the light of the system from the accretion disc is at lower levels and so the spectral lines from the mass donor have a better chance of being observed. However, particularly in Z Cam dwarf novae which frequently outburst, it can be difficult to find systems completely in quiescence and there is a high probability that a particular object may be on its way up to or down from an outburst (see Chapter 5 for examples).

1.7.2.1 Mass transfer instability

It was pointed out by Paczynski (1965) that if a star has a convective envelope it will increase it's radius with decreasing mass. So a convective star losing mass onto a companion (as in CVs) could be potentially unstable. Bath (1969) investigated the stability to a loss of mass on dynamical time scales, and found that instabilities gave rise to two characteristic classes. The first class was unstable down to the He I zone, and apparently described the behaviour of U Gem types well, whilst the

other class was unstable down to the He II zone, and the total emission was more equivalent to the output of novae. Osaki (Osaki, 1970) criticised this work, and proposed that the outbursts of U Gem stars were due to an enhancement of energy transport from shear-flow turbulence on the surface of the mass donor as it overfilled its Roche lobe, and obtained cycle lengths of $\sim$ 15 days with amplitudes of 1.5 magnitudes. Following up this research, Bath (1972) studied the time-dependence of the dynamical instability on the mass donor, and concluded that the the properties of the adiabatic instability were consistent with U Gem star observations, but not with novae as he had deduced previously. At this time, it was not known definitively which of the two stars in the binary system was the seat of the outburst. Smak (1971) made the observation that the outburst must originate in either the white dwarf or the accretion disc, or appear in the disc as a result of instabilities on the mass donor. Papaloizou & Bath (1975) discussed dynamical instabilities due to ionization zones on the mass donor, and the mass loss instability found by Paczynski (1965) turned into a much less energetic mass transfer instability (MTI). Bath (1975) found the intervals between outbursts should be of the order 10–200 days, and pointed out that dynamical instabilities in the mass donor should not be considered a sole explanation for the observed DN outbursts and should be used in conjunction with theories involving the response of the accretion disc and gas stream. The instability itself was described as a result of the recombination in H I and He I ionization zones. Mass transfer phases terminate when these zones are carried away by advection and so the mass donor shrinks away from its Roche lobe. Ionization zones are then rebuilt on a thermal time scale. Observationally, there are several reasons why the mass transfer instability is no longer the favoured model. There are no observations of high mass-loss rate systems undergoing outbursts. The model has no $\dot{M}(2)$ above which stable mass transfer would occur. Also, no observations of the bright spot in dwarf novae show an increase in the mass transfer rate either before or during outburst. A major observational piece of evidence supporting the opposing theory appears in the form of polars (magnetic CVs). These systems have no accretion disc, due to the strength of the magnetic field on the white dwarf. Consequently, they

don't have dwarf nova-like outburst states as such, although they do experience high and low states due to fluctuations in the mass transfer rate.

1.7.2.2 Disc instability theory

After the realisation that the site of the luminosity increase was actually the accretion disc, theories were developed in order to explain why the increases occur. The dwarf nova outbursts were now attributed to occasional accretion events from the disc. This allowed an explanation for the standstills of Z Cam stars to be formulated, as examples of stable accretion taking place. A mechanism for this instability was first proposed by Hoshi (1979) who was researching the behaviour of the accretion disc if the mass transfer rate from the secondary was lower than that in the disc (due to variations in the disc viscosity parameter, α). The condition $\kappa_R \sigma \sim 1$ was determined, κ_R being the Rosseland mean opacity, for an optically thick annulus of accretion disc where matter accumulates. Hoshi (1979) noted that the Rosseland mean opacity passes through a maximum at around 10,000K for typical stellar compositions, so κ_R will be double-valued for each value of surface density, Σ. Two different $\dot{M}(d)$ will therefore satisfy the equilibrium condition. This behaviour, now referred to as the 'S-curve' in the $\Sigma - T_{\rm eff}$ plane is shown in Fig. 1.16. The dashed lines illustrate the cooling and heating directions. For an annulus sitting on the lower portion of the 'S-curve' in Fig. 1.16, an increase in Σ will eventually push it to the limit, Σ_{max} at which the annulus heats on a thermal time-scale to a hot, viscous state and a heating wave propagates throughout the disc. This results in the dumping of all the accumulated mass onto the white dwarf (observed as an outburst). The outburst ends when enough mass has been accreted and an annulus in the disc reaches the minimum critical surface-density to initiate a cooling front which returns the disc to a cool, low-viscosity state.

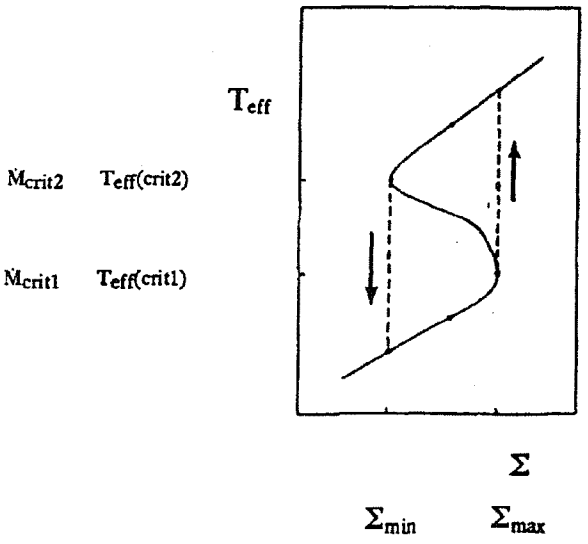

Figure 1.16: The thermal limit cycle for accretion discs. From Warner (1995)

1.7.3 Clues from disc radius variations

Observations of disc radii throughout an outburst cycle can be used to provide support or otherwise for disc instability or mass-transfer instability theory. The MTI model predicts a rapid shrinkage in the disc radius just before an outburst (which is not observed - (Smak, 1989)), due to the addition of low specific angular-momentum material at the outer edge of the disc. This is not present in the disc instability model (DIM). The accretion of mass (and angular momentum) onto the white dwarf requires a balancing movement of mass outwards in the disc, and so the disc radii increase during outburst in both models. Then, in the MTI model, the disc radius shrinks back to a minimum immediately when quiescence begins, whilst the DI predicts a slow decrease in radius over the period of quiescence, until a minimum is reached just before the onset of the next outburst. Eclipse measurements reveal that these variations are observed (Wood et al., 1989, e.g. Z Cha).

1.8 In review

This chapter introduced the group of interacting binary stars called Cataclysmic Variables and went on to describe the interactions which define them, and their evolutionary behaviour and typical characteristics. The appearance and time-variations of their composite spectra were also discussed. Methods which were used during the data analysis to determine various physical parameters (which are demonstrated in the following chapters of this thesis) were also presented. A review of the theory relevant to the analysis contained in subsequent chapters was also provided.

Much of the work in this thesis is based upon spectroscopic observations. In the next chapter, I shall describe the observations which were taken, and will present the data reduction techniques used on the different data sets.

Chapter 2

Data acquisition and reduction techniques

Summary

All the data sets used in this thesis were obtained in the period 1997–1999 using the Isaac Newton Group (ING) telescopes which are operated on La Palma, in the Canary Islands (Latitude: +28° 45′ 30″; Longitude: 01h 11m 31s W, altitude: 2326m). Two of the three ING telescopes were used – the 4.2-m William Herschel Telescope (hereafter WHT) and the 2.5-m Isaac Newton Telescope (hereafter INT). Spectroscopy was carried out on both telescopes. On the WHT, double-beam spectroscopy enabled two wavelength ranges to be covered simultaneously. Echelle (high dispersion) spectroscopy was obtained for one target, EM Cygni, over the wavelength interval 4000–9000Å. The INT was used to obtain long-slit time-resolved spectroscopy of the binaries discussed in this thesis in both the R-band and the I-band. In addition, the auxiliary port at the Cassegrain focus of the WHT was used to obtain high resolution images of the field around EM Cygni. This chapter discusses the instrument configurations used in each of the observing runs,

Table 2.1: Summary of the Observations used in this thesis (listed in chronological order)

Dates	Telescope[a]/ Instrument/Grating combination	Wavelength range (Å)	No. of nights	No. of clear nights	Resolution ($km\,s^{-1}$)[b]
19-23/06/97	I/IDS-500/R1200Y	6220-6641	5	5	37
22-23/10/97	W/ISIS/H2400B	3734-4136	2	1.25	27
	W/ISIS/R1200R	8441-8821			22
10-13/08/98	I/IDS-500/R1200R	8475-8857	4	2	
08/06/99	W/aux port	UBVRI	1.5hr	5.5hr	0.3″
27,28/07/99	W/UES+E79	4145-8774	5.5 hr	2hr	5.7
13,17/08/99	W/UES+E79	4145-8774	-	2hr	5.7

[a]I - INT; W - WHT

[b]Unless marked otherwise

and describes the data reduction methods. Table 2.1 provides an overview of the observing runs from which data are analysed in this thesis. It provides a summary of the observing dates, wavelength ranges covered, and the resolution of the data (in kilometres per second unless otherwise indicated).

2.1 WHT data

Three data sets were obtained using the WHT. The first was taken using the double-armed ISIS long-slit spectrograph. The next set utilised the auxiliary port camera at the Cassegrain focus of the telescope to obtain U,B,V,R and I-band images. The final set of data was echelle spectroscopy: covering 4000–9000Å over 29 orders. All the WHT data required different reduction techniques, which are described in the following sections; the data acquisition and observing requirements are discussed first.

2.1.1 W/97B/28: Supersonic line broadening in accretion discs

Two nights were awarded on the WHT to use ISIS in order to obtain spectra of dwarf novae in quiescence at two simultaneous wavelength ranges. The weather on the first night was reasonable, with the seeing measured at ~ 0.8 arc sec, although cloud affected some exposures in the second half of the night. On the second night, the seeing had increased to 1.2 arc sec, and then observing was badly affected by cloud, with the dome forced to close about one hour into the observing session and not re-opened that night.

ISIS is a double-arm medium-resolution long-slit spectrograph capable of simultaneous observations in two different wavelength regions. This is made possible by the use of a dichroic. Each of the two arms has its optical components optimised for a particular wavelength range. One arm is optimised for $3000-6000$ Å (the blue arm) whilst the other arm is optimised for $5000-10000$ Å, the red arm. Calibration frames need to be taken separately for each arm. The slit is common to the two arms, and has a maximum slit length of $4'$. The slit width can be varied from $0.14''$ to $22.6''$. A possible nine gratings can be used with ISIS. These range from having 150 lines per millimetre (for low dispersion spectra) to having (on the blue arm only) 2400 lines per millimetre. For these observations the R1200R and H2400B gratings were used on the red and blue arms respectively. The R1200R grating had a spectral range of 420Å when used with the TEK CCD-chip, giving a pixel scale of 0.41Å pixel^{-1}. The CCD mounted on the red-arm of ISIS was the TEK2 chip. The quantum efficiency of the CCD was below fifty per cent in the wavelength range used. The H2400B (H stands for 'holographic') produced a pixel size of 0.18Å and a spectral range of 224Å with an EEV CCD-chip. The quantum efficiency of the EEV chip at this wavelength was just under eighty per cent. Thinned chips experience severe fringing when used in the redder part of the spectrum (typical peak-to-peak amplitudes of around 60 per cent in the I-band), hence they are permanently mounted on the ISIS blue arm.

Whilst observing in the red, it was necessary to use an order blocking filter, to cut out unwanted spectral lines due to second order blue light.

Firstly, the central wavelength of each arm was setup to cover the spectral lines of interest (blue: Hδ to H13, covering the Ca II H and K lines; red: Ca II near-IR triplet & Paschen lines). This was done by identifying the arc spectrum resulting from each arm of the spectrograph. The wavelength ranges were then checked with an on-target exposure at the beginning of the evening. The Copper-Neon plus Copper-Argon (CuNe+CuAr) lamps were used to provide wavelength calibration spectra. The CuAr spectrum has few strong lines blueward of $\sim$ 4000Å, so a combination lamp gave the best arc.

Then the rotation of the spectrograph was checked. The long axis of the CCD should be aligned with the dispersion direction of the spectrum; it is possible to do this to an accuracy of 0.3 pixels slope from the bottom of the spectrum to the top. This is usually carried out by aligning the arc lines with the rows of the CCD (this aids later sky subtraction). If the alignment is out by a value greater than 0.3 pixels then some adjustments should be done. For this dataset, the rotation was measured at 0.2 pixels, and so the set-up procedure continued. The tilt of the CCD was checked with a coarse focussing procedure. The cryostat can be moved in two-dimensions so that the CCD is coplanar with the focal surface of ISIS. This was done for both red and blue arms, by opening and closing the left and right Hartmann shutters consecutively. Short exposures of the arc lamps were then taken, and measurements of particular arc line Y-positions were made. One arc line was selected at each of the two extremes of the spectrum, and one chosen near the centre. Measurements of the Y-pixel position were then made at the left-hand edge, middle and right-hand edge of each arc line. The values obtained with the left Hartmann shutter open were subtracted from those made with the right Hartmann shutter open (L - R). The tilt was then calculated by subtracting the mean of (L - R) for the arc line nearest the left-hand end of the spectrum from from the mean of (L - R) for the arc line at the right-hand end of the spectrum. This gave the number of revolutions to adjust the

capstans. The fine focus was then done by adjusting the collimator position.

Exposure times for all comparison frames for each arm of the spectrograph were then calculated. This was done by obtaining exposures of tungsten lamps for each arm of differing durations (with the dekker out), then exposures of the arc lamps, and checking the resulting count levels. For these observations, the red arc exposures were 30s long, and the blue arc exposures 50s. The red flat exposures were 3 seconds long, and the blue ones 500 seconds (due to the nature of the tungsten lamp). A series of bias frames and flat-fields were also obtained. Flat-fields with exponentially increasing exposure-times were taken to calibrate the noise characteristics of the CCD on the blue arm. The resulting readout noise was $R = 7.8e^-$ and the gain $G = 0.77\,e^-\,\mathrm{ADU}^{-1}$. The readout noise measured on the red arm was 3.5 counts. The final step was to start observing. The objects were acquired on the slit, and exposures with durations $\sim 1200 - 1800$ seconds (depending on the magnitude of the CV) were started on each arm of the spectrograph. The slit orientation was set to the parallactic angle. Arcs were taken bracketing each object using both blue and red arms of the spectrograph.

2.1.1.1 W/97B/28: Data reduction

The exposures were examined in order to check for saturated pixels, and to determine the bias region and good region of the frame for each spectrograph arm. Once this had been completed, a balance frame (one which when multiplied into the image frames corrects for the sensitivity variations of the CCD) for each spectrograph arm was created. First, all the useable flat fields were combined into a median frame. Then a mean spectrum in the spectral-direction was obtained (over the good region of the frame). A low-order polynomial (2 or 3 coefficients) was fitted to this spectrum, and the median fiat divided through by the fit. The spatial profile was then divided out of the median flat-field frame. All the suitable sky flats were merged to create a median sky frame, and a twilight spatial profile determined. This

twilight profile was then multiplied into the median flat field, the result inverted and normalised to unity over the good region of the chip. For the blue-arm data, the count range was quite large (due to the red nature of the Tungsten lamp). So, the polynomial was fit to the logarithm of the spectral profile, then the anti-logarithm of the fit used, as this resulted in a fit which was uniform in terms of the deviation from the profile, rather than an absolute number of counts. The resulting balance frame (one for each spectrograph arm), was then used in the data reduction procedure to flat-field the exposures. Sky and object regions were selected from the image frames.

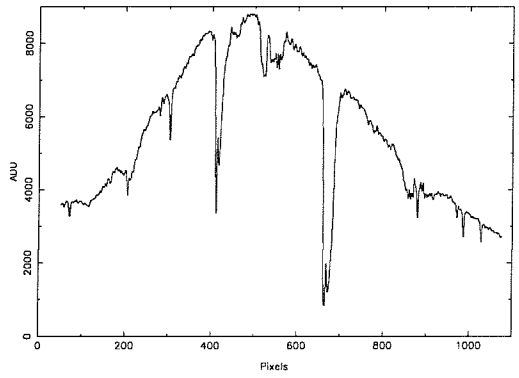

Figure 2.1: Average sky spectrum for the red arm of ISIS

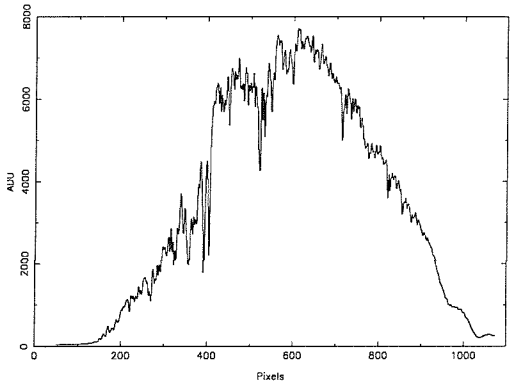

Figure 2.2: Average sky spectrum for the blue arm of ISIS

Then the spectra were optimally extracted (Horne, 1986). The one-dimensional individual spectra were then wavelength calibrated and corrected for slit losses.

2.1.2 W/99A/79: Is the dwarf nova EM Cygni a triple system?

5.5 hrs of bright time were awarded in the 1999A observing semester to gain follow-up observations of EM Cyg to determine if it indeed was a triple system containing a CV. The proposal was divided into two parts, five-colour imaging, and echelle spectroscopy; the latter to be obtained only if a null result was gained with the former.

Table 2.2: Filters used on the auxiliary port

Filter	Type	ING filter number	Central Wavelength (Å)	Width (Å)
U	RGO	202	3560	680
B	Harris	25	4296	1030
V	Harris	30	5461	998
R	Harris	36	6410	1460
I	Harris	41	8120	n/a

2.1.2.1 Auxiliary port imaging: data acquisition

The auxiliary focus (hereafter, aux port) is provided in the Cassegrain Acquisition & Guider (hereafter A&G) unit for on-axis imaging at the Cassegrain focus of the WHT, at the expense of an extra 45° reflection. It was originally provided to obtain short, direct, contemporaneous images for spectroscopic programmes, however the $0.1''\,\mathrm{pixel}^{-1}$ scale on the CCD, and the high throughput in the UV meant it became used as an instrument in its own right. The CCD in use on the aux port at the time of the observations was the TEK1 chip. The quantum efficiencies of the chip are (as percentages) less than forty, sixty, seventy, eighty and less than sixty for the U,B,V,R and I filters respectively. For this programme, the whole chip was imaged. Unfortunately, due to the nature of service observing, the chip was binned by a factor of two in both directions. This allowed shorter chip read-out times, however it resulted in 0.22″ pixels, which were somewhat detrimental to the aims of the proposal. Fig. 2.3 shows the field of view obtained whilst observing EM Cyg. This is a B-band image, in which the accretion disc contributes a greater proportion of light than the mass donor to the appearance of the CV, therefore the CV appears brighter relative to the surrounding stars than in longer wavelength filters.

The aim was to take images through U,B,V,R and I filters in order to detect a change in position with wavelength of EM Cyg. For separation s, a shift of magnitude $\sim 0.3s$ is expected to be seen (see section 3.4.1 for details). At the distance of

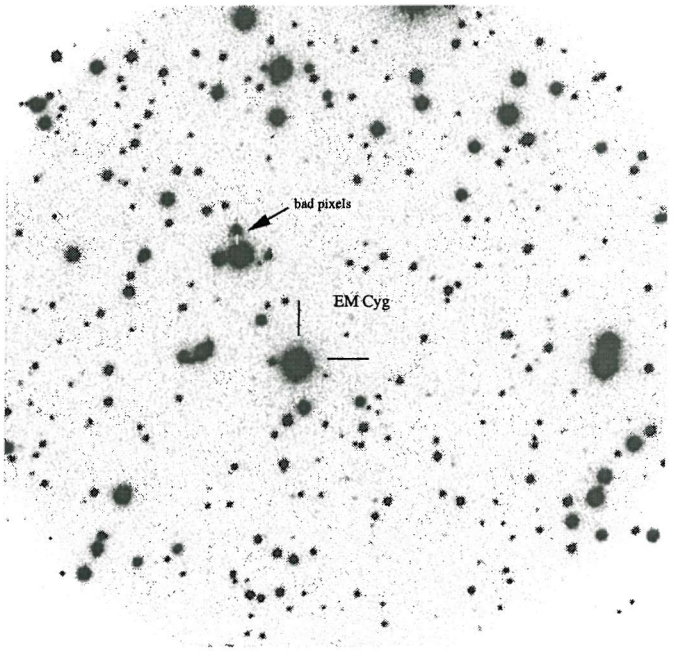

Figure 2.3: The field of view of the auxiliary port imager

EM Cyg ($\sim$ 300 pc) a 3 A.U. separation between the CV and the third star corresponds to $\sim 0.01''$ on the sky. This $0.01''$ converts to an expected shift from U- to I-band of order $0.005''$, which is well below the typical seeing (La Palma typically has $\sim 1''$ seeing). In order to calibrate differential refraction effects (because the field stars all have different colours), observations were requested at three different airmasses, one of which was to be as close to the zenith as possible. Multiple exposures in each filter were also requested to guard against cosmic rays. Lastly, to make full use of the CCD pixel size, the observations were requested to be carried out in as good seeing as possible, and certainly not in conditions with seeing greater than $1.5''$. Estimations of the required exposure times were made. Exposures using the U-band filter were longest at 100s. The B,V,R and I filters only required 20s per exposure. Finally, sky flats (imaging regions of 'blank' sky) were taken in the morning twilight, taken in the order I,R,V,B,U to avoid saturation.

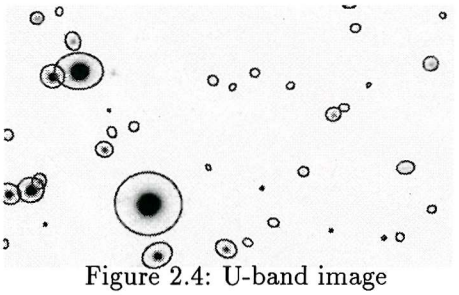
Figure 2.4: U-band image

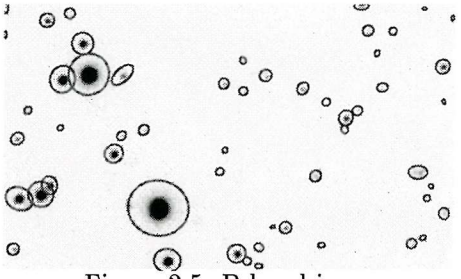
Figure 2.5: B-band image

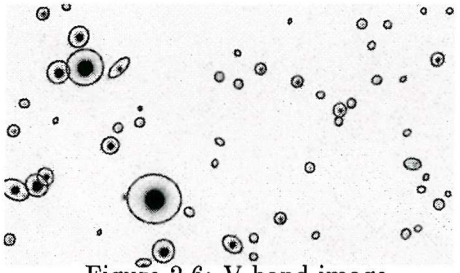
Figure 2.6: V-band image

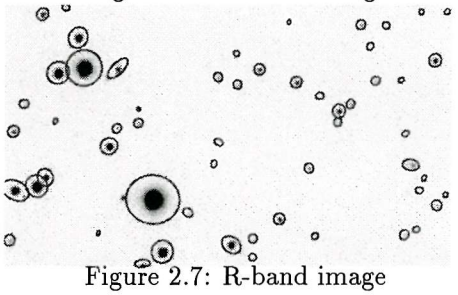
Figure 2.7: R-band image

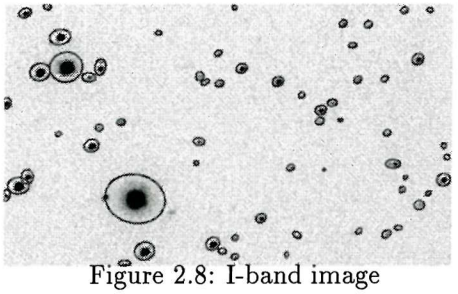
Figure 2.8: I-band image

2.1.2.2 Auxiliary port imaging data reduction

The Image Reduction and Analysis Facility (IRAF) software was then used to remove the bias level and flat-field the image frames. Accurate photometry was not a requirement of the proposal and so no flux standards were observed. The images were examined in order to check for saturation and detect any bad pixels, and to select the comparison stars which were to be used. Then the pixel positions of the objects were measured. Files with the source x- and y-pixel coordinates (measured to within 1/100th of a pixel), source FWHM and information about the source brightness were created for each frame. Figures 2.4 to 2.8 show examples of the results obtained from images in each filter. These images use a negative colour scale. Approximately 50–60 objects were detected with the software per image. The ellipses

show which objects were identified as such and then measurements made. There are a few bad pixels in the top-left corner of the image, which affect the brighter star there in some of the exposures. Consequently, this star was not used in the subsequent analysis. The next step taken was the data analysis (see section 3.4.1.)

2.1.2.3 UES high dispersion spectroscopy

Due to the lack of detection of a conclusive shift, the next stage of the proposal was set in motion. Echelle spectra are generated by using a high angle ($\sim$ 60°) ruled grating cross-dispersed with a low dispersion grating. This produces a high resolution, closely spaced set of orders arranged side-by-side on the CCD-chip which cover a large wavelength range.

This part of the proposal required observing EM Cyg whilst the CV was at a quadrature phase (*i.e.* when the radial velocity of the mass donor was at its maximum positive or negative value). This would ensure that the broad mass-donor absorption lines were minimally affecting the narrow ones from the contaminating third-star. With an orbital period of $\sim$ 7 hr EM Cyg has two quadrature phases per night. Once the service nights had been scheduled, the times of these phases were calculated for each date. Four epochs of spectroscopy were requested, in order to obtain as long a baseline as possible to the observations. This would increase the range of periods which could be detected. Exposures of EM Cyg of duration 1800s were obtained in order to cover completely the quadrature phase. To calibrate the wavelength scale (the spectra covered 4000Å to 9000Å) thorium-argon comparison lamp spectra were taken before and after the target exposures. Bias frames and images of a uniformly illuminated source (flat fields) were also acquired. Seeing and weather information at the time of the observations were not available on the observing log.

2.1.2.4 Data reduction

The data were transformed from 2-D images to 1-D spectra. Each EM Cyg exposure was 1800s long, and so was spattered with cosmic ray hits. Firstly, the images needed rotating through 90° as the order tracing algorithm required the orders to be parallel to rows of the CCD, whereas straight off the telescope they were parallel to the columns (see Fig. 2.9). Then the images were trimmed so that only the good region of each frame remained. Finally, the images had to be flipped over so that the wavelength increased in the direction desired by the software. (Alternatively, the frames could have been rotated in the opposite direction to start with.)

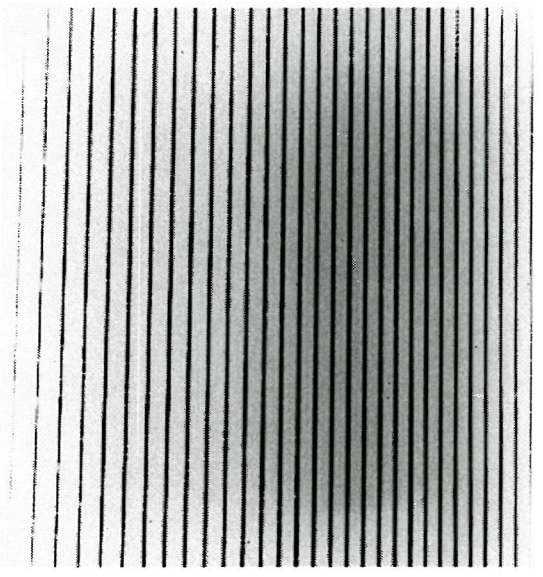

Figure 2.9: An example Echelle data frame

Figure 2.9 shows an example of one of the target Echelle data frames. The illumination of the chip varies from one side to the other, those orders just off-centre on the chip being brightest. In addition the inter-order spacing decreases with longer wavelengths (left-to-right on Fig. 2.9). The image frames then had their bias level removed. One of the bright star frames was examined in order to determine the inter-order spacing, order width, and number of orders. The first step was to locate the orders. This routine gave the option to check the frame; to check that the dimensions of the order-trace frame, object frame and arc frame were

identical. It also checked for any bad pixels, rows or columns, whether they'd been indicated or not, and checked for saturated pixels (the saturation level being set by the user). Saturated and bad pixels, and blemishes on the chip can all disrupt the tracing process so it was important that any features present were noted by the software. Finally the order slope (the deviation from being parallel to rows) and number of orders was determined, and an interactive plot displayed, see Fig. 2.10. In this case, 29 orders with a slope of -0.02 were identified. Orders could be added to

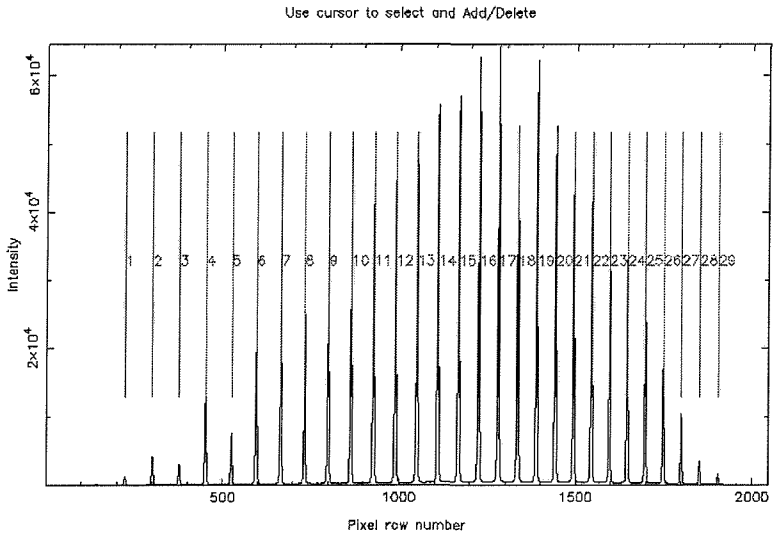

Figure 2.10: The orders located on the trace frame

or deleted from this plot. Once the required number of orders had been identified, the order tracing could begin. Tracing was completed by moving outwards from the centre of each order. This ensured that all possible orders were traced. This was a largely automatic procedure, and the traced paths could then be viewed in a graphics window. The number of coefficients used for tracing the orders could be altered. In this case a third-order polynomial was used. Then the orders were interactively fitted. Obviously spurious points were clipped, and the fit checked. Once the fit was satisfactory the dekker limits of the orders were calculated using a flat-field frame. The dekker limits were located by calculating the profile along the slit and then determining the points where the intensity dropped below a certain threshold. Then the object profile was measured. Both dekker limits and sky and

object limits could be interactively tweaked. In this dataset, the dekker limits were set to -25 and 23 pixels from order centre for lower and upper limits respectively (Fig. 2.11). The object profile ran from -8 to +7 pixels from the centre of the order (Fig. 2.12). The next step in the echelle reduction was to model the flat-field

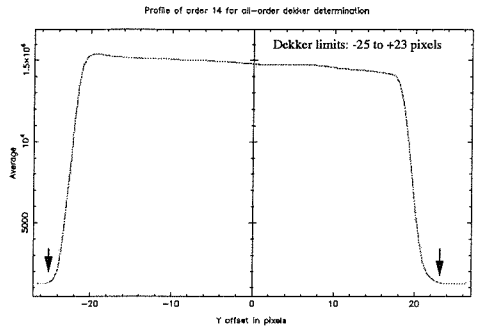

Figure 2.11: Setting the dekker limits

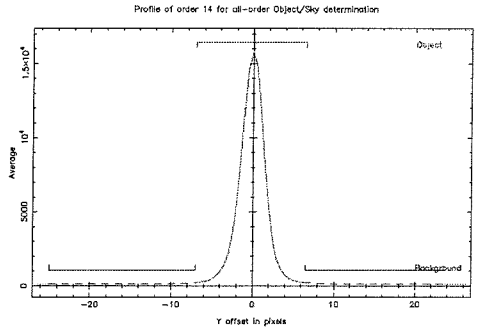

Figure 2.12: The object limit setting task

(variations in pixel response). Balance factors for each pixel in the image, which when multiplied into the object frames corrected for these changes were calculated using a flat-field frame. The tungsten lamp exposure was obtained with the same instrument set-up as for the object frames. The next step was to model either the sky background or the scattered light depending on whether there was severe scattering contamination. In the first case, the sky intensity was modelled along each order with a polynomial whose degree was chosen prior to starting the task. In the case of severe scattering contamination, independent polynomials were fitted to the inter-order pixels (image columns). These were then used as input to a second round of fits which ran parallel to the orders. For this data the sky background was modelled. The next step in the reduction process was to model the object profile, and then extract the object and arc orders over identical pixels. The same weights were used for object and arc extractions. In this case optimal weights (based on the scheme devised by Horne (1986)) were used to extract the orders. The spectra were blaze-corrected (a process used instead of flux-calibration to remove the instrumental response from the data). The blaze-correction procedure involved fitting curves to the flat-field orders. These curves were then 'normalised' to unity, and divided into the extracted spectrum orders. In this case a spline was fitted to the orders.

This was an interactive task, and the fits could be examined and tweaked until the required fit had been achieved. Extracted object and arc orders were written out to NDF files.

At this point it should be noted that, upon examining the spectra, there appeared to be several cosmic ray hits still present. The cosmic-ray checking procedure in the order-locating process repeatedly crashed the software, even when various parameters were tweaked. There was a second cosmic-ray checking procedure which could be carried out immediately after the dekker and object limits had been defined. This procedure failed to converge with the UES data set, and so had to be abandoned. The final opportunity to target cosmic rays was within the order extraction task itself. This performed adequately, but missed one or two glaring candidates in particular orders. The only alternative solution here, was to go back and examine the images for cosmic ray hits with an independent software package before the echelle reduction proceeded.

Once the cosmic-ray free, extracted orders were available in one-dimensional format, a wavelength calibration was applied. A major difficulty with echelle data is the arc-line identification, and finding a preliminary solution to provide the software with. A Thorium-Argon (Th-Ar) lamp was used to obtain calibration frames. Knowing roughly the central wavelength (from the exposure headers), and having worked out which echelle order that should correspond to, meant that the line-identification was at least attemptable. Once the orders had been identified, and a Th-Ar line list obtained, the Th-Ar arc maps were consulted to identify a few major lines to aid the software. This was quite a lengthy procedure, taking longer than anticipated. The problem was exacerbated by the fact that the arc frames had saturated in the longer-wavelength orders, and so very few lines were identifiable there. This meant that the wavelength calibrations for echelle orders 32–26 were

only approximate, and so they weren't used for any subsequent cross-correlation analyses.This was unfortunate, as this was the spectral region where the third star would be appearing most strongly. Following the wavelength identification, files of 1-D spectra were created. The spectra were then ready for analysis (see Chapter 3).

2.2 INT data

Two data sets were obtained using the Intermediate Dispersion Spectrograph (IDS) mounted on the INT. The first, to get spectra in the wavelength range ~6200–6600Å, used the R1200Y grating (which has the largest efficiency at these wavelengths) with the 500-mm camera. The second was again with the 500-mm camera but using the R1200R grating to cover the wavelength range around the Ca II near-IR triplet lines around 8500–8600Å. Both of the observing runs used TEK charge-coupled device (CCD) cameras to image the spectra. These devices have 24-μm pixels, which when combined with the 500-mm camera gives a spatial scale of 0.33″ pixel^{-1}. In the regions of interest, the quantum efficiencies of the TEK chips are 75 per cent for 6200 – 6600 Å and 50 per cent in the range 8500 – 8600 Å.

2.2.1 I/97A/13: The ages of cataclysmic variables

Five grey nights (June 19-23 1997) were awarded to obtain spectra over a full orbital period of long-period dwarf novae ($P_{\rm orb} > 6$ hr). The ultimate aim of the observing proposal was to obtain accurate radial velocities for a sample of CVs, in order to derive their systemic velocities with respect to the Sun.

The Intermediate Dispersion Spectrograph (IDS) is situated at the Cassegrain focus of the 2.5-m INT, and can be used with a choice of camera; the 500-mm camera, or the 235-mm camera (their focal lengths). The 500-mm camera on the

IDS has a scale at the detector of $13.8''\,\mathrm{mm}^{-1}$ in the direction of the slit, compared to the value of $29.4''\,\mathrm{mm}^{-1}$ for the 235-mm camera. Therefore the 500-mm camera gives better-sampled spectra – this was the main reason for choosing the 500-mm camera for this project. Conditions were clear throughout the five nights of observing, and the seeing was approximately 1 arc sec. The R1200Y grating was used, which was blazed to 6000Å and gave a dispersion of $16.4\text{Å}\,\mathrm{mm}^{-1}$ with the 500-mm camera. The central wavelength was set to 6481Å, which resulted in a wavelength range of 6200–6640Å. Unfortunately, this configuration just missed the He I line at 6678Å, however Hα was just off-centre on the chip window and the mass of lines from the companion star blue-ward of 6500Å were all captured; these lines were the reason for choosing this wavelength range to observe in. The mass donor manifests itself here quite strongly in quiescence, and the lines are not too blended if an adequate resolution is used.

Each target exposure was $200 - 300\,\mathrm{s}$ duration, the value used depending on the brightness and the orbital-period length of the CV, in order to keep sufficient phase resolution that no orbital smearing would be introduced. The Hα radial-velocity variations involve components moving with amplitudes are of the order 400–600 $\mathrm{km\,s}^{-1}$. This puts an upper limit on the exposure length of 1/60th to 1/120th of the orbital period to avoid smearing ($\sim 200 - 400$ seconds). The mass donor amplitudes (typically around 150–200 $\mathrm{km\,s}^{-1}$) set their own limits, of approximately 1/30th of an orbital period ($\sim 700 - 800$ seconds). Due to the brightness of the four targets, the Hα requirements were reached quite easily. The DN observed all had orbital periods in the range $0\overset{\mathrm{d}}{.}25 \leq P_{\mathrm{orb}} \leq 0\overset{\mathrm{d}}{.}29$, and were tracked for a minimum of 6 hours at one time. The DN observed are listed with exposure times and orbital periods in Table 2.3.

The 0.8 arc sec wide slit was oriented in order to capture the spectrum of both the DN and a second star on the slit. This allowed an estimate of the slit-losses to be made and a correction applied, and also provided a check for variability in the CV. However, rotating the slit meant that the observations were not carried out at the

Table 2.3: A summary of the observations taken in June 1997 on the 2.5-m INT. All used the IDS 500-camera with the Tek CCD chip and R1200Y grating giving a dispersion of 0.4Å per pixel, and resulting in a resolution of 0.8Å (FWHM).

Object	Date observed (UT, June 1997)	Exposure time (s)	Orbital Period (days)	Reference
EM Cyg	21.932-22.220	200	0.2909	1
V426 Oph	20.924-21.207	200	0.2853	2
SS Cyg	23.005-23.231	200	0.2751	3
AH Her	19.912-20.169	300	0.2581	4

References: (1) Stover et al., 1981 ; (2) Hessman, 1988;
(3) Hessman et al., 1984; (4) Horne, Wade & Szkody, 1986.

parallactic angle. An R-filter was used on the TV to ensure that both stars could be kept on the slit. Spectra of radial-velocity standard stars were also obtained to calibrate the velocities measured from the DN. They were also used to obtain a spectral type for the mass donor in each DN, and so only those standards with good spectral types were chosen. These were selected from the lists of Marcy, Lindsay & Wilson (1987), Barnes, Moffett & Slovak (1986), Beavers & Eitter (1986), Beavers et al. (1979), Duquennoy, Mayor & Halbwachs (1991) and Eggen (1992).

2.2.1.1 Data reduction

The resulting spectral dispersion with the IDS-500 camera and the R1200Y grating was 0.4 Å per pixel and the spectra covered 6230 to 6650 Å. All the spectra had a FWHM resolution of 0.8 Å. Arc calibration spectra were taken every 35 minutes or so in order to eliminate errors in the wavelength scale caused by flexure of the spectrograph, and were also taken before and after every change of object. The arc spectra were extracted over the same region as the objects, and then line identification carried out. The resulting arcs were fitted with fourth-order polynomials. The rms scatter of these fits was of the order 0.005 Å. The arc spectra were linearly interpolated in time to provide the wavelength calibration for each dwarf nova spectrum.

The CCD frames had the bias level removed and were then corrected for any pixel-to-pixel sensitivity variations using exposures of a tungsten lamp. Variations in the illumination of the slit were corrected using exposures of the twilight sky. The spectra were extracted with optimised weights (Horne, 1986) and then corrected onto a flux scale using a flux standard from Oke & Gunn (1983). The correction for slit losses involved determining the comparison spectrum which contained the most counts, then dividing all the other comparison spectra by it. This gave a sequence of 'normalised' comparison star spectra, which were then fitted with quadratic polynomials and the fits divided into the object spectra, to adjust their count levels accordingly. Average spectra for each object were then created by co-adding the individual object spectra. The spectra were normalised by their continua, which were then subtracted, before averaging. Their analysis is discussed in Chapters 3, 4 & 6.

2.2.2 I/98B/12: Ca II spikes and the mass donors of CVs

Four nights were awarded in August 1998 to use the INT/IDS 500-mm camera combination to observe the Ca II near-IR triplet in a range of CVs, in order to confirm the presence of 'spikes' due to the mass donor in a selection of CVs, which had been detected in a previous WHT run (section 2.1.1). Full-orbit coverage, in order to locate the origin of the emission, was required. If successful this project would open the door to a new, sensitive method of detecting the mass donors in Cataclysmic Variables.

The R1200R grating was selected, which was blazed to 8000Å and when combined with the 500-mm camera had a dispersion of 15.5Å mm^{-1}. Again, the TEK3 chip was used, giving a scale of $\sim$ 0.37Å $pixel^{-1}$ in the dispersion direction. Conditions were cloudy interspersed with periods of clear weather over all four nights. Night 1 was possibly affected by dust, as the conditions were very hazy, although the seeing was reported to be $\sim$ 1 arc sec. The second night was badly affected by cloud; only three hours were usable, and passing cloud affected the exposures. The third

night was again affected by cloud. At one point for a couple of hours, cloud was everywhere bar the zenith, and only objects in Cygnus could be observed! The final observing night was only mildly troubled by cloud, however the seeing remained poor.

An order blocker was put into the light path to remove second-order blue lines. The slit width was set to 0.9″ which gave the arc lines a FWHM of 2.5 pixels. The central wavelength was set to 8696Å; this ensured that a good wavelength calibration could be obtained by including a strong arc line at one extreme of the pixel range. Unfortunately, this meant that one end of the Ca II 8498Å line did not have much accompanying continuum, and in some cases was cut short itself. A Copper-Neon plus Copper-Argon (CuNe+CuAr) lamp was used to create wavelength calibration spectra. Arcs were obtained both before and after a change of object, and every half hour or so in between. Flat-field frames (tungsten lamp exposures) were also taken before and after each change of object, to allow accurate removal of the instrument response. Finally, observations of several radial velocity standards, taken from the lists of Marcy et al. (1987) and Beavers & Eitter (1986) were obtained in order to calibrate the radial velocity variations from the emission components. In addition, spectra of a rapidly rotating B-star were taken to calibrate out any telluric lines which might be present. Table 2.4 gives a list of the objects which were observed, and what fraction of an orbit was covered given the weather conditions.

2.2.2.1 Data reduction

The spectra had the bias level removed (measured at $\sim$ 560 counts) and were corrected for pixel-to-pixel variations in sensitivity, using a technique similar to that mentioned in section 2.1.1.1 to create a 'balance' frame for each object, interpolating between the two nearest flat-field images. The twilight sky profile was multiplied into each balance frame to be used in the flat-fielding procedure, to correct for variations in the illumination along the slit. The sky regions (pre-selected for each object)

Table 2.4: A summary of the observations taken in August 1998 on the 2.5-m INT. All used the IDS 500-camera with the Tek CCD chip and R1200R grating

Object	Date observed (UT, August 1998)	Exposure time (s)	Fraction of $P_{\rm orb}$	$P_{\rm orb}$ (days)	Reference
V795 Her	10.903-10.960	200	0.5	0.1082468	1
AB Dra	10.971-11.132	250	1	0.1520	2
UU Aqr	11.142-11.181	300	0.24	0.163580	3
RX And	11.191-11.249	300	0.28	0.209893	4
	13.170-13.247	300	0.37	...	...
WZ Sge	12.061-12.156	150	1.7	0.056688	5
MV Lyr	12.875-12.985	200	0.83	0.1329	6
SS Cyg	13.019-13.163	300	0.53	0.27512973	7
V1315 Aql	13.895-14.032	240	1	0.139690	8
EM Cyg[a]	14.039-14.074	270	0.1	0.290909	9
V425 Cas	14.089-14.219	250	0.87	0.1496	10

[a] in outburst so observations ceased

References: [1] Casares et al. (1996); [2] Hessman (1988); [3] Goldader & Garnavich (1989); [4] Kaitchuck (1989); [5] Skidmore, Welsh, Wood & Stiening (1997); [6] Skillman, Patterson & Thorstensen (1995); [7] Hessman et al., (1984); [8] Hellier (1996); [9] Beuermann & Pakull (1984); [10] Shafter (1983)

were fit with quadratic polynomials to estimate the amount of sky underneath the target. Both the object and arc spectra were then extracted over identical pixels using optimised weights (Horne, 1986). The arc lines were then identified and a wavelength calibration applied to all the object spectra, the best result being a fit using a fifth-order polynomial which gave an rms of 0.01Å. Files of one-dimensional spectra were created, then the objects normalised by their continua. After this the continua were subtracted, and the spectra placed onto a uniform velocity scale, ready for analysis (which is discussed in section 5.4.1).

Chapter 3

The dwarf nova EM Cygni and its consequences for the evolution of CVs

Summary

EM Cygni is one of the earliest spectroscopically studied CVs, because of its relative brightness – it has a quiescent magnitude of 13.5 (Ritter and Kolb, 1998). Stover et al. (1981) observed the system in quiescence, and carried out a radial velocity study. The results were strange because they indicated that the star losing material was more massive than the accreting white dwarf, a situation which should be dynamically unstable. Dynamical instability means that EM Cygni should not exist, and it has remained until this point a mystery as to why it appears to be transferring matter and behaving as a normal CV. During an observing run carried out in June 1997 on the Isaac Newton Telescope (INT) on La Palma (section 2.2.1) it was discovered that the spectrum of EM Cyg blueward of Hα is contaminated by narrow absorption lines. These narrow lines are unusual because we expect the lines

from the secondary in EM Cyg to be broadened by rotational effects, to a value somewhere in the region of $100\,\mathrm{km\,s^{-1}}$. Cross-correlation of the EM Cyg spectra with spectra of radial-velocity standard stars of similar spectral-type to that expected for the mass donor ($\approx$K3) reveal a non-varying component interfering with the sinusoidal variation due to the secondary in EM Cyg. The effect of this extra set of spectral lines is to pull in the cross-correlation peaks towards the zero value, so any measurements of the radial-velocity amplitude from the absorption lines of the mass donor are underestimates. Upon removal of this contaminating (hereafter, "third") spectrum, the amplitude of the radial velocity curve increases from $135\pm3\,\mathrm{km\,s^{-1}}$ calculated by Stover et al. (1981) to $202\pm3\,\mathrm{km\,s^{-1}}$. This result removes the dynamical instability, and enables the calculation of a whole new set of system parameters. In follow-up to this discovery, high-resolution UBVRI images of EM Cyg were taken with the WHT, in order to detect a wavelength-dependent shift due to the differing contribution from the third star in each bandpass. The results of that study are presented, as are the initial results from high-resolution Echelle spectroscopy to detect the orbital motion of the third star.

3.1 Introduction

EM Cyg is one of the most familiar examples of dwarf novae (DN). EM Cyg belongs to the sub-class of dwarf novae named after the prototype Z Cam in which the peculiar characteristics of the light curve were first observed. Z Cam stars experience - in addition to the normal outburst/quiescent states of DN - periods of time when they appear to be 'stuck' in a semi-high state, making them appear visually approximately 0.7 mag brighter than at minimum. EM Cyg appeared to be approaching its low state after a standstill when the spectra were taken (Mattei, 1999). Fig. 3.1 shows its light curve behaviour during the period April 1997 to February 1998. An arrow indicates the observation date, in June 1997.

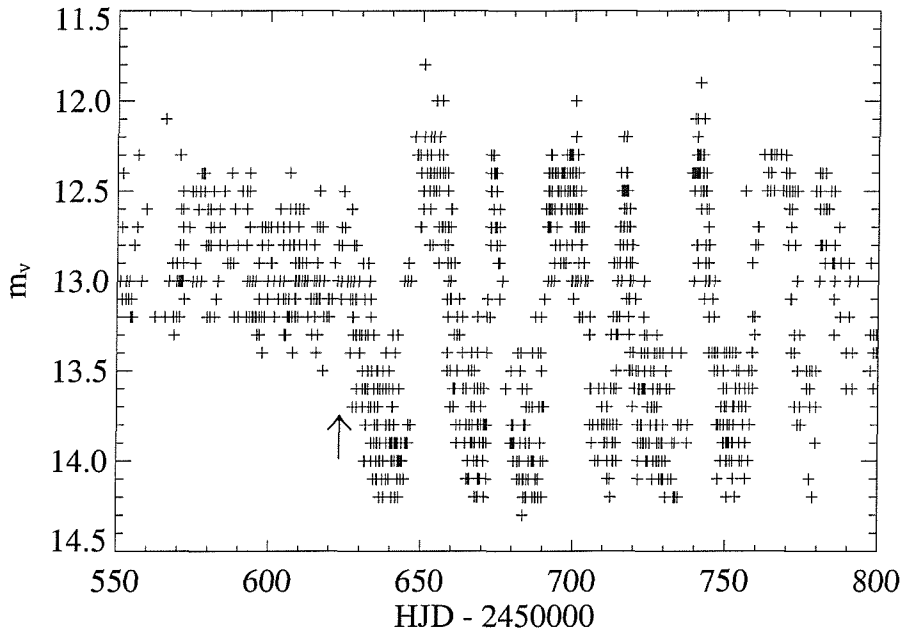

Figure 3.1: The light curve of EM Cyg during 1997. The arrow marks the date of the observations. Data from AAVSO Observations (Mattei, 1999)

Hoffmeister (1928) first detected the variability of EM Cygni (hereafter EM Cyg). It brightened by approximately two magnitudes on a time scale of around twenty-five days. He suggested that this variation was typical of an Algol system, but this was subsequently shown not to be the case. Burbidge & Burbidge (1953) obtained spectra of EM Cyg and due to the presence of broad Balmer emission, and He II 4684Å suggested that EM Cyg was an old nova. The first photometric observations of EM Cyg were published in 1969 (Mumford and Krzeminski, 1969). The data, gathered between 1962 and 1968, were taken in order to determine from the behaviour of the light curve, the classification of the binary. They calculated an orbital period of $P_{\rm orb} = 0.29090942$ days from the times of 29 minima and concluded that an eclipse of the blue component in the binary by the red one could be the explanation for what was being observed. They did note that each minimum differed, sometimes quite markedly, and that wide, shallow eclipses were mainly observed when the system was bright. Robinson (1974) determined spectroscopic orbital elements for the system using previously obtained spectra, and calculated masses for the stellar components using the previously deduced period. This produced

a white dwarf mass of $0.70M_{\odot}$ and a red star mass larger than this at $0.90M_{\odot}$. Mumford (1974; 1975) continued to provide times of subsequent minima, whilst Pringle (1975) published his analysis of period changes in eruptive binaries, which included EM Cyg. He fitted the data with a parabola, the quadratic term being significant at the 99.85 per cent level (3σ on a normal distribution being 99.75 per cent). The time scale for the period decrease was calculated to be $\tau_{\rm P} = 3.8 \times 10^6$ years. Brady & Herczeg (1977) analysed photoelectric observations of EM Cyg, but didn't find any evidence for a Z Cam type variation in the well-covered observing period (1951–1954). Mumford (1980) confirmed that the orbital period of EM Cyg was decreasing from more recent minima timings. The calculated time scale for the period change was now $\tau_{\rm P} = 5.5 \times 10^6$ years. Caution was urged in the paper, suggesting that the main result is purely that the preferred solution to the light elements is non-linear. However, the idea was put forward that a sinusoidal variation with a period of 30 years would fit the data, and that this would occur naturally if there was a third body was present in the system. Following this, Stover, Robinson & Nather (1981) published a radial velocity study using Balmer emission-lines from the disc and absorption lines from the mass donor around 4500Å in order to determine component masses. They reached similar conclusions to Robinson (1974), that the mass donor in EM Cyg was more massive than the white dwarf. Jameson, King & Sherrington (1981) obtained simultaneous optical and IR light-curves, and estimated that the system was at a distance of 320 pc. Steining, Dragovan & Hildebrand (1992) used high-speed photometric observations of EM Cyg to detect coherent luminosity variations (also known as dwarf nova oscillations) during outburst. They could not conclusively decipher the origin of these fast oscillations (e.g. white dwarf or accretion disc normal modes). Finally, in the most recent easily available work on EM Cyg, Beuermann & Pakull (1984) add more minima timings to those given earlier and conclude that the lower limit to the time scale of any period change is $\tau_{\rm P} > 7.5 \times 10^6$ years.

EM Cyg is one of only a handful of Cataclysmic Variable stars which show an

eclipse of the disc every orbit and which have spectral lines from both stellar components of the binary. This makes EM Cyg special amongst CVs, as it means that accurate binary parameters can be determined from spectroscopic and photometric observations. In their classic study Stover et al. (1981) measured the absorption line radial velocity amplitude together with that from the emission lines and obtained a mass ratio for EM Cyg of $q = M_2/M_1 = 1.26$; this value confirmed the earlier study of Robinson (1974), who calculated that $q = 1.29$. A mass ratio greater than one is remarkable because if mass transfer is from the more massive star to its companion, the orbital separation must shrink in order to conserve angular momentum. Unless the donor star shrinks faster than the Roche lobe, mass transfer is unstable. The instability occurs on a dynamical time scale if the adiabatic response of the star fails to keep it within its Roche lobe. At higher donor masses ($M_2 > 0.8M_\odot$) however, the star shrinks drastically when it loses material at a high rate and so the mass transfer becomes stable on a dynamical time scale but it is still unstable thermally (e.g. de Kool (1992), Politano (1996)). The mass ratio ($q = 1.26$) and the donor mass ($M_2 = 0.76M_\odot$) of Stover et al. (1981) lead to dynamical instability according to the criteria given by Politano (1996): EM Cyg should not exist.

Despite this unique status, there have been no more recent studies of EM Cyg. In part, this is probably because measurements of the radial velocities of the white dwarfs in Cataclysmic Variables are normally based upon the emission lines which usually come from the accretion disc surrounding the white dwarf, and these are well known to be unreliable (Stover, 1981a). It would perhaps not be surprising if this problem affected Stover et al.'s (1981) study of EM Cyg. However, EM Cyg is one of the longer period dwarf novae ($P = 6.98$ h), for which the distortions of the emission lines are less significant because of the relatively high amplitude of the white dwarf, and in Stover et al.'s study, the emission and absorption line amplitudes are 20° from being in anti-phase, by no means a large distortion for these stars.

In this chapter new spectra of EM Cyg are presented which show clear evidence for contamination from a third star, which happens to have a very similar spectral

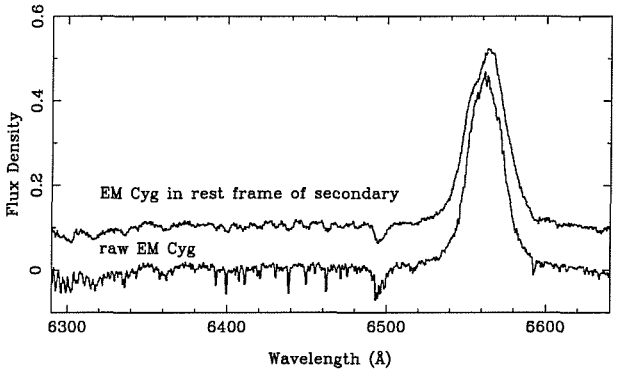

Figure 3.2: The mean spectrum of EM Cyg observed on 22 Jun 1997.

type to the mass donor star. Accounting for the presence of this star increases the radial-velocity amplitude of the mass donor considerably, and causes the mass ratio ($q = M_2/M_1$) to fall below unity, at the same time leading to a larger donor mass. Thus the mass transfer in EM Cyg is stable as expected from theory.

3.2 Results

The observations of EM Cyg taken with the IDS on the Isaac Newton Telescope are described in chapter 2, together with the data reduction methods. Here, the spectra and their subsequent analysis will be discussed.

The mean spectrum of EM Cyg is presented in Fig. 3.2 (lower spectrum). The upper spectrum in Fig. 3.2 shows the average of the 102 spectra after subtraction of the contribution to the absorption lines from the third star, see section 3.2.1, and after shifting each spectrum into the rest frame of the mass donor in EM Cyg, in order to remove the effect of orbital smearing. Absorption features characteristic of a K-type star are visible in the lower spectrum. They are sharp, which is unexpected because the lines from the mass donor are expected to be broadened by rotation, and by orbital motion. These lines are from the third star. It can be seen from this plot that the absorption lines in the upper spectrum (which represent those from the mass donor of EM Cyg) are indeed much wider than those in the lower spectrum,

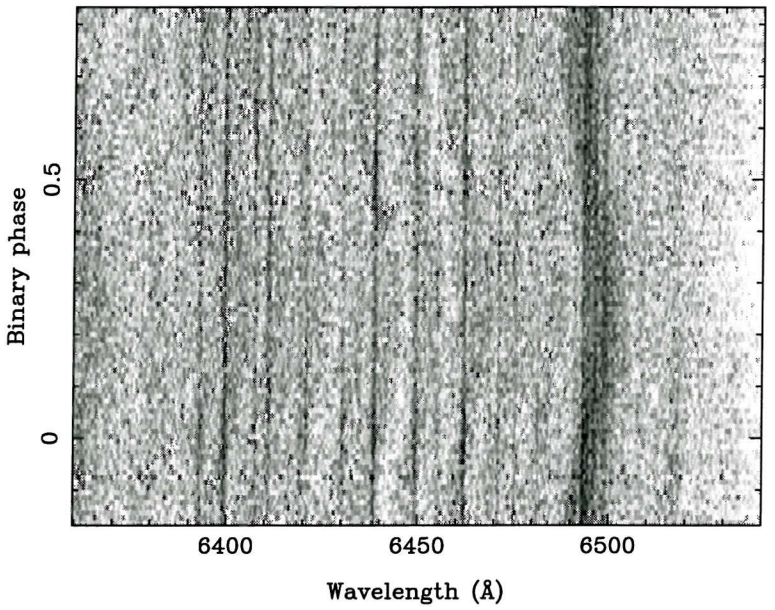

Figure 3.3: The trailed spectrum of EM Cyg scaled to show the absorption features. The contaminating K-star is visible in narrow lines that run straight up the plot. The donor star is scarcely visible, but sinusoidal behaviour can be spotted in the feature at 6495 Å. Hα is not included on this plot (see Chapter 6).

which is as expected due to broadening effects. This is confirmed from the trailed spectrum presented in Fig. 3.3.

The most noticeable feature in Fig. 3.3 is the feature at $\sim$ 6500Å. It looks like a combination of a sinusoidally varying component and a non-varying component. More non-varying absorption lines are evident blueward of this feature, however they dominate any sinusoidal variation which may accompany them, and so appear to be the only features at the wavelengths at which they appear. Figure 3.3 stops short of Hα, which is discussed in Chapter 6.

The procedure followed to get from the lower spectrum to the upper spectrum in Fig. 3.2 is fairly complex, and so a summary of the procedure followed is given first:

i. The continua of all the spectra were fitted and then subtracted, and then re-binned onto a uniform velocity scale.

ii. The average EM Cyg spectrum was cross-correlated (using the method of

Tonry & Davis (1979)) with each different radial-velocity standard star. This was done in order to obtain a list of the relative shifts between the two sets of absorption lines. These shifts were then applied to the standards, so that the absorption lines in the standard were congruous with those of the EM Cyg spectrum.

iii. The standard star spectra were then scaled and subtracted from the EM Cyg spectra in order to remove the absorption lines of the third star. This process is hereafter referred to as "optimal subtraction".

iv. The spectral type of the standard star which gave the lowest χ^2 on subtraction was adopted as the spectral type of the third star (e.g. see Fig. 3.5).

The resulting EM Cyg spectra were then used as described in section 4.3 to determine the radial velocity amplitude of the mass donor, and its systemic velocity. The best-fit circular orbit velocities were then shifted out of the individual EM Cyg spectra, and the results averaged to obtain a spectrum of EM Cyg in the rest frame of the mass donor (Fig. 3.2, upper spectrum).

3.2.1 Removal of the contaminating star spectrum

The presence of the donor star is hard to see in the raw data (Fig. 3.3) and is only obvious at the $\sim$ 6500Å feature, but its motion can be clearly seen after cross-correlation with a K-star radial-velocity standard (Fig. 3.4). The cross-correlation curve due to the mass donor is seen sinusoidally varying up the trailed spectrum. In addition to this there is what appears to be a constant correlation peak close to zero velocity. This is the radial velocity of the sharp absorption lines seen in Fig. 3.2. The right-hand panel of Fig. 3.4 shows the results of the cross-correlation after the removal of the sharp absorption lines from the spectrum. The cross-correlation technique used is similar to that used for SS Cygni (Stover et al., 1980).

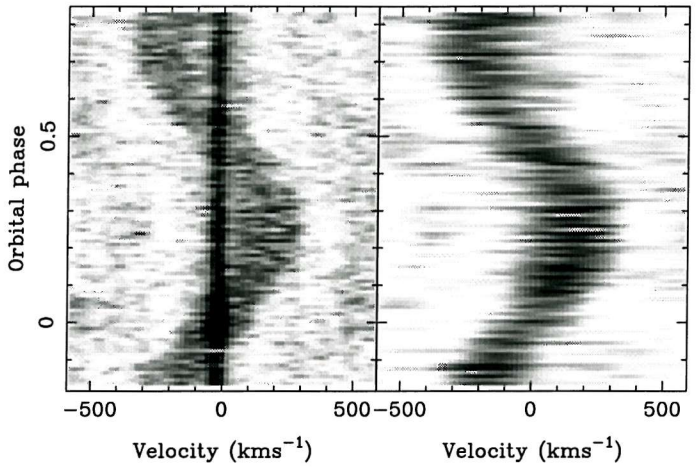

Figure 3.4: Trailed spectra of the cross-correlations with a K-type standard a) before subtraction of a K3V standard, left, and b) after the subtraction, right. As can be seen from a), the contaminating spectrum produces another set of correlation peaks, visible here as a straight line going up the trailed spectrum centred at -20 km s^{-1}. The correlation peaks measuring the radial velocities of the mass donor around the orbit are also visible in both plots. No artificial broadening has been applied to the standard in plot a), but in plot b) the standard has been artificially broadened to $v \sin i = 140\,\mathrm{km\,s^{-1}}$

First, the spectra had their continua fitted and then subtracted and were then transformed onto a logarithmic scale so that the cross-correlation technique could be used to measure the velocity shifts due to Doppler effects. In order to effectively remove the contribution to the absorption lines from the third star, the relative shifts between the velocity-standard stars and the average EM Cyg spectrum were determined, and then applied to the velocity standards. Then the standards were subtracted from the EM Cyg spectra to find the optimum fraction at which the standard should be scaled; see section 3.2.3 for a more detailed description of the procedures followed. This routine provided a formal error on the fractional contribution from the third star, and the standard star which produces the minimum value of χ^2 indicates its optimum spectral type. The standards are then multiplied by this constant, and subtracted from the EM Cyg spectra. The optimum fraction obtained for the contribution of the third star at this wavelength range is 0.160±0.002, with a K3V standard star. The spectral type of the third star could be initially deduced from the appearance of the absorption line spectrum between 6350 Å and 6540 Å (see Fig. 3.5). The criteria developed by Casares, Charles, Naylor & Pavlenko (1993) to determine the spectral type of the mass donor in

V404 Cyg at wavelengths around Hα were used to classify the contaminant. In particular, the lines at Ca I $\lambda\lambda$6439.1, and Fe I $\lambda\lambda$6400.0 + 6400.3, and the blends at Ca I $\lambda\lambda$6449.8 + 6450.2 and Ca I λ6462.6+ Fe I λ6462.7, whose relative depths are useful indicators of spectral type (Casares et al., 1993) were used. However, as can be seen from Fig. 3.5 the relative depth of the blends at wavelengths 6400 Å and 6440 Å are also sensitive to variations in $T_{\rm eff}$. The blend at 6400 Å dominates at spectral types around G8V but then diminishes relative to the blend at 6440 Å becoming equal at spectral types around K3, until it is hardly apparent at spectral types around M4V. In EM Cyg these blends appear to have equal strengths relative to each other, indicating a K3V spectral type. The optimal subtraction process described earlier in this section was carried out for each individual EM Cyg spectrum, and a different constant computed for each. Then the standard was copied and scaled using these constants, and each copy subtracted from the corresponding EM Cyg spectrum. The spectral type of the third star was best fitted by standards between types K2V and K5V. The standard which minimised the value of χ^2 had a spectral type of K3V.

The third star subtraction process was then carried out 'in reverse' to check for possible systematic errors caused by this spectral typing procedure. This means that the absorption lines from the mass donor in EM Cyg (which are broadened by rotational and orbital effects) were optimally subtracted first (using the same general method as in section 3.2.2), and then the best spectral-type for the third star was determined. In this case the optimum spectral type for the third star came out slightly earlier at K2V, indicating that we cannot constrain the spectral type any more precisely than between K2V and K5V with this method.

Finally the sequence of cross-correlation, shifting, and optimal subtraction was repeated using the best-fit spectral-type standard to the contaminating absorption lines (K3V). The resulting spectra were then used (see section 3.2.2) to find out the spectral type of the mass donor in EM Cyg. The relative shift between the standard star absorption lines and those of EM Cyg's average spectrum gave a

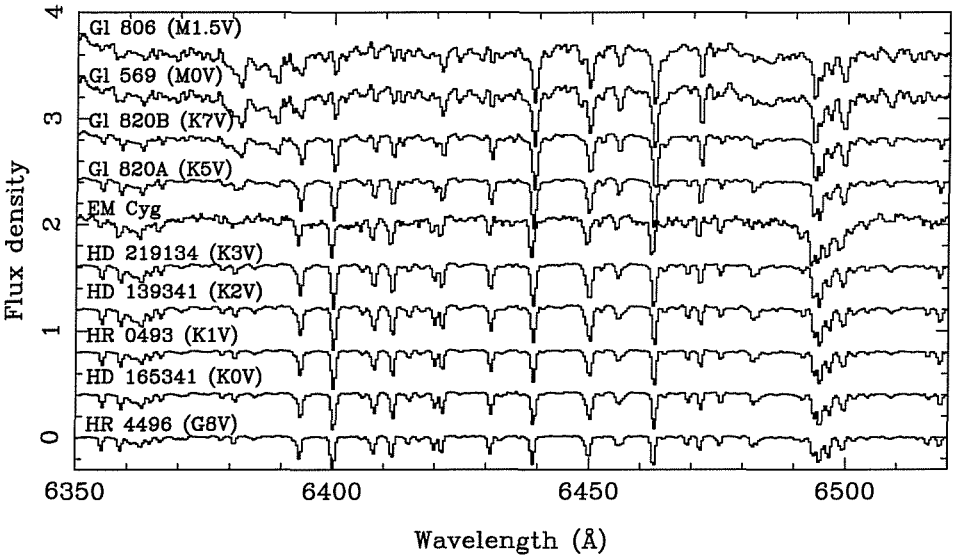

Figure 3.5: The average spectrum of EM Cyg scaled to show the absorption lines in the wavelength region of 6350 – 6540 Å , placed in an apparently suitable position for the third star between spectral types K3V and K5V. The broadened absorption lines from the mass donor underlie those from the third star. The sensitivity of the relative depth of the blends at 6400 Å & 6440 Å with effective temperature is very apparent.

measure of the systemic velocity of the third star. This turned out to be $\gamma = -20 \pm 3\,\mathrm{km\,s^{-1}}$. This is similar to the systemic velocity derived for the mass donor in EM Cyg by Stover et al. (1981) from the absorption lines of the spectrum in the Hβ region ($-23 \pm 6\,\mathrm{km\,s^{-1}}$), and is also similar to the value determined in section 3.2.2 ($-25 \pm 2\,\mathrm{km\,s^{-1}}$). The agreement in systemic velocities of the mass donor and the third star is a hint that they are physically associated (see section 3.3). Figure 3.6 shows the trailed spectra before subtraction of the contaminating spectrum , and after removal. After removal, the third star lines (as discussed in Fig. 3.3) completely disappear, and the sinusoidal nature of the absorption from the mass donor in EM Cyg become apparent. The features around 6300Å are interstellar in origin, and therefore do not experience orbital motion like the lines from the CV.

The absorption lines between 6400Å and 6500Å were used in the cross-correlation procedure. Each EM Cyg spectrum was cross-correlated with the best-fitting template, and a series of cross-correlation functions derived. These cross-correlation functions were then back-projected (in the same manner as for time-resolved spec-

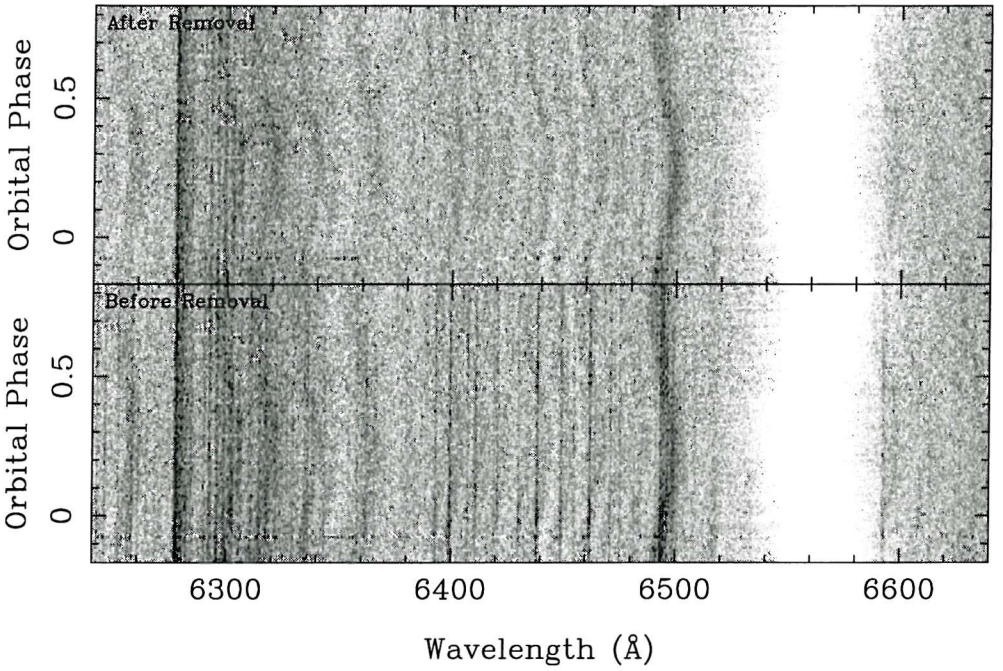

Figure 3.6: Trailed spectra of EM Cyg both before (bottom) and after (top) removal of the contaminating star spectrum.

tra to create Doppler maps, see chapter 6). This is equivalent to integrating along the parameter paths $0 < K < 1000\,\mathrm{km\,s^{-1}}$ and $0 < \phi < 1$, and then plotting the line integrals in velocity space, using K as the radial coordinate, and ϕ_0 as the polar angle. Using this procedure, a visible mass donor would be expected to manifest itself at coordinates $(0,K_2)$ in the resulting velocity-space plot. The cross-correlation template which produces the strongest peak gives the best skew map. The left-hand panel of Fig. 3.7 shows the skew map obtained before any attempt was made to subtract the narrow absorption lines due to the third star. It is obvious that the narrow absorption lines are dominating the skew map, and their measured radial velocity ($\sim 20\,\mathrm{km\,s^{-1}}$) – which to some extent is being pulled up by the true mass donor – puts the peak almost at the origin of the coordinates. The overlaid contours indicate the presence of another peak in the skew map at $\sim 200\,\mathrm{km\,s^{-1}}$on the y-axis. This is the actual mass donor in EM Cyg manifesting itself. The right-hand panel of Fig. 3.7 shows the back-projected cross-correlation functions after attempting removal of the narrow absorption line spectrum. The template spectrum used for the cross-correlation procedure was artificially broadened to the measured rotational

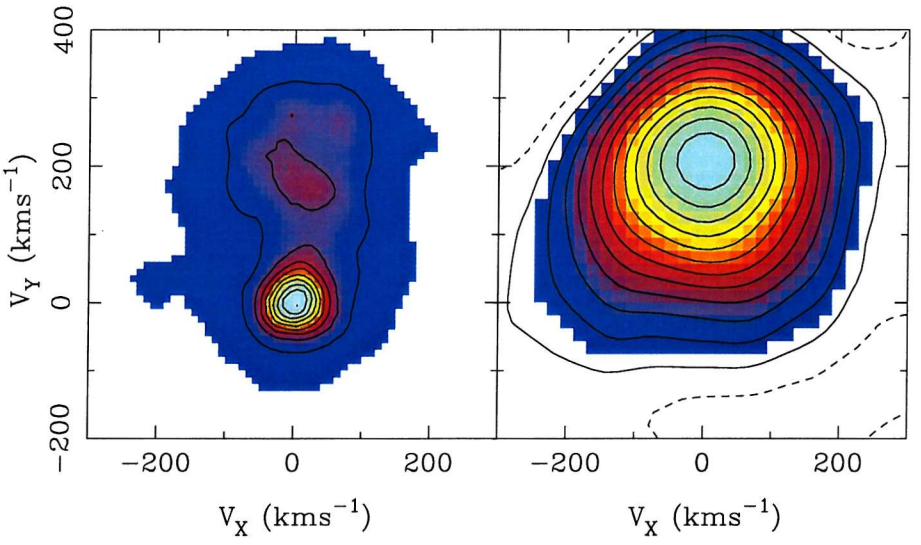

Figure 3.7: Skew map before (left) and after (right) subtraction of third star

velocity of the mass donor in EM Cyg (section 3.2.3). The peak produced by the contaminating spectrum has disappeared from the skew map, and the only peak remaining is that from the actual mass donor in the CV.

3.2.2 Radial velocity of the donor star

Once the individual spectra of EM Cyg had been corrected for the presence of the third star, the radial-velocity amplitude of the actual mass donor could be calculated. The corrected EM Cyg spectra were cross-correlated (using the method of Tonry & Davis, 1979) with the radial-velocity standards each of which had been artificially broadened. The resulting radial velocity curves were then fitted with circular orbit fits of the form given in equation (1.14). Then each EM Cyg spectrum was shifted to correct for the orbital motion of the donor star, and the results averaged. This gave the average spectrum of EM Cyg in the rest frame of the mass donor (upper spectrum of Fig. 3.2), which clearly shows the rotationally broadened absorption lines from the donor, especially in the wavelength region 6350 Å – 6540 Å. Next, this spectrum was cross-correlated once again with the velocity standards and the relative shifts computed and applied. Then a constant times each rotationally broadened

standard was subtracted from the average EM Cyg spectrum. The fraction chosen was such that the χ^2 of the residual spectrum was minimised. Plotting the values of χ^2 against the spectral type of the standard star produced a minimum at spectral types around K3. The circular orbit fit for the K3 standard was then shifted out of the contaminant-free EM Cyg spectra, and the optimal subtraction procedure then repeated to check for systematic errors which could appear due to spectral type mismatch. Initially, the spectral type of the mass-donor was estimated by inspection, using the behaviour of the same spectral lines as used for classifying the third star (see section 3.2.1). The absorption line relative strengths were noted between wavelengths 6350 Å and 6540 Å as compared to rotationally broadened versions of the standard stars. Fig. 3.8 shows the apparent best position to place EM Cyg on the plot, in amongst the standard stars whose spectral types range from G8V to M1.5V. Most of the M-dwarfs for which spectra were obtained have been omitted from this diagram simply because it became obvious, both by inspection and from the results of the initial optimal subtraction, that they weren't a suitable spectral-type match to the mass donor in EM Cyg. The spectral features around 6400 Å and 6440 Å in particular, were noticeably different, as was the general shape of the spectrum blueward of 6400 Å.

After this iterative process had been carried out using the standard with the best fit spectral type (broadened according to the measurement of the rotational velocity, which is detailed in section 3.2.3), a revised value for the radial-velocity amplitude of the mass donor star was determined. Fig. 3.9 shows the circular orbit fit to all the data points. The parameters of this fit are given in Table 3.1. The rms error of the fit is $13\,\mathrm{km\,s^{-1}}$.

Fig. 3.10 shows the fractional contribution from the mass donor to the total light as a function of orbital phase. There is no obvious variation in the fraction contributed by the mass donor around the orbital period. Also, there appears to be no obvious decrease around phase 0.5, which indicates that irradiation of the donor star by the white dwarf is not important. This is confirmed by the lack of any

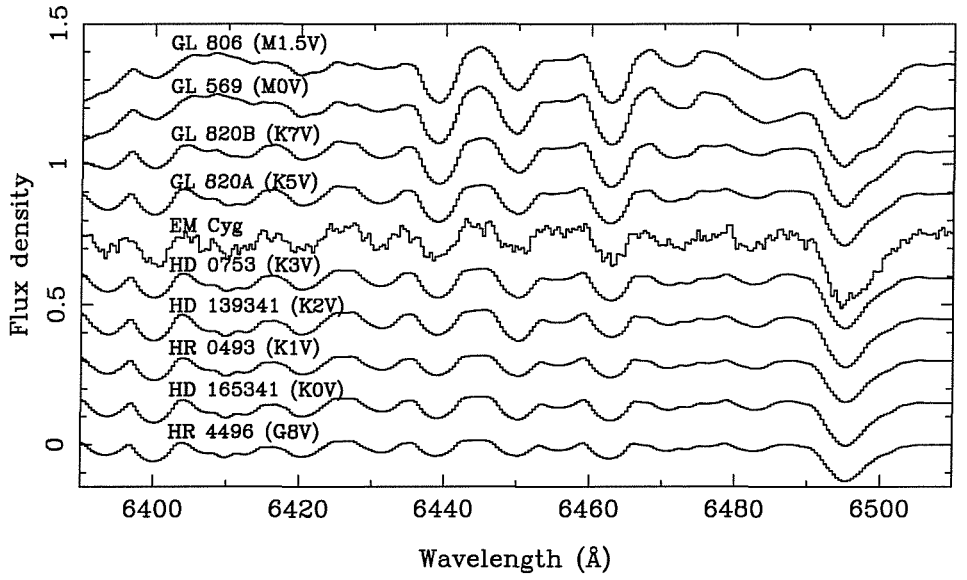

Figure 3.8: The average Doppler-corrected spectrum of EM Cyg after removal of the third star scaled to show the absorption lines in the wavelength region of 6390 – 6510 Å, placed in an apparently suitable position between spectral types K3V and K5V. The sensitivity of the relative depth of the blends at 6400 Å & 6440 Å with effective temperature is very apparent.

Table 3.1: Orbital elements and derived parameters for EM Cyg

Element	Mass Donor[a]	White Dwarf[b]
K ($\mathrm{km\,s^{-1}}$)	202±3	170±10
γ ($\mathrm{km\,s^{-1}}$)	-25±2	-57±7
T_0 ($JD\odot$)	2450621.482±0.001	2443697.128±0.003
$\mathrm{M\sin^3}i$ ($M_\odot$)	0.77±0.08	0.48±0.06

[a]Reference: this paper

[b]Reference: Stover et al. (1981)

obvious distortion of the radial velocity curve (see Fig. 3.9), especially around phases 0.25 – 0.75, compared with, for example, the distortion seen in the radial velocity curve of HS1804+6753 (Billington et al., 1996). A weighted least-squares fit to the data points in Fig. 3.10 gives the mean fraction contributed by the mass donor over the orbital period as 0.231±0.005. For normalised spectra, the value obtained from the optimal subtraction process for the constant which the standards are multiplied by, is equivalent to the fractional contribution of the mass-donor star to the total light. Therefore the mass donor contributes 23 ± 0.5 per cent of the light in the R-band wavelength region.

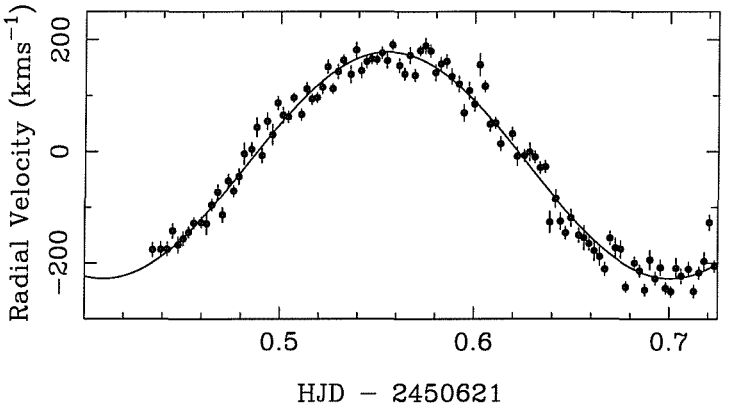

Figure 3.9: The 102 measured mass-donor velocities are indicated by the data points. The solid line is the fit to these points, details of which are given in Table 3.1.

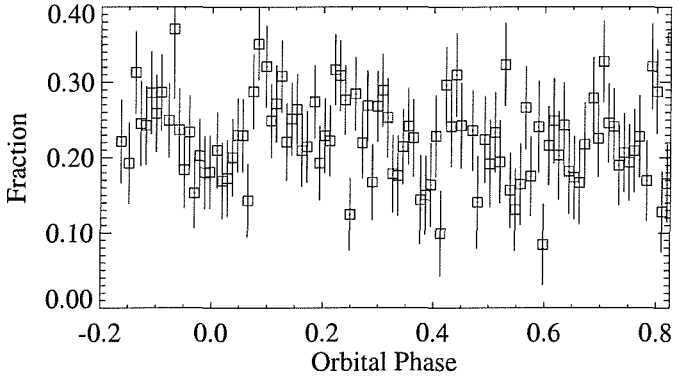

Figure 3.10: The fractional contribution to the total light by the donor star calculated using normalised spectra.

3.2.2.1 Explaining previous radial velocity results

The data used by Stover et al. (1981) to calculate the radial velocity amplitude of the mass donor in EM Cyg had a dispersion of 2.1 Å pixel^{-1}. To check that the higher resolution of the EM Cyg data made the difference as far as detecting the contaminating spectrum was concerned, the raw data were blurred to the Stover et al. (1981) dispersion, and then the cross-correlation procedure repeated to investigate the resulting radial velocity amplitude. Figure 3.11 shows the result of this analysis. The data could be fit by a sinusoid of amplitude 135 km s^{-1} and orbital period $P_{\rm orb} = 6.98$ hours. This test conclusively shows that the resolution

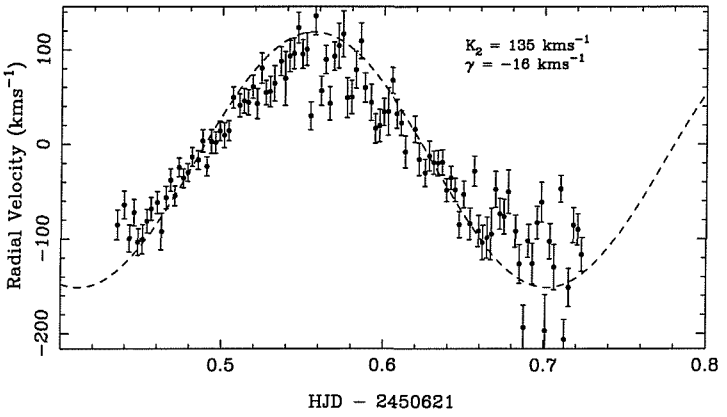

Figure 3.11: The radial velocity curve resulting after the data was blurred to the resolution used by Stover et al. (1981)

of previous data sets could be the only reason why this contamination hasn't been noticed before.

3.2.3 Rotational velocity of the donor star

The rotational broadening of the donor star was estimated by shifting the radial velocity fit determined in the previous section out of each EM Cyg spectrum, and then co-adding the results to produce a spectrum of the star in the rest frame of the mass donor (see Fig. 3.2). This average spectrum was then cross-correlated with the standard stars, whose spectra had been artificially broadened by a range of velocities (10 – 200 km s^{-1} in steps of 10 km s^{-1}). Both the object and standard star spectra were normalised in the continuum. The radial-velocity standard spectra were then shifted by an amount determined from the correlation. A constant times each broadened standard spectrum was then subtracted from the object spectrum, to produce a residual spectrum. Then a smoothing coefficient was applied to the difference spectrum in order to remove any large scale features. The χ^2 of the result was computed in the region containing the absorption line features (6390 – 6510 Å). The resulting curves of χ^2 versus the value of the rotational broadening used are shown in Fig. 3.12, for the spectral types from K1 to K7.

Table 3.2: Rotational broadening from model line profiles

Inclination[a]	Limb Darkening[b]	$v \sin i$ ($\mathrm{km\,s^{-1}}$)
69°	0	147±4
69°	0.5	140±3
69°	1	130±3

[a]Inclination value taken from literature, our preferred value is determined in section 3.2.4.

[b]Gravity darkening taken to be 0.08, mass ratio 0.88 assumed

From Fig. 3.12 it is possible to deduce a value for the rotational broadening and an estimate of the spectral type of the mass donor. Fig. 3.12 also shows that the systematic error due to using different spectral types to obtain values for $v \sin i$ is less than $10\,\mathrm{km\,s^{-1}}$. The minimum χ^2 is obtained for $v \sin i = 140 \pm 3\,\mathrm{km\,s^{-1}}$ and spectral type K3V.

Another systematic effect to be taken account when calculating the rotational broadening of the mass donor is its non-spherical shape. The size of this effect was estimated by computing model absorption profiles including the effects of Roche geometry and system parameters appropriate for EM Cyg. These profiles were then used to broaden a K3 standard star. The $v \sin i$'s of the resulting simulated spectra were then estimated using the same procedure applied previously to the data. The parameters of Table 3.3 were used to define the Roche lobe (i.e. $q = 0.88$, $K_1 + K_2 = 372\,\mathrm{km\,s^{-1}}$), and the method outlined by Marsh, Robinson & Wood (1994) was used. Table 3.2 shows the results of this process and demonstrates that the distortion of Roche lobe geometry has a negligible effect since we recover $v \sin i = 140\,\mathrm{km\,s^{-1}}$ for our assumed limb darkening of 0.5. However, one can see that increasing the value of the limb darkening parameter used to calculate the rotational broadening of the lines from the mass donor makes the star appear smaller, and introduces a systematic error of the order $10\,\mathrm{km\,s^{-1}}$. In all subsequent analysis the value used for the linear limb-darkening parameter was 0.5. In addition, the systematic error introduced by altering the linear limb-darkening parameter whilst artificially

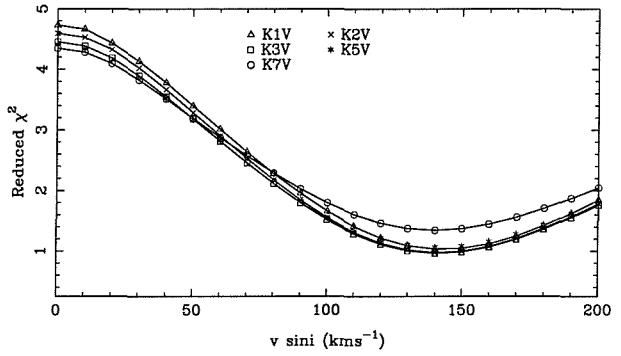

Figure 3.12: A plot of the χ^2 curves obtained using different spectral type standards, which show that the minima occur at a $v \sin i$ value around $140\,\mathrm{km\,s^{-1}}$.

broadening the standard stars was also accounted for. Using a value of 0 for the linear limb-darkening parameter with the best fit standard discovered from Fig. 3.12, the measured $v \sin i$ dropped to $135 \pm 6\,\mathrm{km\,s^{-1}}$. With the limb darkening set to 0.5, the value increased to $140 \pm 3\,\mathrm{km\,s^{-1}}$, an error of magnitude $5\,\mathrm{km\,s^{-1}}$. Accounting for these possible sources of error, we adopt a value for the rotational broadening of the mass donor, $v \sin i$, of $140 \pm 6\,\mathrm{km\,s^{-1}}$. From the $v \sin i$ curves of Fig. 3.12, and the relative depths of the absorption lines, the spectral type of this star is found to be K3V.

3.2.4 New system parameters

The main result of this study has been to discover that the spectrum of EM Cyg is contaminated by light from a star with a very similar spectral type to its own mass donor. Removal of the contamination by this star from the spectral lines in the region blueward of Hα increases the measured amplitude of the radial velocity curve of the mass-losing star by over $60\,\mathrm{km\,s^{-1}}$, effectively removing the problem previously associated with EM Cyg: that the system should be in a state of dynamically unstable mass transfer. Table 3.3 shows the re-measured orbital elements, and those parameters which can be derived from them.

The range for the inclination i, shown in Table 3.3 was deduced as follows. A

Table 3.3: New orbital and derived system parameters for EM Cygni

Orbital Elements[a]		
Name	Value	Reference
Period (days)	0.290909±0.0000042	Robinson (1974)
K_2	202±3 km s^{-1}	this thesis
K_1	170±10 km s^{-1}	Stover et al. (1981)
K_1	171±4 km s^{-1}	this thesis
T_0 ($JD_\odot$)(2450621+)	0.483±0.001	this thesis
γ (km s^{-1})	-25±2 km s^{-1}	this thesis
$a \sin i$ (cm)	$(1.52 \pm 0.04) \times 10^{11}$	this thesis
Derived System Parameters		
$v \sin i$ (km s^{-1})	140±6	this thesis
q (=M_2/M_1)	0.88±0.05	this thesis
$M_2 \sin^3 i$ ($M_\odot$)	0.77±0.08	this thesis
$M_1 \sin^3 i$ ($M_\odot$)	0.88±0.05	this thesis
inclination, i (degrees)	$61° \leq i \leq 69°$	this thesis
M_2 ($M_\odot$)	0.99±0.12	this thesis
M_1 ($M_\odot$)	1.12±0.08	this thesis
R_2 ($R_\odot$)	0.87±0.07	this thesis

[a] e = 0 (assumed)

simulated Hα trailed spectrum was created using the system parameters determined previously (namely q and K_1+K_2 as 0.88 and 372 km s^{-1} respectively) over the phase range covered by the actual data, i.e. phases −0.165 to 0.825. The power law used for the intensity over the disc as a function of radius was -1.5, and the velocity limits of the plots were ±1500 km s^{-1}. The outer disc radius used was $0.8R_{L_1}$. The eclipse of the disc in the simulated Hα trail becomes visible at inclination angle, $i = 61°$. The inclination angle at which the eclipse matches that seen in the actual data is $i = 67°$. At $i = 70°$, the white dwarf is eclipsed, but it is apparent from our data that we are not observing an eclipse of the white dwarf (Robinson, 1974). This places an upper limit to the inclination of 70°. No part of the primary Roche lobe is occulted for inclinations less than 61°, thus placing a firm lower limit on i, higher than that reached by Robinson (1974). Henceforth, we adopt a value of $i = 67° \pm 2°$ to cover the range where the uncertainty should be interpreted as a 1σ estimate.

The radial-velocity amplitude of the white dwarf star was checked using the double Gaussian technique developed by Schneider & Young (1980). The line wings are used to determine the radial velocities because they form in an area which is close to the white dwarf and so disruption of symmetry by the gas stream and mass donor star are minimised. Twin Gaussians (200 km s^{-1} FWHM) with separations varying from 1200 – 1800 km s^{-1} were used. This procedure gave consistent values of the white dwarf radial velocity amplitude $K_1 = 171 \pm 4$ km s^{-1}, in agreement with that obtained by Stover et al. (1981). The systemic velocity measured from the radial velocity curve fits was $\gamma = -26 \pm 5$ km s^{-1}, consistent with that obtained from the mass donor analysis. The emission line radial-velocity curves were measured to be delayed by $10° \pm 3°$ from being in anti-phase with with the donor star.

3.2.5 Masses

The measurements of $v \sin i$ and K_2 can be used to deduce the mass ratio $q = M_2/M_1$. Assuming that the donor star rotates synchronously then

$$\frac{v \sin i}{K_2} = \frac{R_L(2)}{a}(1+q). \tag{3.1}$$

The relative size of the donor star is constrained by Roche geometry to be (equation 1.8)

$$\frac{R_L(2)}{a} = \frac{0.49q^{2/3}}{0.6q^{2/3} + \ln(1+q^{1/3})}, \qquad \text{for } 0 < q < \infty,$$

Eggleton (1983). Applying these equations we find $q = 0.88 \pm 0.05$. This is consistent with that found from K_1: $q = K_1/K_2 = 0.84 \pm 0.06$, but we prefer the value determined from $v \sin i$ as K_1 measurements often suffer distortions (Stover, 1981a).

The values obtained here for K_2, q (derived from the rotational broadening measurement) and i can be combined with the orbital period obtained by Robinson (1974) to calculate the masses of each component using:

$$M_1 = \frac{P_{\rm orb} K_2^3 (1+q)^2}{2\pi G \sin^3 i} \tag{3.2}$$

$$M_2 = \frac{P_{\rm orb} K_2^3 (1+q)^2 q}{2\pi G \sin^3 i}. \tag{3.3}$$

The values obtained are shown in Table 3.3. Assuming the inclination value concluded in the previous section, $i = 67° \pm 2°$, we calculate component masses of $M_1 = 1.12 \pm 0.08 M_\odot$ and $M_2 = 0.99 \pm 0.12 M_\odot$. The value for the white dwarf mass is consistent with those given for other Z Cam systems (Ritter and Kolb, 1998). However, the mass for the donor star is close to that of the Sun, which is a G2V star, compared with our observed K3 spectral-type (Allen, 1973). Beuermann et al. (1998) discuss whether the mass donor stars in CVs are main-sequence stars, using relationships between spectral type and orbital period in a sample of CVs. They show that the donor stars in CVs with shorter orbital periods fit the 'unevolved' evolutionary tracks well, whilst those at longer periods tend to fit 'evolved' models better. EM Cyg with its orbital period of 6.98 hours, and mass donor spectral type of K3, fits on the plot nearer to the 'moderately evolved main-sequence' track, indicating that EM Cyg may have an evolved mass donor, as it appears to be oversized and over-massive for its spectral type. The radius of the mass donor is $R_2 = 0.87 R_\odot \pm 0.07$ which compares with $0.74 R_\odot$ for a K5V star, and $0.85 R_\odot$ for a K0V star (Allen, 1973), indicating that it is oversized compared to a main-sequence star of the same spectral type. However, the mass deduced for the donor star ($0.99 \pm 0.12 M_\odot$) is not consistent with its spectral type according to the current theoretical models of Kolb & Baraffe (2000). Their stellar models only become as cool as K3 for a donor star mass of $\lesssim 0.85 M_\odot$, and this is only if the mass loss rate has been rather high (and the mass donor is unevolved). In addition, they show

that if the mass donor is 'evolved' it would have a slightly earlier spectral type than a ZAMS star with a mass of 1 $M_{\odot}$. In summary, the new system parameters appear to be inconsistent with the current CV mass-donor models.

3.2.6 The third star

A third star contaminating the spectral region around Hα wavelengths in EM Cyg has been identified, causing the absorption lines in this area to appear narrow, with none of the broadening present which is associated with the actual mass donor. The spectral type of this third star has been identified as K2V - K5V, which is similar to that of the mass donor. It also contributes a similar percentage of light to the spectrum of EM Cyg as the actual mass donor. The third star contributes a fraction 0.160±0.002 to the light of EM Cyg at Hα wavelengths, whilst that contributed by the mass donor is 0.231±0.005. Once this third star has been accounted for, the measurements for the radial velocity amplitude increase (from $135 \pm 3\,\mathrm{km\,s^{-1}}$ to $202 \pm 3\,\mathrm{km\,s^{-1}}$) and the mass ratio of EM Cyg falls below one, removing the conflict with the theory. The amplitude of the radial velocity curve for the white dwarf is $171 \pm 4\,\mathrm{km\,s^{-1}}$, which agrees with the value $170 \pm 10\,\mathrm{km\,s^{-1}}$ given by Stover et al. (1981), and which gives a mass ratio of q=0.85±0.03 $\mathrm{km\,s^{-1}}$. The radial velocity of the centre-of-mass of the binary from the absorption line measurement is $-25 \pm 2\,\mathrm{km\,s^{-1}}$. The radial velocity of the contaminating spectrum ($-20 \pm 3\,\mathrm{km\,s^{-1}}$) is also consistent with this value which implies that the third star and EM Cyg may be physically associated. In addition, the similarity of spectral type and fractional contribution to the spectrum of EM Cyg indicates that the third star and the CV may be at similar distances. However, the field of EM Cyg is quite a crowded one, and so a chance superposition is also plausible. To address this some direct images were acquired on the William Herschel Telescope which have a FWHM of 0.7 arcsec, but still the third star could not be resolved (see section 3.4.1 for details).

3.2.7 The accretion disc

The value of a sin i obtained with the new amplitude and mass-ratio values is 1.52×10^{11}cm. Assuming Keplerian motion in the disc, then

$$\frac{r_{\rm d}}{R_{L_1}} = \frac{a}{R_{L_1}} \frac{GM_1 \sin^3 i}{a \sin i (V_{\rm d} \sin i)^2}, \tag{3.4}$$

where $\rm R_{L_1}$ is the distance from the centre of mass of the white dwarf to the inner Lagrangian point and is equal to $0.51a$ for $q = 0.88$. Using the determined values of $\rm M_1 \sin^3 \mathit{i}$=0.88±0.05$\rm M_\odot$, a sin $i = (1.52 \pm 0.04) \times 10^{11}$ cm, and the outer disc velocity, $V_{\rm d}$ sin i as $305 \pm 30\,{\rm km\,s^{-1}}$ we calculate a value of $\rm r_d/R_{L_1} = 1.61$. This is physically impossible as it implies that the disc must occupy space outside the Roche lobe of the white dwarf. For a more believable disc radius of $0.8\rm R_{L_1}$, the predicted outer disc velocity, using equation 3.4 is $430\,{\rm km\,s^{-1}}$. Stover et al. (1981) measured the half-separation of the peaks of the Hβ line to be $390 \pm 15\,{\rm km\,s^{-1}}$, giving an outer disc radius of $0.98\rm R_{L_1}$, still too large, but not as discrepant as that found for Hα, for which we have no explanation.

3.2.8 Evolutionary considerations

Smith & Dhillon (1998) plot the mass (in solar mass units) versus the spectral type of the mass donor in a sample of CVs. EM Cyg is on this plot with a spectral type of K5V, and a mass of $0.76 \pm 0.10 M_\odot$. Figure 3.13 shows the points used by Smith & Dhillon, and the new position of EM Cyg as calculated in this chapter. The new value of $\rm M_2$ puts the system above where it should be were it a main-sequence star, confirming that the mass donor in EM Cyg must be evolved. If the third star is actually physically associated with EM Cyg, then this would make it only the second CV known to be in a triple system (Reimers et al., 1988).

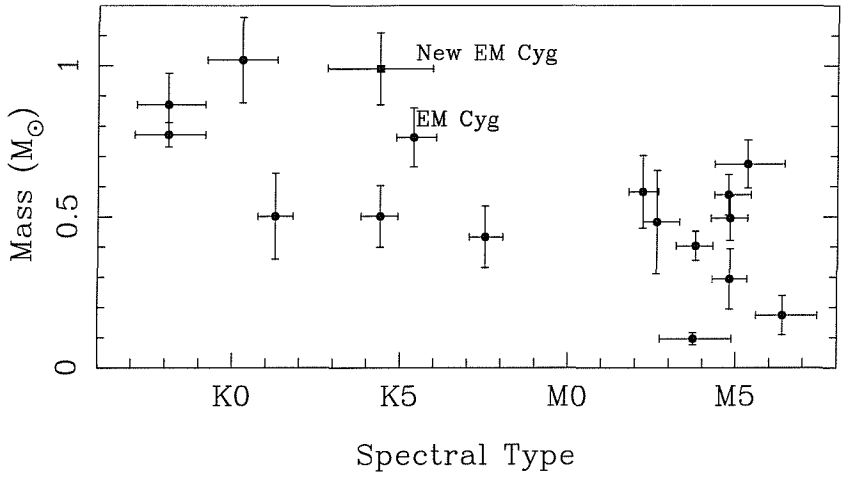

Figure 3.13: Mass versus Spectral type for the mass donors in several CVs. Data points are from Smith & Dhillon (1998)

3.3 Is the third star physically associated with the CV?

The initial results of this analysis indicate that the third star may be physically associated with the CV (section 3.2). The similarity of the systemic velocities and the brightness of both the mass donor in the CV and the third star are possible indicators of a physical connection. The configuration of a CV (an evolved white dwarf in a close orbit with a main-sequence star) places restrictions on the prior evolution of the binary star. The presence of a $\sim 1\,M_\odot$ white dwarf means that its progenitor star must have reached the giant stage in its evolution (i.e. had a radius over a hundred times the current binary separation). The current picture to deal with this apparently implausible evolution is that a common-envelope phase is experienced by the system. The evolving star reaches the asymptotic giant branch (AGB), and transfers mass to its main-sequence companion very quickly. Due to the inability of the main-sequence star to respond fast enough to this mass influx, the transferred matter forms a single envelope around the two stars (Paczynski, 1976). Tidal interactions between the binary star and this envelope cause the transfer of orbital angular momentum, and energy, to the envelope ultimately resulting in its expul-

sion. This can cause reduction of the orbital period from greater than hundreds of days to a period of only hours in length. There is little direct evidence to support this theory though. The common envelope phase is expected to be short-lived, and whilst a binary star is going through this phase it probably will not be able to be observationally distinguished from a single AGB star in any case. In addition, subsequent evolution of CVs tends to eradicate evidence that this process occurred at all. Until recently, there has been only one system which could provide direct constraints on the prior evolution of the CV; triple-system 4 Draconis (hereafter 4 Dra) (Reimers et al., 1988; Eggleton et al., 1989). 4 Dra is an M-giant at a distance of some 100 pc which was found to be part of a spectroscopic binary star with an invisible companion at optical wavelengths. Ultra-violet data implied that this companion was in fact a CV. The orbital period of the system, 1703 days, is long, however this does put considerable constraints upon the maximum separation of the precursor to the CV. Due to the faintness of the CV, and the dominance of the M-giant, calculation of the masses of the components in the CV is unlikely. In EM Cyg however, the CV component masses have been measured here in this chapter. The white dwarf in EM Cygni has a mass $1.12 \pm 0.08\,M_{\odot}$, which implies it must have reached the AGB. Hurley, Pols & Tout (2000) plot the relation between the final object mass and its progenitor zero-age main sequence (ZAMS) mass, as shown in Fig. 3.14. Therefore, the precursor to the current white dwarf must have had a mass of $\gtrsim 6M_{\odot}$. The mass donor in the current CV has a mass of $0.99 \pm 0.12 M_{\odot}$, and from its spectral type (section 3.2.2) the third star has a mass of $\sim 0.7 M_{\odot}$ (Allen, 1973). So the total system mass must have changed from $\gtrsim 7.7 M_{\odot}$ to the current value of $\sim 2.8 M_{\odot}$. Assuming that the mass lost by the CV (and also any by the third star) carries off the same amount of angular momentum per unit mass as resides in the orbital motion of the star it was lost from, and that this process is sufficiently slow that the eccentricity of the orbit and the reduced angular momentum are left unaltered leads to

$$P_{\rm orb} \propto m^{-2},\ a \propto m^{-1} \tag{3.5}$$

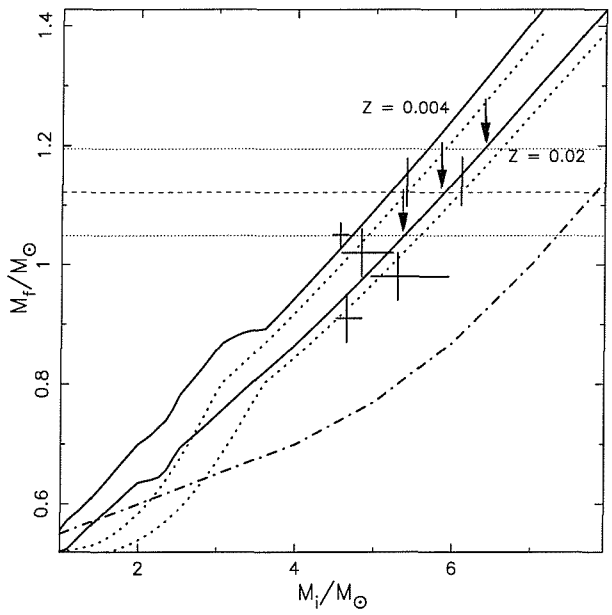

Figure 3.14: Relation between white dwarf mass and ZAMS mass of the progenitor (the initial-final mass relation). Arrows indicate the corresponding progenitor masses given the white dwarf mass calculated. Adapted from Hurley, Pols & Tout (2000)

where m is the total mass So, the separation of the third star and CV can be expected to have increased by a factor 2.8 due to this loss of mass.

In order to prevent the precursor to the white dwarf transferring mass onto its companion before reaching the peak of the giant branch, the radius of its Roche lobe must have been large enough to accommodate it. Using equation (1.8) to determine the effective radius of the Roche lobe, R_L, needed in order to fully enclose a star in a binary with mass ratio, $q = 6.06$ (ratio of would-be mass-losing star to would-be mass-gaining one) gives $R_L = 0.537a$. The mass of this AGB star can be determined from the mass of the white dwarf which remains. The $1.12M_\odot$ white dwarf formed from the core of the AGB star. Hurley, Pols & Tout (2000) present analytic formulae which approximate the evolution of stars over a wide range of mass and metallicity values. The following analysis uses these formulae to deduce the radius of the star at the tip of the giant branch. Hurley, Pols & Tout (2000) state that the luminosity at the end of the giant branch is equivalent to L_{HeI}, the luminosity at the time of

helium ignition.

$$L_{HeI} = \frac{b_{11}+b_{12}M^{3.8}}{b_{13}+M^2} \quad M \geq M_{HeF} \tag{3.6}$$

where all the constants are as given in Hurley, Pols & Tout (2000). For EM Cyg, $M > M_{HeF}$ and so we use equation 3.6 to calculate the luminosity of the precursor to the white dwarf at the time of helium ignition. Assuming solar metallicity, the constants are $b_{11} = 11486.2234, b_{12} = 734.8793$ and $b_{13} = 84.9954$, and so $L_{HeI} = 5595.3683 L_{\odot}$, from equation 3.6). The radius at helium ignition is then $R_{HeI} = R_{GB}(M, L_{HeI})$ for $M \leq M_{FGB}$. M_{FGB} is the maximum initial mass for which helium ignites on the first giant branch, and for EM Cyg $M < M_{FGB}$. The radius to which this luminosity corresponds, assuming solar metallicity, is given by

$$R_{GB} \approx 1.1 M^{-0.3} \left(L^{0.4} + 0.383 L^{0.76}\right) \tag{3.7}$$

(Hurley et al., 2000). Therefore the precursor to the white dwarf in the CV must have had a radius of at least $194 R_{\odot}$. Therefore the separation of the two stars in the precursor to the CV must have been greater than 1.7 AU.

Eggleton & Kiseleva (1995) determine the stability criterion for hierarchical triple systems, that

$$Y_0^{min} = 1 + \frac{3.7}{q_{out}^{1/3}} + \frac{2.2}{1+q_{out}^{1/3}} + \frac{1.4}{q_{in}^{1/3}} \frac{q_{out}^{1/3}-1}{q_{out}^{1/3}+1} \tag{3.8}$$

where Y_0^{min} is the critical initial ratio of the periastron distance of the outer orbit to the apastron distance of the inner orbit. The ratios q_{in} and q_{out} are the inner-binary and outer-binary mass ratios respectively.

$$q_{in} = m_1/m_2 > 6.06, \quad q_{out} = (m_1+m_2)/m_3 > 9.99 \tag{3.9}$$

Therefore, using equation (3.8) to determine the stability criterion for the progenitor to EM Cyg, the outer binary (CV-progenitor plus K-star) must have been at least 3.8 times as large as that of the inner binary star (CV-progenitor). Allowing for the expansion of the orbit in the subsequent mass loss (from equation 3.5) means that

the present day separation of the CV and third star must be at least 18 AU. At the distance of EM Cyg ($\sim 300\,\mathrm{pc}$ (Jameson et al., 1981)), 18 AU corresponds to 0.06″ on the sky. Using Kepler's Third Law, the expected amplitude of the radial-velocity curve for the third star can then be estimated. Kepler's third law states

$$\frac{GM_{\mathrm{total}}}{a^3} = \frac{4\pi^2}{P_{\mathrm{orb}}^2} \tag{3.10}$$

and so it is known that the separation between the third star and CV is proportional to the cube-root of the total mass of the triple system multiplied by the square of the cube-root of the orbital period. The CV mass has been determined in section 3.2.5 as 2.11 $M_{\odot}$. Assuming the third star is a main-sequence star with a spectral type of K3, then we can expect it's mass to be 0.7 $M_{\odot}$. From equation (3.10) one estimates an orbital period, P_{orb} of ~ 45 years using the minimum separation calculated (18 AU). The amplitude of the radial-velocity curve that is expected is

$$K_K = \frac{2\pi a}{P_{\mathrm{orb}}} \sin i \left(\frac{M_{CV}}{M_{CV} + M_K}\right) \tag{3.11}$$

which gives $K_K \approx 8\,\mathrm{km\,s^{-1}}$, assuming that $\sin i = 90$. At best, the effect to be measured could be as little as only a few kilometres per second over a period of tens of years.

3.4 Further investigation into the nature of EM Cyg

In semester 1999A, 5.5 hrs of bright service time were allocated to observe EM Cyg with the WHT (see chapter 2), in order to determine whether the third star is physically associated with the CV in EM Cyg. The proposal involved two stages. The first was to use auxiliary port (hereafter, aux port) imaging to obtain U,B,V,R,I images to try and resolve the third star by detecting a wavelength-dependent shift

of the CV on the images. If this was not successful at resolving the stars, then UES spectroscopy was to be acquired in order to attempt to detect orbital motion of the third star.

3.4.1 Imaging

Auxiliary port (Cassegrain) imaging on the WHT was chosen for the next stage of the investigation in order to obtain accurate astrometry of EM Cyg. Accurate photometry was not required – the aim was to try and detect a wavelength-dependent shift between EM Cyg and the third star relative to nearby stars.

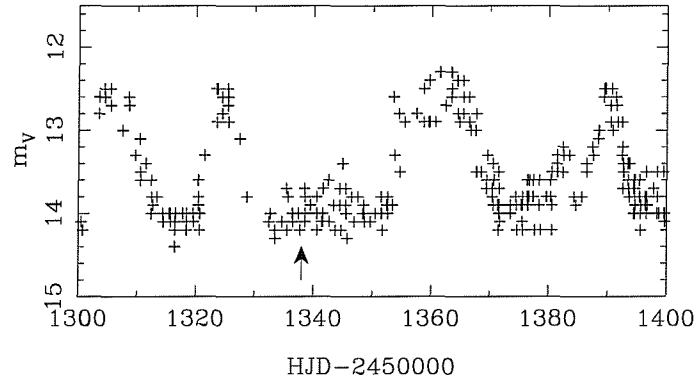

Figure 3.15: The visual magnitude of EM Cyg in the 100 days around the observations. Data from Mattei (2000)

The important factor for these observations was that EM Cyg was *not* undergoing an outburst whilst they were being carried out. Otherwise, the flux from the third star would be swamped by that from the accretion disc. The light curve of EM Cyg around the time of the observations is shown in Fig. 3.15. The arrow indicates the date on which the aux port imaging was taken. The observations appear to have been taken about 10 days before the start of the next outburst.

As measured in section 3.2.1, the contribution in the R-band ($\sim$ 6500Å) from the third star was 16 per cent, and it's spectral type K3–5V. Using the information given in Johnson (1966), and assuming that the third star is on the main-sequence,

Table 3.4: Comparison stars in the field of EM Cyg whose positions were measured

Number	ID	RA (2000)	dec (2000)	Vmag	Bmag
1	U1200_12415370	19:38:39.1	+30:30:31.2	16.7	17.6
2	NOT	IDENTIFIED	IN	USNO	
3	U1200_12418260	19:38:41.129	+30:30:18.3	15.9	16.6
4	NOT	IDENTIFIED	IN	USNO	
5	NOT	IDENTIFIED	IN	USNO	
6	U1200_12419020	19:38:41.7	+30:30:35.0	14.1	14.9
7	U1200_12417843	19:38:40.8	+30 30 30.5	17.3	18.3

results in a contribution of approximately zero per cent in the U-band, rising up to $\sim$ 30 per cent in the I-band. So if the CV and the third star are separated by s, then we can expect to detect a shift on the images, from U to I, of magnitude $\sim 0.3s$. With the 0.11″ pixels on the aux port CCD, positions can be measured to within 1/20th of a pixel, therefore detecting a shift of 0.01″ is entirely feasible. The colours of the field stars near to EM Cyg are all different, of course, so observations were requested at three differing airmasses, to allow for any differential refraction effects. Unfortunately, the 'three different airmasses' were all within 0.1 airmasses of the zenith, and so no correction for this effect could be applied. Images of the field centred on EM Cyg were taken in the U,B,V,R and I broad-band filters as described in chapter 2. The aux port delivers a circular field-of-view of diameter 1.8′, which when centred on EM Cyg gave seven reasonably bright comparison stars within a 280 × 165 pixel frame, with which to calculate accurate positions. These stars were recorded in the US Naval Observatory (USNO) catalogue, and their identifications are given in Table 3.4. Figure 3.16 shows the $\sim$ 2′ × 2′ field around EM Cyg, illustrating how the CV lies in a rich star field. The CV is indicated on the figure. The dashed line linking EM Cyg to another star (numbered six) approximately 23″ distant on the frame shows the orientation of the slit for the IDS/500-mm observations. This translates to a separation of $\sim$ 70 pixels on the TEK CCD, which agrees with the positions measured spatially on the chip. This image was taken through the Harris V filter, whose central wavelength is 5461Å. EM Cyg is the brighter object which is marked in the image. The celestial coordinate axes

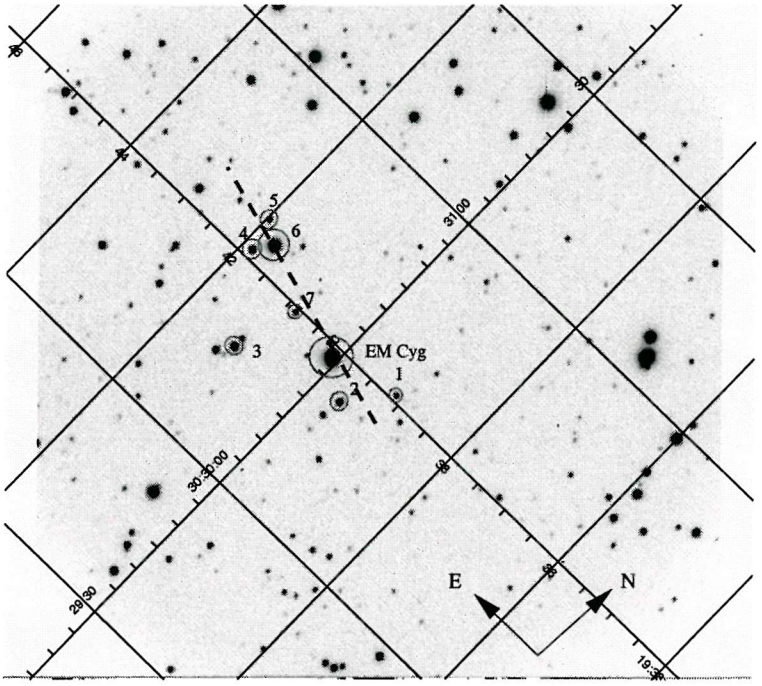

Figure 3.16: An example image from the auxiliary port.

have been overlaid onto the image, and all the objects identified as stellar have been circled. For accurate position measuring the STARLINK package GAIA was used (see section 2.1.2.2 for details.) Only the brightest eight (including EM Cyg) objects were measured on the images. However, one of these stars was affected by bad pixels on the CCD chip (number 6), and so it was not included in further analysis. From the set of images taken, no significant shift could be detected at a level of 0.2″, so UES spectroscopic observations were requested.

3.4.2 Echelle spectroscopy

Due to the absence of a detection of any wavelength-dependent shift on the aux port imaging, the second phase of the proposal was set in motion. This involved using the Utrecht Echelle Spectrograph (hereafter, UES) on the WHT to obtain spectra of EM Cyg at one of the quadrature phases of the CV in service mode. Choosing observations to happen at those particular phases means the absorption lines of the

Table 3.5: Results from the Imaging. All pixel measurements are quoted to within 0.01 pixels

Filter & frame number	EM Cyg	Star 1	Star 2	Star 3	Star 4	Star 5
U-2004	99.34	140.32	97.07	51.84	124.75	149.51
U-2005	97.87	138.40	95.22	51.81	124.85	149.62
U-2010	94.03	132.25	89.07	55.90	128.34	152.54
U-2015	91.76	129.19	86.29	55.30	128.51	152.71
B-1997	104.89	146.74	103.69	52.85	124.80	150.03
B-1998	103.87	145.45	102.49	52.84	125.05	150.22
B-2006	94.86	135.83	92.51	49.67	122.91	147.67
B-2011	92.10	130.71	87.41	53.51	126.82	151.08
V-2000	103.37	144.03	100.80	55.13	127.70	152.63
V-2007	95.81	136.08	92.74	51.90	125.11	148.54
V-2012	93.05	131.74	88.48	53.64	126.95	151.23
R-2001	102.96	143.13	100.13	55.07	127.95	152.87
R-2002	102.42	142.79	99.74	54.67	127.48	152.43
R-2008	95.41	135.71	92.64	51.01	124.39	148.82
R-2013	94.34	132.56	89.23	55.67	129.03	153.32
I-2003	99.97	140.32	97.5	52.86	125.40	150.20
I-2009	93.84	133.10	90.18	52.01	125.38	149.61
I-2014	92.02	129.16	86.21	55.66	128.99	153.06

actual mass donor will be at their maximum Doppler-shift from the contaminating star lines, and so should, in principle be easier to resolve. Echelle spectra are high resolution with a large wavelength coverage, in this case, from 4200 Å to $\sim$ 9000 Å. Figure 3.4.2 shows the state EM Cyg was in at the time of the observations. The first two observations are at the very beginning of an outburst, so the data had to be checked to see whether it would be useful. The final observations were done when the CV was in a quiescent disc state.

The datasets were reduced as described in section 2.1.2.4. One spectrum per order was produced using this reduction method. Due to the nature of the data frames (most notably that the higher orders in the arc frame were saturated) it was decided that a single-order operation would be the best way to deal with the data. The next process was to cross-correlate the single-order target observations with observed radial velocity standards. Two of the standards used with the INT data were chosen, GL 820A and HD 219134 (see section 4.2). The cross-correlations were carried out

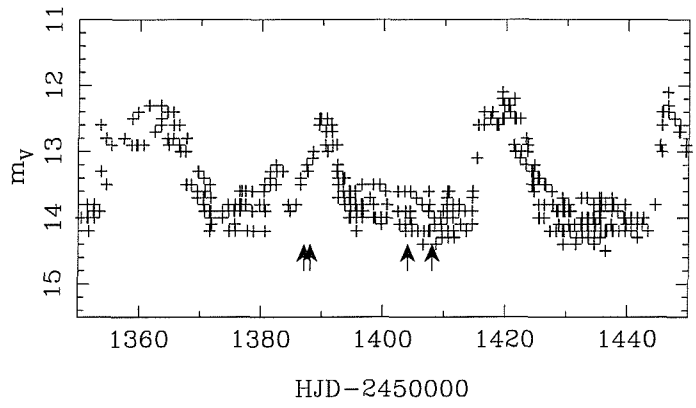

Figure 3.17: Light curve of EM Cyg around the time the echelle observations were made. From Mattei (2000)

in the same way as before, by using the method applied to galaxies by Tonry & Davis (Tonry and Davis, 1979). The resulting radial velocities were corrected for the radial velocity of the standard, and then plotted (see Fig. 3.18). The heliocentric radial velocities determined from this procedure are given in Table 3.6. The radial velocities in Table 3.6 obtained using two different radial velocity standards (HD 219134 and GL 820A) are all quite consistent, apart from a couple of spurious values. These occur in orders 32 and 40. A probable reason for these erroneous values lies in the wavelength scale assignation process. Each order had its wavelength scale fitted individually, but an automated process was used once the basic lines had been identified. A major problem encountered in the data reduction was cosmic ray identification (see chapter 2). This automated process did not contain enough flexibility to allow for the possible presence of potential cosmic rays; it assumes all the lines present are from the arc lamp. For order 40, for example, the radial velocity values which disagree most with the rest are both from August 13th, spectrum number one insinuating that there may be a minor problem with the arc scale. To re-iterate, due to the nature of service observing the data obtained for this part of the investigation were not sufficient for any conclusions about the radial-velocity variations of the third star in EM Cyg to be drawn with confidence. Unfortunately, having requested that each observation was carried out at the same quadrature phase (i.e. 0.25 or 0.75) in order to reduce the probability of introducing systematic error, one of the observations was taken at phase 0.25, whilst the others were taken

Table 3.6: Heliocentric radial velocities for the third star absorption lines

Night number	Spectrum number	Order number[a]	RV ($km\,s^{-1}$)	RV standard
2	1	32	-23.5±0.6	GL 820a
2	2	32	-26.0±0.7	GL 820a
3	1	32	-21.8±0.7	GL 820a
3	2	32	-23.4±0.7	GL 820a
2	1	32	-22.2±0.5	HD 219134
2	2	32	-38.2±0.4	HD 219134
3	1	32	-22.6±0.5	HD 219134
3	2	32	-22.7±0.6	HD 219134
2	1	35	-24.4±0.2	GL 820a
2	2	35	-24.5±0.2	GL 820a
3	1	35	-22.5±0.2	GL 820a
3	2	35	-22.2±0.2	GL 820a
2	1	35	-24.0±0.2	HD 219134
2	2	35	-24.0±0.2	HD 219134
3	1	35	-22.2±0.2	HD 219134
3	2	35	-21.7±0.2	HD 219134

[a]Order 32: 6980-7140Å; Order 35: 6400-6520Å;

at phase 0.75. Figure 3.19 plots the wavelength range 6400 – 6500Å from the echelle spectra. The lines visible here are the same ones as seen in the lower spectrum of Fig. 3.2. The major difference to note here is that the blend at $\sim$ 6500Å in Fig. 3.2 is resolved into a cluster of sharp lines in Fig. 3.19. The contribution from the CV mass donor is still seen here as a broad, shallow dip extending from $\sim 6490-6500$Å. The top two spectra in Fig. 3.19 are from two radial-velocity standard stars, obtained so that radial velocities of the third star absorption lines could be measured.

From the available data so far no firm evidence has been gathered to verify a physical connection between the third star and the CV. The first night's data from the echelle spectrograph was taken as EM Cyg was on the rise to outburst. Therefore, the continuum from the disc was brighter than for the other data, so the spectra were not used to calculate radial velocities.

Table 3.6: Continued...

Night number	Spectrum number	Order number[a]	RV ($km\,s^{-1}$)	RV standard
2	1	40	-43.1±0.1	GL 820a
2	2	40	-24.5±0.2	GL 820a
3	1	40	-22.2±0.2	GL 820a
3	2	40	-22.2±0.2	GL 820a
2	1	40	-42.5±0.1	HD 219134
2	2	40	-23.9±0.2	HD 219134
3	1	40	-21.5±0.2	HD 219134
3	2	40	-21.5±0.2	HD 219134
2	1	50	-23.7±0.3	GL 820a
2	2	50	-23.8±0.4	GL 820a
3	1	50	-23.4±0.4	GL 820a
3	2	50	-23.2±0.5	GL 820a
2	1	50	-22.7±0.3	HD 219134
2	2	50	-22.8±0.4	HD 219134
3	1	50	-22.3±0.3	HD 219134
3	2	50	-22.1±0.5	HD 219134

[a]Order 40: 5600-5700Å; Order 50: 4480-4570Å

3.5 Conclusions

EM Cygni, a long-period dwarf nova of the Z Cam subtype, has long been somewhat enigmatic. All the measured radial-velocity curve amplitudes indicated that the mass donor in the binary system was more massive than the white dwarf primary. This situation should be unstable, and therefore EM Cyg should not exist. This chapter has presented time-resolved spectroscopy of EM Cyg which indicates that this is not the case. EM Cyg is actually transferring mass in a stable manner, and the low radial-velocity amplitude measured previously was due to the presence of a third spectrum whose absorption lines were influencing the position of the cross-correlation peaks. This was causing the measured radial velocity values to be pulled closer to the zero point, and so the resulting amplitude value was too small. Several indicators pointed to this third star being physically associated with the CV; the similar γ–velocities, and the similarity between the measured spectral types of the two cool stars. So further observations were obtained to deduce conclusively whether

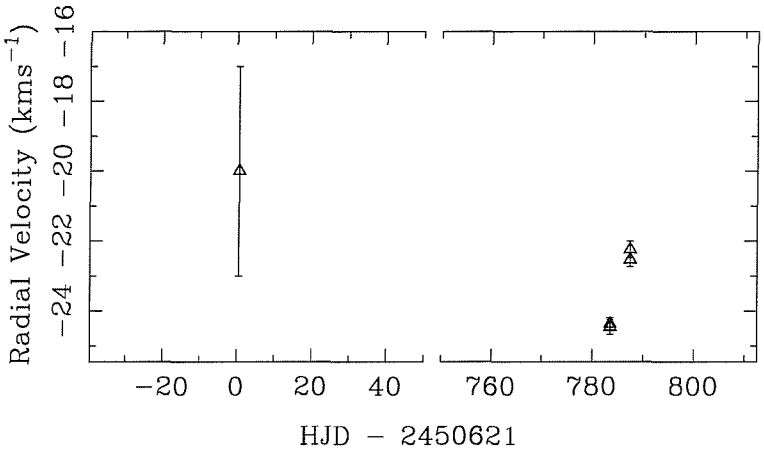

Figure 3.18: The radial velocities measured for the third star from four epochs of spectroscopy

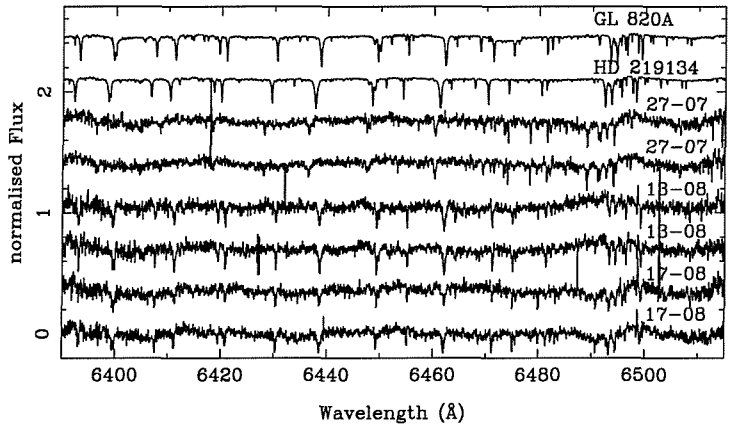

Figure 3.19: The spectra from Echelle order number 35, showing clearly the third star absorption lines

the apparent physical association was real. Unfortunately, the data so far are not yet revealing the answer to this question. More high-resolution radial velocity data need to be obtained.

Chapter 4

The quest for accurate systemic velocities of dwarf novae

Summary

The determination of the centre-of-mass velocity of a binary system (γ, the *systemic velocity*) has important implications for the evolutionary theories constructed to describe these objects. Standard CV evolutionary theory uses disrupted magnetic braking to explain the existence of the period gap (Spruit and Ritter, 1983; Rappaport et al., 1983). As a result of this hypothesis, CVs above the period gap are expected to be younger than those below the gap; magnetic braking is an efficient process for the removal of angular-momentum so if it ceases then gravitational radiation is left as the mechanism losing orbital angular momentum, and this operates over a much longer time scale. Kolb & Stehle (1996) used population synthesis methods to confirm that the longer period dwarf novae should be younger than those below the period gap (section 1.6), as a result of assuming disrupted magnetic braking occurs. Applying the empirical age-velocity dispersion relation found for single stars (Wielen et al., 1992; Wielen, 1977), Kolb & Stehle (1996)

found the theoretically expected distribution of γ–velocities and the dispersion of γ with orbital period. This distribution predicted that objects above the gap would have a smaller line-of-sight velocity dispersion than those below it. In addition, the models of Kolb & Stehle (1996) showed that brightness-dependent selection effects (which plague observational studies of CVs) actually preserved the age difference, and so determining accurate γ–velocities for CVs would provide a direct test of the disrupted magnetic braking model of CV evolution. An observational project was started to ascertain whether proposed methods could lead to accurate measurements of γ–velocities. γ–velocities have been accurately measured for four systems (with $P_{orb} > 6$ hours): SS Cygni, AH Herculis, EM Cygni and V426 Ophiuchi (hereafter SS Cyg, AH Her, EM Cyg & V426 Oph respectively). Initial results show a spread in the γ–velocities of the four systems of only $17 \pm 2\,\mathrm{km\,s^{-1}}$, and a velocity dispersion of only $\sim 8\ \mathrm{km\,s^{-1}}$. The predicted dispersion is $15\,\mathrm{km\,s^{-1}}$ (Kolb and Stehle, 1996). In this chapter the techniques used to obtain these velocities are discussed, along with the implications of this result for evolutionary theory of CVs.

4.1 Systemic velocities and their importance

The centre-of-mass velocity of a binary system (γ) is an important parameter when considering its evolution. The age of an object can often be reflected in its space motion. The older the object, the higher its random velocities are. This space velocity is likely to have been provided by encounters with giant molecular clouds, or other massive objects resulting in a 'kick' to the stellar velocity. Kolb & Stehle (1996) proposed that a way to probe the age distribution of the CV population would be to examine the dispersion of observed γ–velocities of population I Galactic CVs. This suggestion, which is independent of the selection effects which plague comparisons between theory and observations in the CV regime, provides a direct test for the magnetic braking model of CV evolution. Magnetic braking is assumed only to operate when the mass donors in the binary stars have radiative cores. This

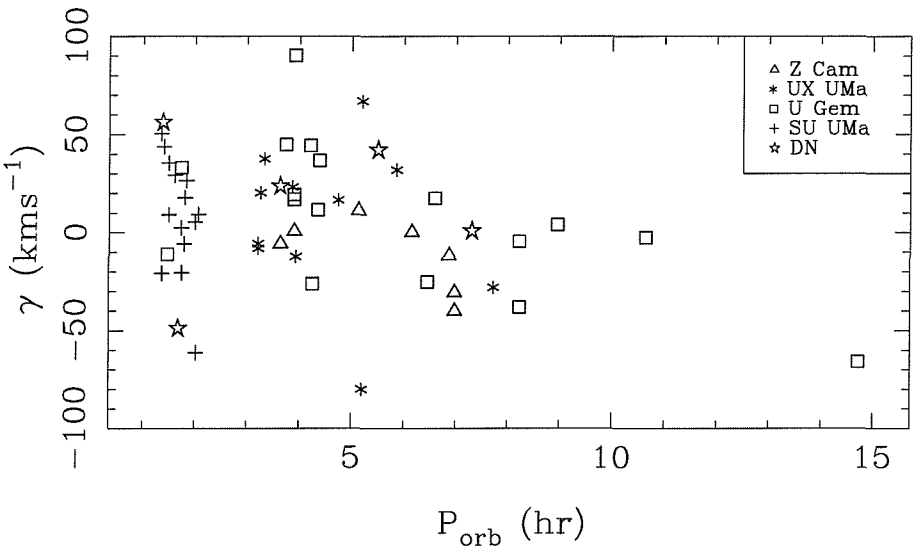

Figure 4.1: The distribution of γ velocities plotted against the orbital period of the system. Data from Kolb & Stehle (1996)

places a lower limit on the secondary mass of $M_2 > 0.2 - 0.3\,M_\odot$. So, those CVs with fully convective mass donors will be experiencing a period of cessation of the magnetic braking mechanism and therefore losing angular momentum at a lower rate. Kolb & Stehle (1996) determined the age structure of a model population of Galactic CVs, and by convolving this with the observed age-space velocity relation of Wielen (1992) they obtained the theoretical distribution of γ-velocities. They showed that the age of a system in the present CV population is largely determined by the time scales of the orbital angular-momentum loss mechanisms (magnetic braking and gravitational radiation). The present explanation for the existence of the so-called 'period-gap' in the CV period distribution involves the concept of disrupted magnetic braking for those systems with a fully convective mass donor. This immediately introduces an age split into the CV population; those systems above the period gap must be younger than those below it. Kolb & Stehle (1996) used population synthesis methods to confirm this explanation. In addition, their models showed that the brightness-dependent selection effects which have hitherto plagued comparisons between observation and theory preserved the age differences, thereby providing an opportunity to directly test the magnetic braking model. So, if current models are correct, then the CV group having periods longer than the upper limit

of the period gap ($P_{\rm orb} \geq 3$ hours) should be younger ($\leq$ 1.5Ga), and therefore only have a small line-of-sight velocity dispersion, due to having experienced fewer gravitational interactions. Conversely, those CVs with orbital periods shorter than the lower limit of the period gap, should be older ($\geq$ 3-4Ga) and show a larger velocity dispersion.

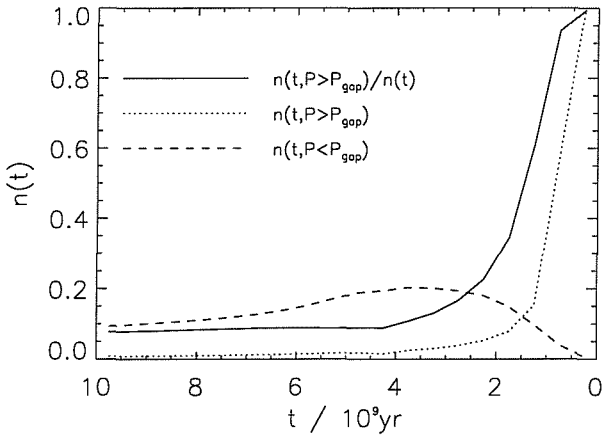

Figure 4.2: This figure (from Kolb & Stehle, 1996) shows the relative number of systems as a function of age, for CVs above the period gap ($P_{\rm orb} > 3$hr, dotted line) and below the gap ($P_{\rm orb} < 2$ hr, dashed line). The solid line is the total fraction of CVs above the period gap as a function of age. The relative youth of the longer period systems is a firm prediction of the magnetic braking model of CV evolution.

In a review by van Paradijs, Augusteijn & Stehle (1996), the observed γ velocities for a sample of CVs were collected together from published radial-velocity studies and statistically analysed. They concluded that for the non-magnetic CVs (of which they had a sample size of 72), the rms scatter of the velocity distribution is 33.4 km s^{-1}. Assuming that the measurement error and the intrinsic dispersion add in quadrature, they calculated that the γ–velocities must have an intrinsic dispersion of 27 km s^{-1}, the measurement error having been deduced as 19.7 km s^{-1} (the rms scatter of a single γ measurement). The problems associated with using values taken from the literature are, unfortunately, not negligible. Typically, with the emission lines a γ-value which is only one tenth the size of the radial-velocity variations in the system, and only one hundredth of the total spectral line width is

being measured. Many radial-velocity curves of both white dwarfs and mass donors in CVs have been attempted. However, if just a measurement of the radial velocity amplitude is required, then care will not have been taken to ensure that systematic effects do not dominate. To obtain an accurate value for the γ-velocity requires a little more care. For example, it is vital that the spectra are adequately sampled, and that a reasonable number of radial-velocity standard stars have been observed. If a lower spectral resolution is used to obtain data, then the probability of the spectral lines being affected by blending is significantly increased, so using a dispersion which minimises this effect is important. Measuring radial velocities from the absorption lines due to the mass donor goes part way to reducing possible sources of error. These absorption lines are not visible in all dwarf novae. They are generally only present in those systems with orbital periods above the so-called 'period gap' (where there is a dearth of non-magnetic systems due to the cessation of the magnetic braking mechanism – to enable loss of angular momentum; see section 1.6). Where two sets of spectral lines are present, radial velocity analyses can be carried out on both the absorption lines and the emission lines, thus enabling a calculation of the mass ratio, q, of the binary star to be made. Alternatively, a value for q can be deduced using the rotational broadening from and the radial velocity amplitude of the mass donor absorption lines. Radial-velocity curves obtained from the absorption lines are inherently less prone to systematic error; those from the emission lines (to measure the motion of the white dwarf) are affected by the contribution from the accretion disc. The systemic velocity (hereafter γ–velocity) is a measure of the centre-of-mass radial velocity of the binary, and can be deduced directly from the radial-velocity curves. Unfortunately, obtaining accurate measurements of the centre-of-mass radial-velocities of CVs has always been problematic. The radial velocities obtained from emission lines are well known to be affected by the internal motions in the disc or stream which contribute larger velocities than γ . Therefore, the measurements of γ obtained from the emission lines may not accurately reflect the motion of the white dwarf at all. This will be especially true if the inner disc is distorted in some way. For example, in magnetic CVs, where the magnetic field

of the primary is so strong it disrupts the accretion disc, and prevents it forming near to the surface of the white dwarf. However, I believe that these are not major problems for determining the γ-velocities of dwarf novae, it is just that they have not been the primary concern in previously published radial-velocity studies. Here, the initial results of a project to deduce reliable γ-velocities of a large sample of longer-period ($P_{\rm orb} \geq 6$ hours) non-magnetic CVs are presented. The aim of this initial investigation was to test the methods and procedures described in section 4.3, to see whether they could produce sufficiently accurate γ-velocity values, capable of being used to construct an observed velocity-dispersion relation for Galactic CVs, and thus be able to compare the results directly with the theory.

4.2 Radial velocity standard stars

Observations of late-K and early-M spectral-type radial-velocity standards were made using the lists of Marcy, Lindsay & Wilson (1987), Barnes, Moffett & Slovak (1986), Beavers & Eitter (1986), Beavers et al. (1979), Duquennoy et al (1991) and Eggen (1992) for reference. The full list of 25 standards which were actually observed is given in Table 4.1. The requirements for choosing the radial velocity standards were that they were between RA10 – 24 and 00 – 02, with declinations greater than $-20°$, having good radial velocity measurements. The references quoted cite the number of spectra, N (column 3, Table 4.1) used to obtain the radial velocity measurement, and they also quote the standard deviation of the set of measurements, σ (column 4, Table 4.1). The standards were chosen primarily so that $\sigma < 1.5\,{\rm km\,s^{-1}}$ based on at least five spectra. Since the spectral types of the mass donors in the CVs to be observed were not tightly constrained, the selection of radial velocity standards had to include a good range of spectral types: types from G8V to M5V were used. So, having a good spectral type was a further requirement for choosing the standards, although obviously it was not as important as the objects having good radial velocity measurements. Figure 4.3 shows the earlier

Table 4.1: The radial velocity standard stars which were observed

Object name	RV ($km\,s^{-1}$)	N	σ	Spectral type	Reference[a]
HD 4628	-9.73	6	0.15	K2V	1
GL 380	-25.29	20	0.28	M0	1
GL 411	-84.74	19	0.16	M2V	1
GL 569	-7.17	12	0.28	M3V	1
GL 752	+35.82	14	0.18	M3.5V	1
GL 720	-31.12	10	0.12	M2	1
GL 436	+9.65	10	0.13	M3	1[b]
GL 699	-110.86	22	0.24	M5V	1
GL 806	-24.03	6	0.41	M1.5V	1
GL 820A	-64.97	19	0.22	K5V	1
GL 820B	-63.89	6	0.13	K7V	1
HD 101177	-16.6	19	1.8	K3V	2

continued.....

[a]1 - Marcy et al. (1987); 2 - Beavers & Eitter (1986)

[b]Eggen (1996) indicates -9.5 $km\,s^{-1}$

spectral-type standards, from G8V to K7V, offset by an arbitrary amount in order to see the variations which occur with decreasing temperature. The standards were all normalised by their continua, which were then subtracted before plotting. The general shape of the continuum around 6360–6380Å changes markedly from type G8 to type K7. Additionally, the relative strengths of the lines at 6400Å and 6440Å are a good indicator of spectral type in this wavelength region. Figure 4.4 is a similar plot, but this time showing the later spectral type standards. The M-dwarfs plotted here clearly illustrate the developing continuum shape around 6360Å. The relative depths of the lines at 6400Å and 6440Å are still changing with the progression to lower temperatures, and are used later on to aid spectral typing of the mass donors in the CVs observed (sections 3.2.1, 4.4.2). Figure 4.5 shows the measured γ–velocities obtained using the twenty-six radial-velocity standards. They are consistent from one standard to another on the whole, although a few of the standards appear to give discrepant results. Reasons for these measurements are given in the following paragraphs.

Table 4.1: *Continued.....*

Object name	RV ($km\,s^{-1}$)	N	σ	Spectral type	Reference
HD 122742	-8.2	20	1.7	G8V	2
HD 131156	+1.9	20	1.1	G8V	2
HD 139341	-67.7	6	1.5	K2V	2
HD 165341	-9.7	24	0.2	K0V	2
HD 219134	-18.2	31	2.3	K3V	2
HR 7345	3.0	20	0.3	G8V	3
HD 182488	-20.7	20	0.4	K0V	3
HR 7462	28.3	27	0.3	K0V	3
HR 0166	-33.2/-32.8	20/10	0.3/0.8	K0V	3/4
HR 0493	-33.8	21	0.4	K0V	3
HR 0753	26.1	19	0.4	K3V	3
HR 4496	-5.0/-5.1	16/16	0.3/0.5	G8V	3/4
HR 5706	-46.8	16	0.4	K0	3
HR 7345	3.0/4.4	20/6	0.3/1.2	G8V	3/4

2 - Beavers & Eitter (1986); 3 - Beavers et al. (1979); 4 - Barnes, Moffatt & Slovak (1986);

GL 436 The radial velocity value used for GL 436 was that from Marcy et al. (1987) ($9.65\,km\,s^{-1}$). In Fig. 4.5, the systemic velocities calculated using this standard appear have a much larger range than those from the other radial-velocity standards (numbers 12 and 13 on the x-axis). At this point it was noticed that in Eggen (1992), the radial velocity of GL 436 is quoted as -9.5 $km\,s^{-1}$. It is not clear which reference contains the error, although SIMBAD quotes the radial velocity to be $+10\,km\,s^{-1}$. In any case, any further analysis discounts results from this standard for this reason.

HR 0166 In the observing logs (and therefore the spectrum headers), the object name for this particular standard is given as HR 0166. However, a look at the coordinates revealed that the object observed wasn't HR 0166, but was actually GL 820A. All the cross-correlations carried out with this standard were therefore done assuming an incorrect value for its radial velocity (template number 25 in Fig. 4.5). All the resulting γ–velocities using this template were approximately $30\,km\,s^{-1}$ too large ($-33.2\,km\,s^{-1}$ had been used instead of $-64.97\,km\,s^{-1}$ as the radial velocity of the

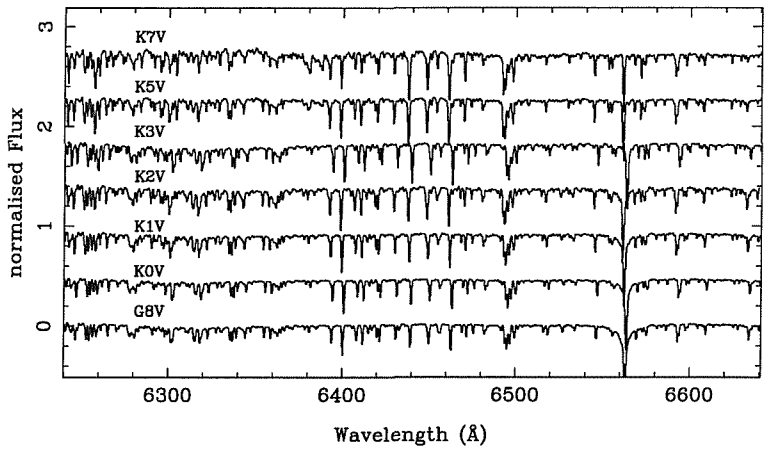

Figure 4.3: Spectra of the K-dwarf radial velocity standard stars in the wavelength range observed over

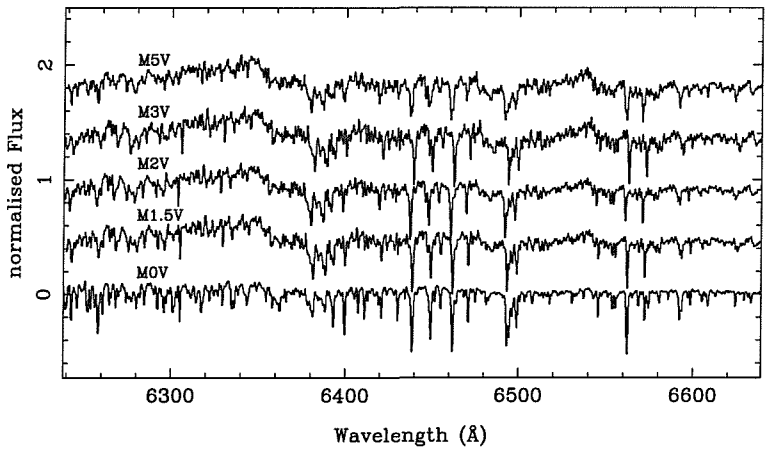

Figure 4.4: Spectra of the M-dwarf radial velocity standard stars in the wavelength range observed over

standard). Once this problem had been identified, the values were corrected for this problem, the γ–velocities in Fig. 4.5 move down by $\sim 30\,\mathrm{km\,s^{-1}}$ to their present positions and all the discrepant points in Fig. 4.10 disappear.

GL 699 This star, Barnard's Star, has the largest proper motion as seen from Earth. It is also the M-dwarf observed with the latest spectral type. The radial-velocity standard numbered 'template 24' on Fig. 4.5 gives the γ–velocity measurements made with this star. The spread of measurements is much wider than for most of the other standards. This may possibly be a result of its discordant spectral type compared to those of the mass donors in the CVs observed.

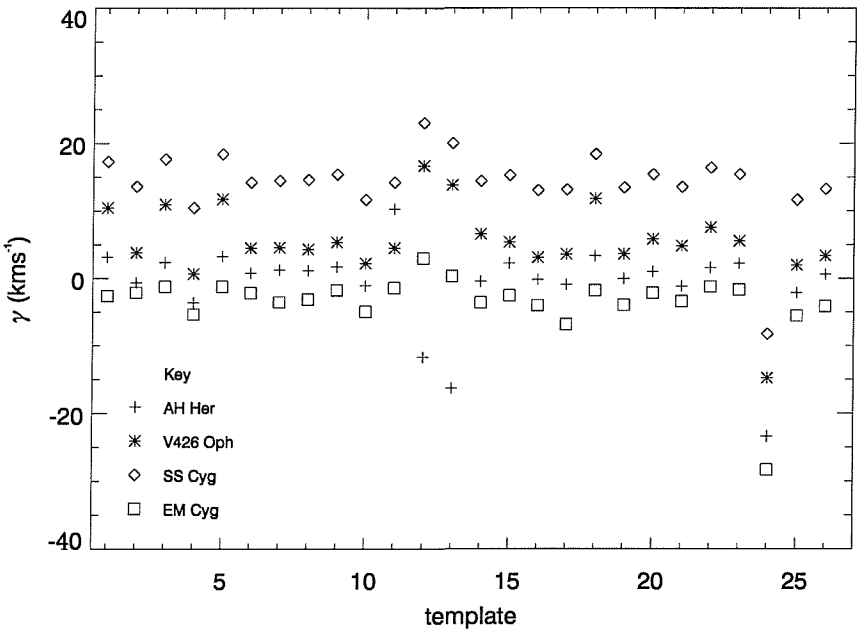

Figure 4.5: The range of γ–velocities measured using the radial velocity standards. The standard used at position 25 on the abscissa was identified erroneously in the observing log, and so the wrong radial velocity was corrected for. The standard at position 24 on the abscissa is Barnard's Star, a very high proper motion star whose spectral type is discrepant compared to those of the CV mass donors

4.3 Methods

The data for each of the dwarf novae was dealt with using the same sequence of methods. In expecting to obtain a value for the velocity dispersion of the order $15\,\mathrm{km\,s^{-1}}$, it was imperative that the γ–velocities were measured to within an accuracy of $5\,\mathrm{km\,s^{-1}}$. The following process illustrates how this was achieved, and how potential sources of systematic error (which are the main problem using a procedure like this) were minimised and, in some cases, eliminated altogether.

i. First, the continua of the individual spectra were fitted and then subtracted. The radial-velocity standard stars also had their continua fitted and subtracted.

ii. All the spectra of each DN were rebinned onto a logarithmic wavelength scale. Then each individual DN spectrum was cross-correlated with that of a radial-

velocity standard (rebinned onto an identical scale), following the method of Tonry & Davis (1979), in order to determine the heliocentric radial velocities. Adjustments were made at this stage to allow for the radial-velocity of the standard star. However, no allowance (at this stage) was made for the rotational broadening of the absorption lines from the mass donor.

iii. The radial velocities were then fitted with a circular orbit fit of the form

$$V = \gamma + K \sin \frac{2\pi(t - t_0)}{P_{\rm orb}} \tag{4.1}$$

in order to calculate the radial-velocity amplitude (K), the systemic velocity (γ), and the phase-zero point (where phase zero (ϕ_0) is defined as the phase at which the radial velocity of the mass donor crosses zero moving from negative to positive)(see section 4.4.1). These initial radial velocity fits were made to allow the orbital motion of the mass donor to be removed from the individual spectra in order to create an average spectrum from which to determine its spectral type.

iv. Then the cross-correlation and curve-fitting process was repeated with the radial-velocity standards artificially broadened to match the widths of the absorption lines seen in the DN. Measurements of the rotational broadening of the absorption lines are calculated in section 4.4.3. Determination of the broadening also allowed an estimate of the spectral type of the mass donor to be deduced.

v. Initially, an estimate of the spectral type of the mass donor could be deduced simply by inspection of the spectra. The behaviour of several of the absorption lines is obviously closely related to temperature in the standard stars observed. Casares, Charles, Naylor & Pavlenko (1993) noted the usefulness of several relative line depths in constraining the spectral type of the mass donor in V404 Cyg, over a similar wavelength region to the one being used here (see section 4.4.2). The spectral-type of the mass donor in the dwarf

nova could also be deduced in the following way. A range of standard stars with different spectral types were artificially broadened, and then fractions of those standard spectra were subtracted from the average DN spectrum (with the orbital motion of the mass donor removed). The fraction of a particular standard which produced the lowest χ^2 value determined the best-fit spectral type. The mass donor spectral types are discussed in section 4.4.2.

vi. Finally, the cross-correlations were repeated again, using the radial-velocity standard (of best-fit spectral-type) broadened to the measured rotational velocity of the mass donor.

To avoid introducing errors due to spectral-type mismatch between standard star and dwarf nova, steps (i) to (v) were repeated with velocity standards of several different spectral types (ranging from G8V–M6V). The radial velocities obtained for each dwarf nova did not differ significantly, implying that spectral-type mismatch between standard and dwarf nova is not a significant source of systematic error here. This process also identified those radial-velocity standards which are good to use for this purpose, and those which may still have an uncertain radial velocity value, or spectral type. Observing such a large number of standards at the first attempt (over 20) will aid the efficiency of future observing runs, since a smaller number of reliable radial-velocity standards can be observed, thus maximising the available exposure time for observations of dwarf novae.

4.4 Results

In this section, the results obtained using the methods described in section 4.3 are presented. Section 4.4.1 describes the radial velocities obtained for each mass donor. This is followed by the results of the rotational broadening measurements

(section 4.4.3), and the mass-donor spectral typing process (section 4.4.2). Finally, the resulting systemic velocities are given in section 4.4.4.

4.4.1 Radial velocity curves for the mass donors

To obtain sufficiently accurate radial velocities, the absorption spectrum from the mass donor, which can be seen in the wavelength region $\lambda\lambda\, 6350 - 6540$ was used. DN with orbital periods greater than $\approx$ 5 hours have mass donors with spectral types in the early-to-mid K range. Due to the higher temperatures of these stars they can manifest themselves in the DN spectrum at shorter wavelengths than their M-dwarf mass donor counterparts, which tend to get quenched by the dominating accretion disc spectrum in the visible region. In addition, at quiescence the contribution of the accretion disc to the spectrum is smaller than when the disc is in outburst. Therefore, quiescence is the ideal time to make observations requiring measurements of the spectrum of the mass donor. The K-type secondaries generally tend to be visible in the R-band, and the M-type secondaries become more prominent in the I-band. Certainly, there is not much evidence for the mass donors of CVs in the U and B wavelength passbands.

The absorption lines from the mass donor can be easily distinguished from interstellar features, as they exhibit a sinusoidal variation, which should in theory be 180° out of phase with the one seen in the emission lines. The trailed spectra in Fig. 4.6 show the behaviour of the spectral lines over a full orbital period as observed in each system.

Figure 4.6 shows well the sinusoidal behaviour of the absorption lines. It also shows how the emission lines do vary approximately 180° out of phase with the absorption lines. The lines at $\approx$ 6300Å are interstellar, which can be deduced from their unvarying behaviour over the orbital period of the CVs. The difference between the trails of the individual systems are apparent in this plot. For example,

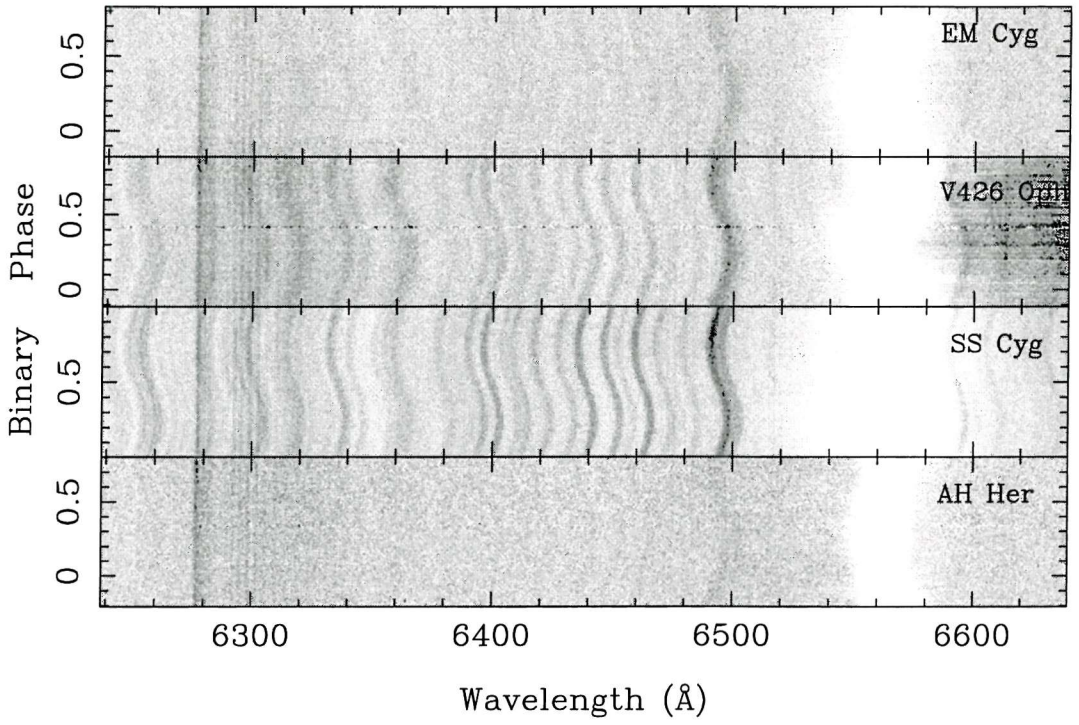

Figure 4.6: Trailed spectra (wavelength versus binary phase) of the DN observed. The Hα lines have been saturated (white) in order to bring up the contrast of the absorption lines from the mass donor, which can be seen in the wavelength range 6300 – 6500 Å. The scale used is from -0.15 to 0.15 for each object. From top-to-bottom, the panels show the systems in order of decreasing orbital period. In V426 Oph and SS Cyg, the sinusoidal nature of the absorption lines (black) is clearly visible. The lowest panel contains the trailed spectra of AH Her. The mass donor lines are not as clear as in all the other dwarf novae, but the feature at 6495Å is just visible. See Fig. 6.3 for Hα detail.

the absorption lines from the mass donor in AH Her are barely visible in the trail. However, those from the mass donor in SS Cyg are very obvious. The size and temperature of the mass donor will affect the visibility of the absorption lines, as will the relative contribution to the continuum by the accretion disc at the time of the observations. If the disc is bright (in an outbursting state) then the absorption lines from the mass donor may be quenched. Each object was observed when it was in, or approaching, a quiescent state. In addition, the strength of the absorption lines may vary around the binary orbit if the hemisphere of the mass-donor facing the white dwarf is being irradiated by the accretion disc and boundary layer. This manifests itself as a departure from a circular orbit fit to the radial velocities (see Fig. 4.7) around phase 0.5. The behaviour of the Hα line is also seen to differ markedly in each object. This will be fully discussed in Chapter 6.

The section of spectrum used for the cross-correlation was between $6350-6540$Å. This wavelength region contains absorption lines from low-ionization states of calcium and iron, which originate at the mass donor. The region containing interstellar features was avoided, as was that close to the Hα line wings. Different radial velocity curves were obtained for each of the radial-velocity standards used (ranging from spectral types G8V-M6V), to check that spectral-type mismatch did not produce a significant error. The radial velocities resulting from the cross-correlation procedure were fit with a sine curve, to determine the amplitude of the fit, K, ϕ_0, and γ–velocity. The orbital periods are already well-determined for all the observed dwarf novae, so I used the values given in the literature (see Table 4.4 for details). Then, the best-fit spectral type of the mass donor in each DN was determined (as in section 4.4.2) and following this, its rotational broadening was calculated (section 4.4.3). Finally, the radial velocities were re-calculated using the standard with best-fit spectral type, whose absorption lines had been artificially broadened to the best-fit value of $v \sin i$. Figure 4.7 shows the sinusoidal fits to the radial velocities of

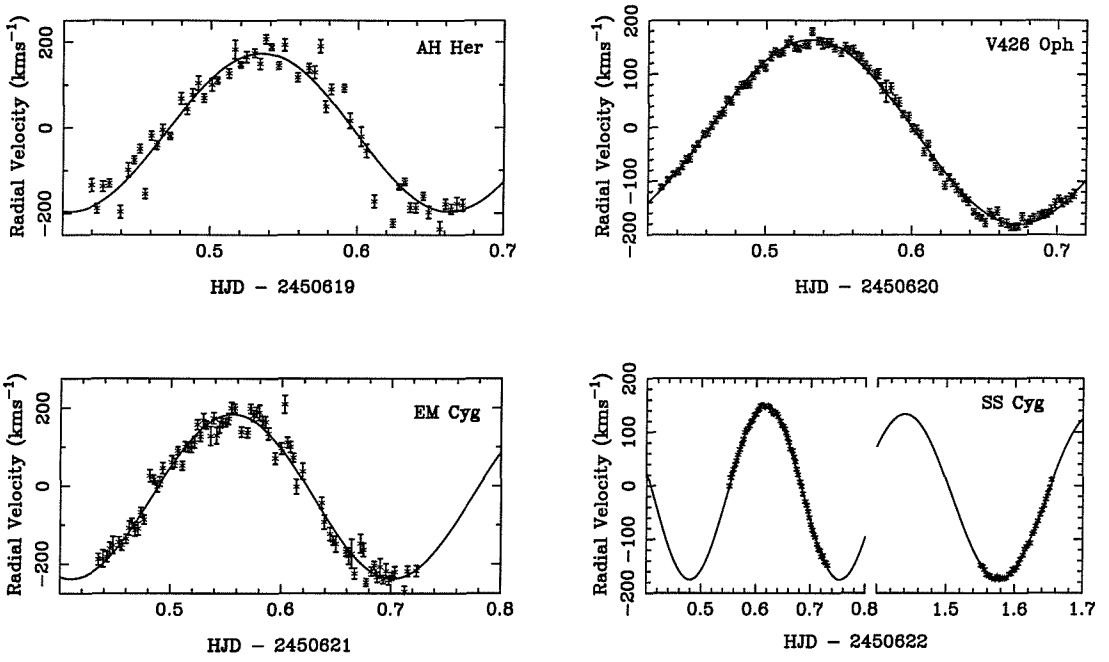

Figure 4.7: Sinusoidal fits to the radial velocity data for each dwarf nova. Clockwise from top left, AH Her, V426 Oph, EM Cyg and SS Cyg. The data from two nights worth of observations for SS Cyg is combined into the lower right-hand plot.

each DN. The radial-velocity standard used to obtain each fit was of best-fit spectral type and artificially broadened to the value obtained in section 4.4.3. It was then cross-correlated with the individual DN spectra as described previously.

4.4.2 Determination of the spectral type of the mass donors

An estimate of the spectral type of the mass donor in each dwarf nova was carried out. This was done using the following method. It must be noted that quite a reliable spectral type value was obtained simply by inspection of the spectra in the wavelength region 6350 − 6540Å. The depth of the Fe I blend at $\lambda\lambda 6400.0 + 6400.3$, compared to that of the Ca I line at $\lambda\lambda 6439.1$ varies with effective temperature over the spectral-type range in use (G8V-M6V). Casares et al. (1993) also noted some useful spectral-typing line relationships in a similar wavelength region. In particular, they note that the relative depths between Ca I $\lambda 6439.1$ and the blends Ca I $\lambda 6462.6$ + Fe I $\lambda 6462.7$ are particularly useful. They also measured the EW of

Table 4.2: The mass donor spectral type determined for each object. Previous estimates of the spectral type (gathered from the literature) are also given.

Object	Spectral Type of mass donor	Previous Spectral type	reference for previous spectral type[a]
EM Cyg	K3	K5V	1
V426 Oph	K5V	K3V	2
SS Cyg	K5V	K2-K3V	3
AH Her	K7V	K0-K5V	4

[a] 1) Stover et al., 1981; 2) Hessman, 1988; 3) Martinez-Pais et al., 1994; 4) Horne, Wade & Szkody, 1986.

these lines, plus those of Fe I $\lambda\lambda$6430.9, Fe I $\lambda\lambda$6392.5 + 6393.6 and Fe I $\lambda\lambda$6400.0 + 6400.3, and remarked that the ratios $\lambda\lambda$6439/6431, and the $\lambda\lambda$6450/6439 are very sensitive to $T_{\rm eff}$ over the spectral-type range in question.

The standard spectra were each artificially broadened to an appropriate value (determined in section 4.4.3). Then the fraction of that broadened standard which, when subtracted from the dwarf nova spectrum, best removed the spectral lines of the mass donor was calculated. The routine used minimised the χ^2 between the DN spectrum (with a specific fraction of the chosen standard subtracted) and a smoothed version of itself. The standard producing the lowest value of χ^2 gave an indication of the spectral type of the mass donor. All the objects observed have mass donors with a spectral type later than K3. AH Her best fitted a K7V mass donor. SS Cyg and V426 Oph were both best-fit using a K5V type. Finally, EM Cyg resulted in a K3 – 5 type mass donor, see Chapter 3 and North et al. (2000). Figure 4.8 shows the average spectra of the four dwarf novae, created by removing the orbital motion of the mass donor from each individual spectrum, rebinning onto a uniform velocity scale, and co-adding the results. The absorption lines are obviously broadened; measured in each case to be $\approx 100\,{\rm km\,s^{-1}}$ (see Table 4.3). Marked on the plot are a few of the spectral lines found most useful in the spectral typing process. The blend at λ6495 is also marked on the plot. This was not used in the spectral typing

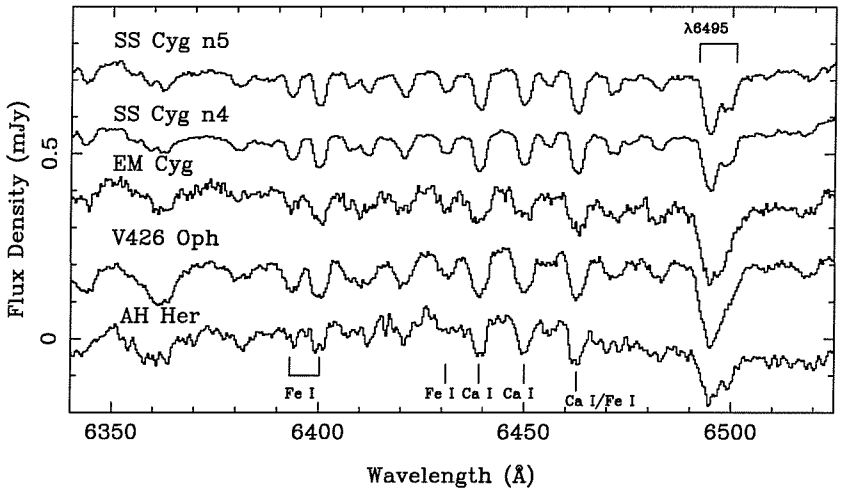

Figure 4.8: The average spectra of the mass donors of the four dwarf novae observed over the five night observing run. The raw spectra for each DN have had the orbital motion of the mass donor removed, then been rebinned onto a uniform velocity scale and then averaged.

process as it is a blend of mostly Ca I λ6493.8 and Fe I $\lambda\lambda$6495.0, 6495.7 and λ6496.5. However, it is the one absorption feature originating from the mass donor which is clearly visible in the trailed spectrum of each dwarf nova. Purely by inspection, there appear to be four reliable indicators of spectral type at this wavelength range. Firstly, there appears to be a relationship between the relative depths of λ6439.1 and the blend at $\approx$ λ6400 which changes rapidly over the spectral type range we are interested in here (as mentioned earlier). This enables us to identify whether the spectral type is between G8 and K3, or between K5 and M6. Secondly, the Fe I lines around λ6400 begin to change very obviously around spectral type K7. This can give a further constraint on the identification of the mass donor. In addition, the general shape of the spectrum around 6370Å allows us to deduce whether the mass donor is a K- or M-type star. Finally, the two spectral features just short of the λ6495 blend vary significantly relative to each other over the spectral range G8–M6. These factors were all taken into account when initially spectral-typing the mass donor in each dwarf nova.

4.4.3 Calculation of the projected rotational velocity of the mass donors

The rotational broadening of the absorption lines was determined using a standard having the same spectral type as that estimated for the mass donor. The standard was then artificially broadened to values between 0 and 200 $\mathrm{km\,s^{-1}}$ (using increments of $10\,\mathrm{km\,s^{-1}}$). The orbital motion of the mass donor of the dwarf nova was removed from the individual spectra, and the results rebinned onto a uniform velocity scale. The resulting spectra were then co-added. The fraction of the standard which best removed the mass donor lines was then calculated, using an optimisation technique. The fraction required was calculated by minimising the scatter between the spectrum of the standard and the dwarf nova spectrum. This gave a value for the rotational broadening of the mass donor, and an additional estimate of its spectral type. Plotting χ^2 versus the amount of artificial broadening used on the standard produces a minimum in χ^2 at the optimum value of $v \sin i$ (see Fig. 4.9 for examples). In order to check that choosing one spectral type for the mass donor did not introduce a further source of systematic error, we repeated the $v \sin i$ measuring technique with all the available standard stars. The standard error on the mean of the sample was $2\,\mathrm{km\,s^{-1}}$, implying that the choice of standard used to calculate $v \sin i$ was not significant. A value of 0.5 was used for the limb-darkening coefficient for each dwarf nova. Changing this value did not change the deduced values of $v \sin i$ by more than $5\,\mathrm{km\,s^{-1}}$, see Chapter 3 for details of the method followed. Table 4.3 shows the measurements of $v \sin i$ for each of the observed systems. Horne, Wade & Szkody (1986a) calculated a value for the rotational broadening of the mass donor in AH Her of $112\pm17\,\mathrm{km\,s^{-1}}$. Our value of $103\pm2\,\mathrm{km\,s^{-1}}$ agrees with theirs. Hessman (1988) determines a value for the mass donor of SS Cyg of $87\pm4\,\mathrm{km\,s^{-1}}$. Our value of $96\pm3\,\mathrm{km\,s^{-1}}$ agrees at the 2σ level.

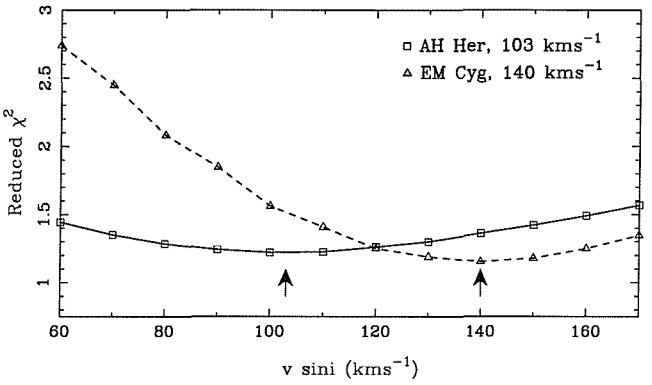

Figure 4.9: Examples of the χ^2 vs. $v \sin i$ curves obtained during the rotational broadening measurement procedure. The arrows denote the positions of the minima of the curves (optimum $v \sin i$ value).

Table 4.3: The rotational broadening values determined for the mass donors in the four dwarf novae.

Object	$v \sin i$ ($\mathrm{km\,s^{-1}}$)	Spectral type of standard used	mass ratio deduced from $v \sin i$ and K_2
EM Cyg	140 ± 2	K3V	0.88 ± 0.03
V426 Oph	132 ± 3	K5V	0.96 ± 0.01
SS Cyg	96 ± 3	K5V	0.68 ± 0.02
AH Her	103 ± 2	K7V	0.69 ± 0.02

4.4.4 Deducing the γ–velocities

Many previously attempted radial-velocity studies have published values for the γ–velocities of several dwarf novae, both in outburst and quiescence. Several of these results are significantly different, and do not appear consistent with each other. I believe that this is just a symptom of the data acquisition methods. Obtaining γ–velocities is not the primary concern for many of these studies, and so it is possible that the spectra are undersampled, for example and therefore unsuitable for deducing γ–velocity values. In section 4.6 a compilation of the published γ–velocity measurements for the dwarf novae discussed in this paper is presented. SS Cyg is a prime example of a single object with many differing values for the γ–velocity. Echevarria et al. (1989) obtain $-15.7 \pm 0.3\,\mathrm{km\,s^{-1}}$ for γ, from the absorption lines whilst SS Cyg was at the end of an outburst (using echelle spectra). Friend, Martin, Smith & Jones (1990a) use the Na I lines around 8190Å to calculate

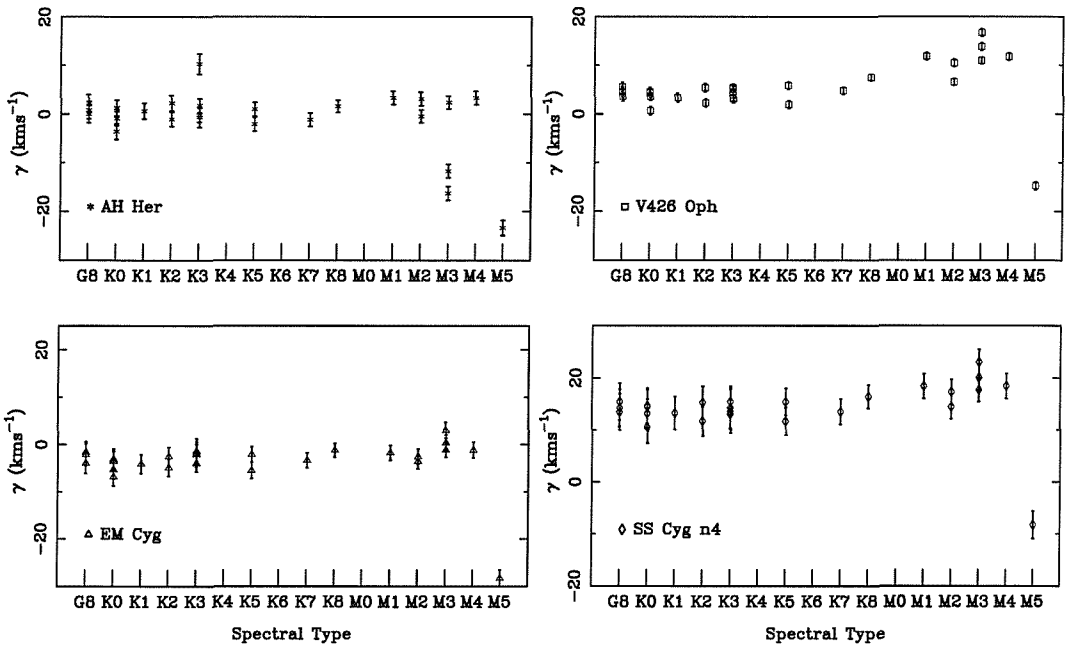

Figure 4.10: The γ–velocities calculated with each spectral type standard.

a γ–velocity of $-14 \pm 3\,\mathrm{km\,s^{-1}}$. At the time of their observations, SS Cyg was almost mid-way between two outbursts. Kiplinger (1979a), calculated a γ–velocity of $-3 \pm 4\,\mathrm{km\,s^{-1}}$, again from the absorption lines. Our heliocentric γ value for SS Cyg is $-14 \pm 2\,\mathrm{km\,s^{-1}}$. If this is the case for SS Cyg, the brightest dwarf nova for which it is easy to obtain measurements, then it can only be worse for the rest.

The line-of-sight centre-of-mass (γ) velocities are calculated at the point in the analysis described previously when the final radial-velocity curves are derived for each object. They are deduced using a sinusoidal fit to the radial velocities around the complete orbit, which have themselves been determined using a standard of the same spectral type as the mass donor, and artificially broadened to the measured $v \sin i$. The values calculated at this point are heliocentric, and in order to deduce the velocity dispersion for these measurements, it was necessary to correct for the solar motion. I have used the dynamical Local Standard of Rest (LSR) as the reference point. Corrections to apply to the heliocentric γ-velocities for AH Her, V426 Oph, EM Cyg and SS Cyg are -7.75,-16.46, -28.515 and -25.645 $\mathrm{km\,s^{-1}}$ respectively. Fig. 4.10 shows the range of γ values obtained for each spectral type

of radial-velocity standard, for each dwarf nova. It was here that using so many radial-velocity standard stars was most useful. Most of the derived values appeared to be similar in magnitude to within the error margin of $\pm 2\,\mathrm{km\,s^{-1}}$. The ones that did not agree to within this precision were found to be bad identifications in the observing log, and so the radial-velocities using that standard had been corrected to the wrong zero-point.

Values for the γ-velocities of -1.7, 5.4, 1.5 and 15.4 $\mathrm{km\,s^{-1}}$ referred to the dynamical LSR for AH Her, V426 Oph, EM Cyg and SS Cyg respectively were calculated. Considering only the data obtained here, the velocity dispersion is calculated to be $\sim 8\,\mathrm{km\,s^{-1}}$, smaller than the value of $15\,\mathrm{km\,s^{-1}}$ predicted by Kolb & Stehle, yet still consistent with it. Section 4.6 discusses this result further.

4.5 System parameters

Benefits of carrying out an accurate systemic velocity study become obvious once the data analysis is complete. Well-defined radial velocity curves for the mass donors are derived, which in turn lead to more accurate mass estimates for the white dwarfs. Accurate phasing, from the RV curves, then enables Doppler maps of the emission lines to be computed allowing further deductions about the nature of the systems to be made. Measurements of the rotational broadening of the mass donors can be made assuming that the mass donor absorption lines can be seen in the composite spectrum from the CV. These enable mass ratios for the observed objects to be calculated, thus allowing values for the mass of the main-sequence component to be calculated. This section presents these results for the four objects covered in this chapter. Table 4.4 summarises the orbital data for each system which has been used or determined in this thesis. Table 4.5 lists the derived data for the four observed dwarf novae. The mass functions, $M_1 \sin^3 i$ and $M_2 \sin^3 i$ were calculated using equations 1.15 and 1.16.

Table 4.4: System Parameters for the four observed dwarf novae

Object	Orbital Period (h)	RV amplitude[1] K_2 ($\mathrm{km\,s^{-1}}$)	Rotational broadening[1] ($\mathrm{km\,s^{-1}}$)	mass ratio[1]
EM Cyg	0.290909[2]	202 ± 3	140 ± 6	0.88 ± 0.05
V426 Oph	0.285314[3]	179 ± 2	132 ± 1	0.96 ± 0.01
SS Cyg	0.27512973[5]	165 ± 1	96 ± 3	0.68 ± 0.02
AH Her	0.258116[4]	175 ± 2	103 ± 2	0.69 ± 0.01

1 - This thesis; 2 - Stover et al. (1981); 3 - Hessman (1988);
4 - Horne, Wade & Szkody (1986); 5 - Hessman et al. (1994)

Table 4.5: Derived System Parameters

Object	inclination (°)	$M_2 \sin^3 i$ ($M_\odot$)	$M_1 \sin^3 i$ ($M_\odot$)	M_2 ($M_\odot$)	M_1 ($M_\odot$)
EM Cyg	67 ± 2[1]	0.77 ± 0.08	0.88 ± 0.05	0.99 ± 0.12	1.12 ± 0.08
V426 Oph	59 ± 6[2]	0.62 ± 0.02	0.65 ± 0.02	0.70 ± 0.13	0.73 ± 0.14
SS Cyg	37 ± 5[2]	0.25 ± 0.01	0.36 ± 0.01	0.92 ± 0.31	1.36 ± 0.45
AH Her	46 ± 3[2]	0.28 ± 0.01	0.41 ± 0.01	0.61 ± 0.10	0.83 ± 0.13

[1] this thesis; [2] Ritter & Kolb (1998);

V426 Oph is the only object for which the mass ratio determined from the rotational broadening measurement is very different compared to that determined previously. This may be an effect of irradiation of the mass donor, which would cause the absorption lines from the mass donor to appear more broad than they would be without the irradiating source present. This would lead to an overestimate of $v \sin i$ which itself would lead to an overestimate of q. Hessman (1988) quotes $q = 0.78 \pm 0.06$, calculated using the radial-velocity amplitudes from the emission and absorption lines ($K_1 = 142 \pm 11\,\mathrm{km\,s^{-1}}, K_2 = 183 \pm 3\,\mathrm{km\,s^{-1}}$). For a value of this magnitude to result from the $v \sin i$ method, the rotational broadening of the absorption lines for V426 Oph would need to be $\sim 15 - 20\,\mathrm{km\,s^{-1}}$ smaller than measured here. The value calculated using Eggleton's formula, equation (1.8), and the $v \sin i$ and K_2 values given in Table 4.4 lead to a value of 0.96 ± 0.01, which is significantly larger than that used by Hessman (1988).

4.6 Discussion

In order to detect a velocity dispersion with a magnitude of $\approx 15\,\mathrm{km\,s^{-1}}$ it is important to aim to obtain measurements of γ to within $\approx 5\,\mathrm{km\,s^{-1}}$. Using the methods detailed here, and knowing precisely the data-acquisition requirements needed during the observing run itself, a process has been formulated which specifically targets accurate measurements of γ–velocities. The requirement for optimum sampling of the spectra (to measure accurate γ–velocities) reduces the potential use of archived data to carry out statistical analyses. The methods presented in this paper for measuring γ-velocities have been thoroughly tested here on four long-period dwarf novae, and the initial results indicate that the techniques are an accurate way to determine γ–velocities for CVs, whilst minimising the potential sources of systematic error which exist.

The velocity dispersion (σ_v) is defined as the root mean square of the peculiar stellar space velocity, v (Kolb and Stehle, 1996). Using a local Galactic coordinate system (U, V, W), where U points towards the Galactic centre, V is in the direction of the Galactic rotation, and W is in the direction of the North Galactic pole, Wielen et al. (1992) (introduced by Wielen (1977)) define the total dispersion, σ_{v} as

$$\sigma_{\mathrm{v}}^2 = \sigma_V^2 + \sigma_U^2 + \sigma_W^2 \tag{4.2}$$

obeys this age–velocity relation:

$$\sigma_{\mathrm{v}} \simeq 10 + 21.5\left(\frac{t}{(10^9 yr)}\right)^{1/2}\ \mathrm{km\,s^{-1}} \tag{4.3}$$

This relation is also expected to hold for binary systems, unless an event occurs during its evolution in which a significant fraction of the total mass of the system is violently, asymmetrically ejected. In the case of CVs, the progenitors do eject a fraction of their mass during the common-envelope period, but this occurs on a time scale much longer than the duration of the orbital period, and so can be considered

as symmetric about the rotation axis of the binary. This means that the space velocity of the system is not affected. Kolb & Stehle (1996) note that repeated nova eruptions would alter the space velocity of the system. This would *increase* the velocity dispersion of CVs. For this case, equation (4.3) would underestimate the total dispersion.

The velocity observed for the CV population which describes their space motion is the velocity of the centre-of-mass of the binary star. Assuming CVs are isotropically distributed about the Galaxy, the γ–velocity dispersion is related to σ_v by

$$\sigma^2_{|v|} = < \gamma^2 > = \frac{1}{3}\sigma^2_v \tag{4.4}$$

In transforming the CV population from a distribution in age, t and orbital period, P_{orb} to one over γ–velocity and orbital period (P_{orb}) a distribution is obtained from which can be derived the root-mean-square (σ_γ) of the range of γ–velocities at a specific orbital period. It is seen that the CVs above the period gap (young) show a significantly smaller dispersion in γ. What is notable about the $\sigma_\gamma(P_{orb})$ distribution is that it is essentially independent of the selection effects which plague the original distribution, $n(\gamma, P_{orb})$. The observations taken here are the prelude to obtaining a full, statistically meaningful sample of γ–velocity measurements, for objects both above and, eventually, below the period gap in the distribution of CVs. Initial results from the first sample of systems indicate that the behaviour of the longer-period dwarf novae does follow closely that predicted from the theory (as presented by Kolb & Stehle, 1996). Fig. 4.11 compares the distribution of γ–velocities as obtained a) in this paper (solid marking) and b) from the literature (hatched lines) for the four dwarf novae observed in this pilot study. It can be seen that the distribution of literature values has a large range. It is obvious why therefore, Kolb & Stehle suggested obtaining a complete set of velocities for both groups of CVs (above and below period gap). In doing this a direct test of the disrupted magnetic braking theory is being undertaken, one of the basic assumptions in the standard model of CVs.

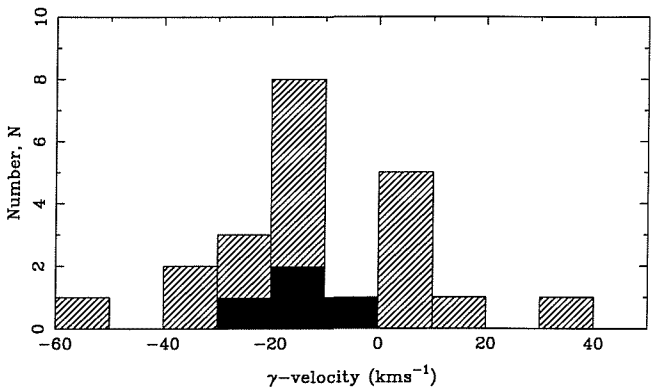

Figure 4.11: A histogram showing the spread of values for the γ–velocities of the dwarf novae observed. The solid histogram is the results we have so far, and the area with hatched lines denotes values for each of the observed systems gathered from the literature.

Using the random sample of γ–velocities measured here, the velocity dispersion is deduced by calculating the variance of the sample (S^2). The sample variance is described by

$$S^2 = \frac{\Sigma_{i=1}^{N} \left(X_i - \bar{X}\right)^2}{N-1} \tag{4.5}$$

For a small random sample (X, S^2) from a population (μ, σ^2), the quantity NS^2/σ^2 can be described by a chi-square distribution with $N-1$ degrees of freedom. Using this theorem on the data in question implies that a confidence interval on the determined velocity dispersion can be calculated. The relation which must be obeyed to calculate a 95 per cent confidence limit is

$$P\left(\chi^2_{0.025} < \frac{NS^2}{\sigma^2} < \chi^2_{0.975}\right) = 0.95$$

Inversion of the inequalities then gives

$$\frac{NS^2}{\chi^2_{N-1}(0.975)} < \sigma_\gamma^2 < \frac{NS^2}{\chi^2_{N-1}(0.025)} \tag{4.6}$$

Following this reasoning to obtain a 95 per cent confidence limit on the velocity dispersion yields $4.2 < \sigma_\gamma < 27.6\,\mathrm{km\,s^{-1}}$, which doesn't sufficiently narrow the range of values. However, if the number of accurately measured γ–velocities is merely doubled ($N = 8$, $N - 1 = 7$), and assuming the dispersion remains approximately

constant, then the 95 per cent confidence interval goes from $5.2 < \sigma_v < 16.1\,\mathrm{km\,s^{-1}}$. More data points need to be obtained for this project before any conclusions can be drawn and before an agreement can be confirmed.

4.7 Conclusions

In this chapter the centre-of-mass radial velocities of four long-period dwarf novae have been accurately measured using the absorption lines from the mass donors around 6400Å, with precautions taken to ensure that systematic errors were minimised or eradicated completely. Twenty-six radial-velocity standards with good spectral types were observed to allow for possible spectral-type mismatch errors. The γ–velocity dispersion, which Kolb & Stehle (1996) proposed would be a good probe of the CV age population, appears to agree with their predicted value ($\sim 8\,\mathrm{km\,s^{-1}}$ c.f. $15\,\mathrm{km\,s^{-1}}$ respectively). Obviously, this is a statistically limited sample, however more suitable observations are available for analysis, and there are still double-lined CVs which can be observed in the future to add to the numbers (see Appendix A for a list of systems).

Chapter 5

Radii of accretion discs in dwarf novae and soft X-ray transients

Summary

Soft X-ray transients (SXTs) are interacting binary systems which are similar to dwarf novae (DN) in all respects bar one – the nature of the accreting object. In dwarf novae the accretor is a white dwarf whilst in soft X-ray transients the accretor is a black hole. Differences between the two types of object are expected during outbursts; the greater mass of a black hole and its stronger influence upon the inner accretion disc are expected to change the way the system reacts. However, in quiescence there is very little accretion onto the central star, and so it may be expected that the two classes of object are very similar, with the mass of the central object being the main factor causing any observed differences in the spectra. The disc instability (DI) theory (see Cannizzo (1993) for an overview) has been generally accepted as providing the explanation for the observed outbursts of dwarf novae (see section 1.7.2). The SXT counterpart to the DI theory which takes account of irradiation from the central X-ray source during outburst will be introduced here.

Inclusion of irradiation naturally accounts for the longer outburst durations for SXTs, and the longer recurrence times which these systems experience (King and Ritter, 1998). A significant difference between irradiated and un-irradiated models is the predicted distribution of the disc mass at the end of, and the fraction of disc mass accreted during an outburst. Un-irradiated discs are anticipated to end the outburst with most of the mass in the outer disc whilst irradiated discs are expected to have most of the remaining disc mass located in the inner disc and having been accreted onto the compact object. This difference leads to the possible discrimination between the models in terms of the measured disc radius, since if mass of low angular momentum is added to the disc during quiescence the radius of the disc shrinks. The amount of shrinkage depends upon the mass in the outer disc compared to that which is added. In this chapter I focus upon this difference, and compare optical measurements of quiescent accretion-disc radii in both DN and SXTs with theoretical expectations to determine which model the observations appear to support.

5.1 Introduction

Soft X-ray transients are a class of low-mass interacting binary star in which the accretor is assumed (generally from radial velocity studies) to be a black hole. As the mass donor in these stars is a low-mass dwarf then the mass ratio, q, for these systems is small, smaller in magnitude even than those of SU UMa-type dwarf novae. In outburst, the higher-mass accreting star in SXTs is expected to influence the appearance of the spectrum for this class of object. However, in quiescence, the importance of the difference in mass of the central objects diminishes, and the expectation is that the spectra from these two classes of object will look similar. This is found to be the case (Marsh, 1998). Balmer, He I and Ca II emission lines are seen in both objects, with double-peaked profiles indicating a disc origin (see section 1.4.1). The spectrum of the mass donor may also be seen in the optical

wavelength-region in both dwarf novae and X-ray transients.

The outbursts of dwarf novae have been well-explained using the disc instability theory (see section 1.7.2) which utilises the thermal-viscous instability which exists in a hydrogen-dominated accretion disc. Outbursts occur when the surface density of an annulus in the disc exceeds a maximum critical value, and the annulus heats on a thermal time-scale in order to reach equilibrium on the upper branch of Fig. 1.16. Whilst doing so it makes adjacent annuli thermally unstable in both the inward and outward directions, thus propagating a thermal pulse which forces most of the disc onto the upper equilibrium branch of the $\Sigma - T_{\rm eff}$ plane. This state persists until one annulus reduces its surface density to the minimum critical value, again starting a chain reaction, and so cooling the disc back into an equilibrium state on the lower branch of Fig. 1.16. Adaptations of this disc instability theory have been established to comprehend the outbursts of SXTs. Allowances for the nature of the accreting object, a black hole, have been included into the theory, since effects such as irradiation of the disc may be non-negligible in these systems. King & Ritter (1998) introduced the concept of the irradiated disc instability model. Irradiation of the disc by the central X-ray source prevents the passage of a cooling front, to lower the disc into quiescence, until most of the disc mass has been accreted. So the system will remain in outburst for a much longer time scale. As a result of this major loss of mass, the recurrence time scale will be much longer; the lost mass has to be replaced before the next outburst can occur. Consequently, the major difference between un-irradiated and irradiated models of SXT outbursts involves the disc-mass distribution at the end of an outburst. Un-irradiated accretion discs do not lose much mass at each outburst, which they end with most of the mass towards the outer disc. Irradiated models predict that a large fraction of the mass of the disc has to be accreted before the disc can return to a cool state, the mass which is left is concentrated in the inner disc. In quiescence, the central accretion rate is greatly reduced and mass of low specific angular momentum is being added to the outer disc, so the radius of the disc will shrink. The amount that the disc

radius decreases depends on the amount of mass in the outer disc compared to that which is added. Measurements of disc radii can then be used to discern whether observations support the irradiated models. Section 5.2 will quantify how much shrinkage is expected to be seen. Then the theoretical limits imposed on the size of an accretion disc will be discussed, followed by the observational constraints that can be determined. Finally, the theory and observations will be compared (Fig. 5.15) and conclusions drawn.

5.2 Disc shrinkage in the irradiated disc instability model

Suppose that at the end of an outburst the accretion disc has a radius R_0 and surface density $\Sigma(R)$, which is a function of radius, R. At the end of an outburst, the disc will be pressing against it's tidal radius, and so the mass transferred through the inner Lagrangian point will have a lower specific angular momentum than the outer disc. Therefore, the disc will shrink. If viscosity is negligible, then mass will accumulate in a ring at the outer edge of the disc – this assumes no disc overflow, which is seen in Doppler images (see Chapter 6). If a mass, ΔM, with circularisation radius, R_C has been added to the outer disc, causing it to shrink to a new radius, R_D then since the specific angular momentum in the disc is given by $VR = \sqrt{GM_1R}$, conservation of angular momentum requires

$$M_{R_D,R_0}\overline{R^{1/2}} + \Delta M R_C^{1/2} = (M_{R_D,R_0} + \Delta M)R_D^{1/2} \tag{5.1}$$

where $M_{R_D,R_0} = \int_{R_D}^{R_0} dm$ is the mass in the disc between radii R_D and R_0 prior to the addition of stream material, and $\overline{R}$ is a weighted mean radius given by

$$\overline{R^{1/2}} = \frac{\int_{R_D}^{R_0} R^{1/2} dm}{\int_{R_D}^{R_0} dm}. \tag{5.2}$$

The smallest possible shrinkage will occur when all the disc mass is concentrated at the outer-disc edge at the end of an outburst (un-irradiated case), so that $M_{R_D,R_0} = M_D$, the total mass of the disc, and $\overline{R} = R_0$. In this case

$$R_D^{1/2} = \frac{M_D R_0^{1/2} + \Delta M R_C^{1/2}}{M_D + \Delta M}. \tag{5.3}$$

Of course this depends on the exact behaviour of the surface density, Σ, on return to quiescence which will in general produce larger changes in disc radius than expected from equation 5.3. For a power-law dependence on radius for the surface density, i.e. $\Sigma \sim R^{\eta}$, it is found that the ratio $x = R_D/R_0$ is controlled by

$$\frac{x^{\eta+5/2}}{2\eta+5} - \left(1 + \frac{\Delta M}{M_D}\right) x^{1/2} + \frac{2\eta+4}{2\eta+5} + \frac{\Delta M}{M_D}\left(\frac{R_C}{R_0}\right)^{1/2} = 0. \tag{5.4}$$

Solutions for R_D/R_0 as a function of $\Delta M/M_D$ are plotted in Fig. 5.1. The figure

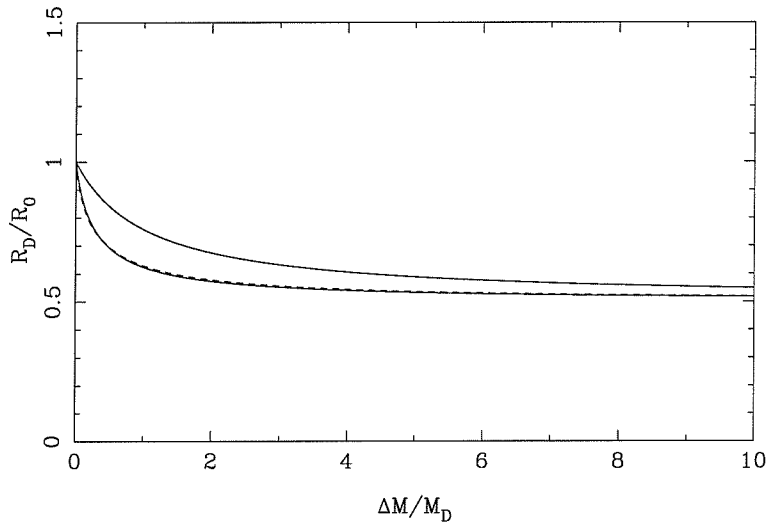

Figure 5.1: Ratio of the disc radius, R_D to its initial value, R_0 is plotted versus the ratio of the mass added, ΔM to the initial disc mass at the end of an outburst, M_D. The upper solid line shows the case where the mass is concentrated at the outer edge of the disc. The lower solid line shows a more realistic case, with $\Sigma \sim R^{-3/4}$. The dashed line illustrates the result for a disc of constant surface density

illustrates that most of the shrinkage will occur before $\Delta M/M_D \approx 1$. Un-irradiated discs lose, at most 10–20 per cent of their disc mass during an outburst (Cannizzo, 1993). Therefore $\Delta M/M_D < 0.25$ and the upper limit is only approached towards

the end of quiescence. Very little shrinkage is therefore expected, particularly in the case of SXTs (if they are assumed not to follow the irradiation model of King & Ritter (1998)), where only a few years accumulation has occurred out of a quiescent interval expected to last several decades. For irradiated discs, the situation is the converse; most of the mass of the disc is accreted, so $\Delta M/M_D >> 1$ by the end of quiescence, and exceeds one soon after the end of outburst. What is clear is that if the irradiation models hold, then some SXT discs should appear close to their circularisation limit.

5.3 Theoretical constraints on accretion disc sizes

Ultimately, the radius of an accretion disc would not be expected to exceed the radius of the Roche lobe surrounding the accreting object (see section 1.3), although there is no physical barrier preventing it from doing so. However the disc radius will be affected by other forces long before it approaches the Roche-lobe radius. The circularisation radius, r_r (see section 1.7), at which the initial stream from the L_1 point impacts with itself and forms a ring around the white dwarf is given by equation (1.26) (Hessman and Hopp, 1990)

$$\frac{r_r}{a} = 0.0859q^{-0.426} \qquad\qquad 0.05 \leq q < 1.$$

The ring that is formed has a finite radial size and, if we assume the particles orbiting within it obey a Keplerian velocity relation, rotates differentially. This causes a shearing flow which generates heat through viscous processes, which is radiated away and so the particles fall deeper into the potential well of the white dwarf. To conserve angular momentum, some particles must move out to larger radii and so a disc is formed. Therefore, r_r is the *minimum* outer radius an accretion disc can have.

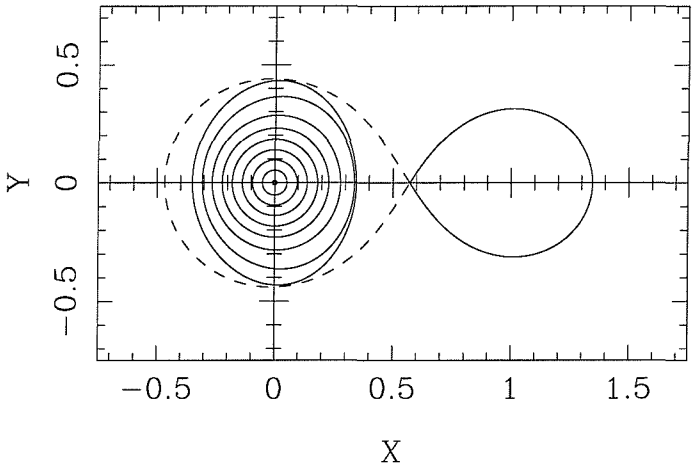

Figure 5.2: Periodic orbits for a binary system with mass ratio, $q = 1/2$

The tidal influence of the mass donor physically limits the maximum disc radius that can be achieved in a CV of mass ratio q. Paczyński (1977) computed single particle orbits, and determined the maximum radius of the last non-intersecting orbit in the outer disc, which can be approximated using (Warner, 1995)

$$\frac{r_{\rm d}(max)}{a} = \frac{0.60}{1+q} \qquad 0.03 < q < 1. \tag{5.5}$$

Figure 5.2 illustrates the periodic orbits as calculated by Paczynski (1977).

5.4 Observational constraints on disc radii

Measurements of the accretion disc radius can be made in several ways. In eclipsing CVs, the width of the disc eclipse can be measured from the first and last contact points, $\pm\phi_d$. In deep eclipses

$$\frac{r_{\rm d}}{a} \approx \tan 2\pi\phi_d - \tan 2\pi\phi_p \tag{5.6}$$

where $\pm\phi_p$ are the points of mid-immersion and mid-emergence of the primary (i.e. from the total eclipse width and total-width at half-depth). In addition, photometry

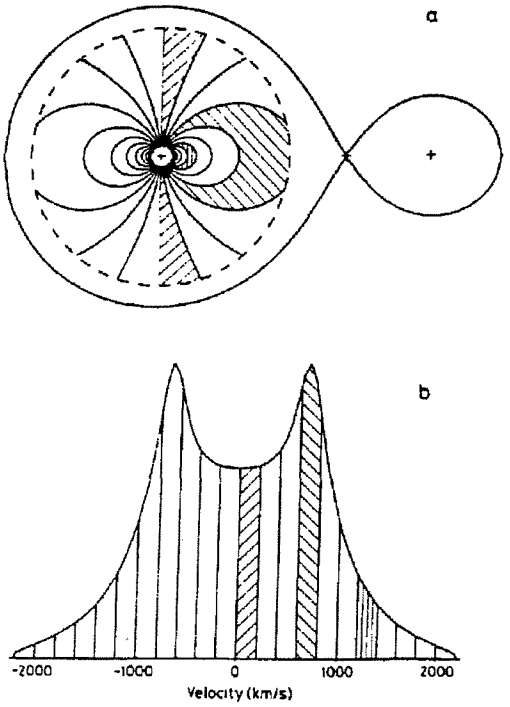

Figure 5.3: (a) A Keplerian disc in a system with a mass ratio $q = 0.15$ viewed at quadrature phase (b) The emission line profile due to the rotating disc, as a function of velocity from the line centre. The shaded bins show which regions of the disc contribute to which parts of the line profile.

during eclipse can allow a determination of the bright-spot radius vector. The bright spot is assumed to form on the outer edge of the accretion disc, and so gives an indication of the radius of the disc. Unfortunately, there are no deeply eclipsing SXTs discovered as yet.

Alternatively, spectra of the emission lines from accretion discs (see section 1.4.1) can be used to determine the velocity of the outer edge of the disc; transforming the relevant theoretical radii into orbital velocities then allows a direct comparison between theory and observations to be made. The emission lines from accretion discs are broad, and often double-peaked (Horne and Marsh, 1986; Smak, 1981). The measured Keplerian velocities in the line wings are thousands of kilometres per second, yet the sound speed in the disc is only of the order of $10\,\mathrm{km\,s^{-1}}$ (from equation 1.20). The line profiles are therefore dominated by Doppler broadening, which enables information about the velocity and intensity distributions in the disc to be extracted.

Fig 5.3 shows the relation between the place of origin of the emission in the accretion disc and the velocity that emission will be seen to have in the line profile. Loci of constant radial velocity resemble a 'dipole field' pattern (Fig. 5.3a). The global emission-line profile is shown in Fig. 5.3b. The line profile is divided into velocity bins corresponding to disc regions between adjacent dipole lines, emission in a particular bin of the line profile will have come from a particular region of the disc. Line cores ($V = 0$) come from material with low radial velocities (moving perpendicular to the line-of-sight), located on the front-back bisector of the disc ($\theta = 0, \pi$). The side of the accretion disc rotating towards the observer will form the blue-shifted wing of the line profile, that rotating away from the observer will form the red-shifted wing. Crescent-shaped regions of the disc close to the white dwarf contribute to the velocity bins far out in each wing of the emission line. The crescent-shaped regions which are truncated by the physical outer edge of the accretion disc produce the enhanced double peaks. These line peaks are formed from the largest area of disc contributing at velocities $V_d \sim \pm v_K(r_d) \sin i$. The maximum intensity in the line profile, I_{max} occurs at $v_K(r_d) \sin i$, equation 1.10 (Smak, 1981). So half the separation of the double peaks in an emission-line profile is an estimate of the projected outer-disc velocity. If the inclination, i, and white dwarf mass, M_1, are known then an estimate of the disc radius can be made using equation (1.23). Double-peaked profiles therefore delineate an outer boundary to the emitting region. Emission lines from different atomic species can be used to measure the accretion disc radius. Most commonly used are the H I, He I and He II lines. Measurements of the peak separations using different species give rise to differing outer-disc velocities, perhaps because each species is formed in a different part of the disc. The distribution of line emission has no definite boundary and so Persson (1988) remarked that the Ca II emission would be best for determining the disc radius due to it's formation in the outermost, coolest parts of the disc.

The catalogue of *Cataclysmic binaries, low-mass X-ray binaries and related objects* (Ritter and Kolb, 1998) contains information about the presence (or absence)

of eclipses, and how many components are visible in the spectrum. The catalogue indicates that there are 34 systems which are double-lined spectroscopic binaries (see Appendix A): these are all able to have accurate orbital parameters calculated from spectroscopic observations. In particular, all thirty-four of these CVs should have accurately measured K_2 values (the radial velocity amplitude of the mass donor). Along with these K_2 values, an estimate of the rotational velocity of the mass donor is possible from the absorption line spectrum. With these two parameters, and assuming that the mass donor is rotating synchronously with the binary star, a value for the mass ratio of the system can be calculated which does not rely in any way upon measurements which use emission lines from the accretion disc. Equation 1.8 relates the mass donor radius as a fraction of the binary separation to the mass ratio of the system. For binary angular velocity Ω, and inclination, i, the projection of the mass donor velocity, $v \sin i$, can be expressed as $\Omega R_2 \sin i$. The radial velocity amplitude of the mass donor K_2 can be written as $K_2 = \Omega a \sin i/(1+q)$, and therefore

$$\frac{v \sin i}{K_2} = \frac{R_2(1+q)}{a}. \tag{5.7}$$

Thus, the mass ratio q can be determined without any dependence on emission line measurements. This is similar to the method used here to deduce accretion disc radii. It has long been known that Doppler shifting of the emission from accretion discs causes double-peaked line profiles (Horne and Marsh, 1986), see also sections 1.4.1& 5.3. The velocities of these peaks reflect the velocity of the outer edge of the rotating disc. To translate this velocity into a measure of the disc radius, other system parameters are needed. Assuming that the gas in the disc obeys a Keplerian velocity relation then equation (1.23) can be used together with equation (1.10) to determine the outer disc velocity as a function of primary mass, inclination and disc radius only,

$$(0.95 \pm 0.05) V_{\rm d}(I_{max}) = \frac{(GM_1)^{1/2} \sin i}{r_{\rm d}^{1/2}}. \tag{5.8}$$

If this is considered in a ratio with the radial velocity amplitude (equation 1.13) then the sin i projection factor cancels and the observations can be directly compared

with the theoretical constraints that are a function of mass ratio alone. In the past, the ratio $V_{\rm d}/K_1$ has been used. Since the K_1 values are badly affected by distortions in the disc, and are especially pronounced for systems of small q (such as SXTs) K_2 is preferentially used here. Using equation (1.13) for the radial velocity amplitude of the mass donor and multiplying by $1/(1+q)$ – then taking the ratio of this by equation (5.8), gives $V_{\rm d}/K_2$ as a function of q alone. Values of $V_{\rm d}/K_2$ can then be plotted versus q, to directly compare with the circularization speed, and the tidally-limited velocities.

A thorough literature search has been carried out to find measurements made in the optical wavelength region of K_2 and q for as many dwarf novae and soft X-ray transients as possible (see Tables 5.1 and 5.2). The uncertainty in K_1 is not avoided altogether because some of the mass ratio measurements are derived using it. Where possible, however, values of mass ratios have been extracted which use K_2 and $v \sin i$ values, or else photometric estimates have been used instead.

5.4.1 Measurements of outer disc velocities using Ca II lines

Spectra of several dwarf novae were taken simultaneously in the near-IR and around Hϵ (3970Å) in order to examine the Ca II emission lines (see Chapter 2 for details). The near-IR triplet are located at 8498.02Å, 8542.09Å and 8662.14Å. The Ca II H and K lines are at wavelengths 3933.67Å and 3968.47Å. All of these lines are very close to hydrogen emission lines. The Ca II H and K lines are situated amongst the middle members of the Balmer series, whilst the near-IR triplet are adjacent to the higher members of the Paschen series. The Ca II lines are all separated from the nearest hydrogen line by approximately $100\,{\rm km\,s^{-1}}$. The ionization potential for Ca II is 11.871 eV, and that for Ca I is only 6 eV (Allen, 1973). Many CVs have singly-peaked emission lines. Whether this is a projection effect – most systems with $i \gtrsim 65°$ show double-peaked lines – or whether it is due to some other form of broadening intrinsic to the disc is uncertain (Marsh, 1998; Marsh and Dhillon, 1997;

Table 5.1: Results from the literature search for dwarf novae in quiescence (listed in descending orbital period length)

Object	mass ratio ±error	method[a]	K_2 ($\mathrm{km\,s^{-1}}$)	V_d ($\mathrm{km\,s^{-1}}$)	refs.[b]
GK Per	0.69±0.12	V	121.2±0.7	402±54	20,21
BV Cen	1.09±0.07	K	128±3	700±–	22
DX And	0.96±0.12	V	105.8±3.8	–	10
RU Peg	0.77±0.03	K	121±2	320±20	16,18
CH UMa	0.49±0.07	K	78±3	–	24
BT Mon	0.854±0.032	V	205±5	–	13
TT Crt	0.8±0.2	K	169±46	413±120	27
EM Cyg	0.88±0.05	V	202±2	305±30	15
V426 Oph	0.98±0.03	V	179±1	450±80	16,23
SS Cyg	0.676±0.024	V	165±2	526±14	16,17
AH Her	0.69±0.02	V	175±2	300±80	16,26
EX Dra	0.84±0.01	V	210±14	349±–	14
RX And	0.42±0.12	O	126±13	273±1	16,19
SS Aur	0.36±0.13	O	174±7	303±67	6,16,19
BD Pav	0.44±0.09	V	278±4	–	6
U Gem	0.363±0.010	K	298±9	564±20	4,5,6
WW Cet	0.40±0.06	K	224±7	358±3	16,25
CN Ori	0.66±0.04	K	231±7	–	6
IP Peg	0.55±0.05	P	305±15	700±50	7,8,9
Z Cha	0.149±0.023	M	430±16	580±50	11,12
HT Cas	0.15±0.03	P	430±25	597±12	1,2,3

[a]P = photometric, M = model, K = from radial velocity amplitude measurements, V = from K_2 and $v \sin i$ measurements, O = Other

[b]1-Horne,Wood & Steining (1991); 2-Marsh (1990); 3-Young, Schneider & Shectman (1981); 4-Long & Gilliland (1999); 5-Stover (1981); 6-Friend et al. (1990a); 7-Wood et al (1989); 8-Marsh (1988); 9-Wolf et al. (1998); 10-Drew et al. (1993); 11-Robinson et al. (1995); 12-Marsh, Horne & Shipman (1987); 13-Smith,Dhillon & Marsh (1998); 14-Billington, Marsh & Dhillon (1996); 15-North et al. (2000); 16-this thesis; 17-Echevarria et al. (1989); 18-Stover (1980); 19-Ritter & Kolb (1998); 20-Morales-Rueda (2000); 21-Garlick et al. (1994); 22-Gilliland (1982); 23-Hessman (1989); 24-Friend et al. (1990b); 25-Tappert et al. (1997); 26-Horne, Wade & Szkody (1986); 27-Szkody et al. (1992).

Lin et al., 1988). Marsh & Dhillon (1997) noted that even if the Balmer lines in a CV only had a single peak, the near-IR Ca II triplet tended to be doubled. With this in mind, Table 5.3 has been compiled for the objects observed at both wavelength regions simultaneously, noting whether the Balmer emission was double-peaked or not, and whether the Ca II emission was observed to be double-peaked. The final column in Table 5.3 indicates whether a 'spike' of emission was visible in the Ca II near-IR triplet (for an illustration of the phenomenon, see Fig. 5.13). The motion of this spike across the Ca II line profiles appears to be phased with the mass donor (see

Table 5.2: Results from the literature search for quiescent soft X-ray transients

Object	mass ratio ±error	method	K_2 ($\mathrm{km\,s^{-1}}$)	V_d ($\mathrm{km\,s^{-1}}$)	refs.[a]
GU Mus	0.133±0.019	K	406±7	470±15	1,2
V616 Mon	0.067±0.01	V	433±3	635±60	3
V404 Cyg	0.060±0.005	V	208.5±0.7	212±91	4,5
QZ Vul	0.042±0.012	V	519.9±5.1	439±35	6
V518 Per	0.116±0.07	V	372±10	500±70	7
J1655-40	0.387±0.050	V	228.2±2.2	550±10	8,9
V2107 Oph	0.014±0.015	V	441±6	700±50	10

[a]1-Orosz et al. (1994); 2-Orosz et al. (1996); 3-Marsh et al. (1994); 4-Casares & Charles (1994); 5-Casares et al. (1992); 6-Harlaftis et al. (1996); 7-Harlaftis et al. (1999); 8-Orosz & Bailyn (1997); 9-Soria et al. (2000); 10-Harlaftis et al. (1997).

section 5.4.1.3). To determine outer disc velocities for the observed objects, using the Ca II near-IR triplet, the line profiles were fit with multiple Gaussians. The input parameters of the Gaussians were varied until they visually fitted the line profiles. A parameter was created to measure the radial velocity of the Gaussian from the rest wavelength of the Ca II line. All the results are listed in Table 5.4. The outer disc velocities using the Ca II atomic species were then calculated from half the average separation of the measured peaks. These have been used where necessary to complete Table 5.1.

5.4.1.1 SS Cygni

SS Cyg is the brightest dwarf nova, rising from a quiescent magnitude of 12.1 to a magnitude of 8.1 in outburst (Ritter and Kolb, 1998). Due to this fact, it is one of the most frequently studied dwarf novae, and in addition both sets of spectral lines from the stellar components of the binary star can be seen in the spectrum (section 4.4.2). This means that masses for both stars can be determined purely from observations of the radial velocity variations. Figure 5.4 shows the spectra obtained from each arm of the spectrograph on the WHT. The blue arm shows strong Balmer emission which appears to have a small double-peak at the centre of the line profile, and the

Table 5.3: Objects whose Ca II peak velocity was measured

Object	Type of CV[a]	double-peak Balmer	double-peak Ca II	Spike in Ca II
SS Cyg	DN UG	Y	Y	Y
RU Peg	DN UG	N	Y	N
WW Cet[b]	DN	N	Y	Y
RX And[b]	DN ZC	N	Y	Y
KT Per	DN ZC	Y	Y	Y
AM Cas[b]	DN ZC	N	N	Y
TZ Per	DN ZC	N	Y	N
FY Per[b]	NL UX	N	N	Y
SS Aur	DN UG	N	Y	Y
CZ Ori	DN UG	N	Y	Y
AB Dra[b]	DN ZC	N	N?	Y

[a]Ritter & Kolb (1998)

[b]in outburst (Mattei, 2000)

Ca II H and K lines have a spike of emission on the blue wing of the line at the time of the observations. The red spectrum shows the Ca II near-IR triplet, but they are not straightforwardly double-peaked. The contribution from the mass donor must be distorting the line profiles, so that the classic accretion disc contribution is disguised. The absorption line at $\sim$ 8680Å is definitely from the mass donor, deduced from follow up time-resolved spectra which show its variation is correctly phased. The best course of action here is to try and remove the spectrum of the mass donor before any line profile measurements are made. Figure 5.5 compares the

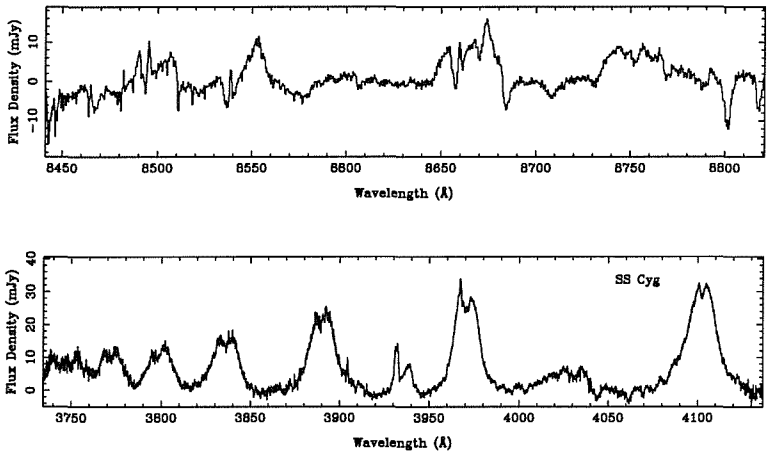

Figure 5.4: Spectra from the two wavelength regions of SS Cyg

Table 5.4: Peak velocities for the Ca II near-IR triplet measured with multiple Gaussian fits

Object	λ8498		λ8542		λ8662	
	red peak	blue peak	red peak	blue peak	red peak	blue peak
	RV[a]±	RV±	RV±	RV±	RV±	RV±
	($km\,s^{-1}$)	($km\,s^{-1}$)	($km\,s^{-1}$)	($km\,s^{-1}$)	($km\,s^{-1}$)	($km\,s^{-1}$)
SS Cyg	306±2	-286±1	306±2	-366±1	410±2	-351±2
RU Peg	326±2	-286±3	387±4	-283±2	323±2	-274±2
WW Cet	–	-200±68	–	–	–	–
RX And	232±2	-313±2	252±1	-279±1	244±1	-301±1
KT Per	–	–	441±35	-384±52	436±31	-383±28
SS Aur	391±5	-246±4	344±57	-254±48	328±67	-258±60
CZ Ori	–	-177±22	–	-199±36	153±32	-172±32

[a]Radial velocity

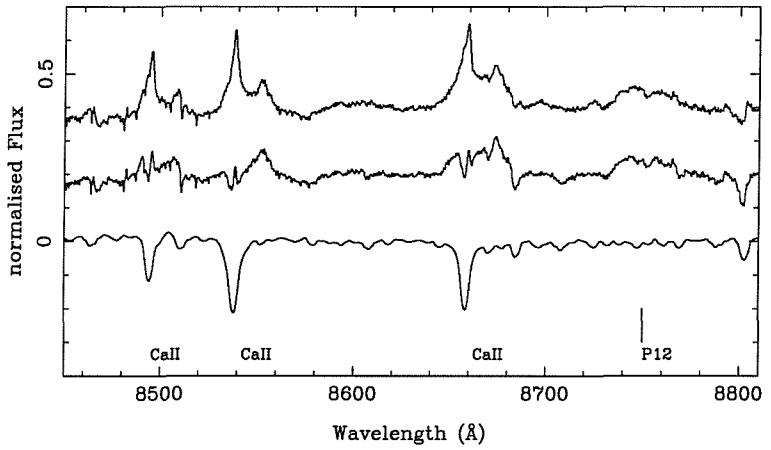

Figure 5.5: The Ca II near-IR triplet of SS Cyg, before removal of the mass donor spectrum (middle), and after removal (top). The spectrum of a K0V star broadened to a rotational velocity value of $100\,\mathrm{km\,s^{-1}}$ was used to do the subtraction (bottom)

Ca II near-IR spectrum before (top panel) and after (bottom panel) subtraction of the absorption spectrum from the mass donor (see section 4.3 for further detail on the procedure followed). The Ca II lines have transformed into double-peaked lines, where the blue peak is stronger than the red one. It is suspected that the stronger blue peak is just an artifact of the subtraction process, due to the Ca II absorption being weaker than expected in a K-type dwarf. However, peak measurements were made using this spectrum.

5.4.1.2 RU Pegasi

RU Peg is a long-period dwarf nova ($P_{\mathrm{orb}} \sim 9\,\mathrm{hr}$) of the U Gem subclass (Ritter and Kolb, 1998). The Balmer emission lines in RU Peg appear single-peaked (Fig. 5.6, bottom panel) whilst the spectrum of the mass donor is apparent even at these short wavelengths. Ritter & Kolb (1998) state that the inclination of the system is $33° \pm 6°$. The double-peaked nature of the Ca II near-IR triplet here may be the influence of the spectrum from the mass donor. The line profiles look like absorption superimposed upon emission rather than a double-cusped profile seen as a result of a rotating accretion disc. In RU Peg, the Ca II H and K line profiles appear to have sharp emission spikes in the middle of the line profiles.

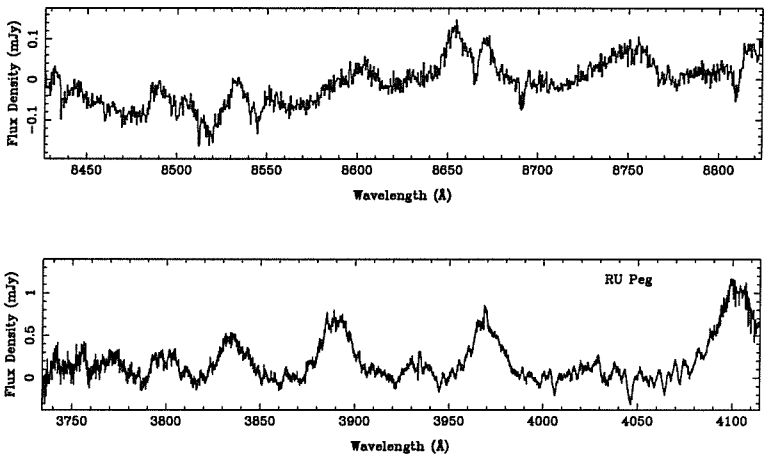

Figure 5.6: Spectra from the two wavelength regions of RU Peg

5.4.1.3 RX Andromeda

RX And is a dwarf nova of the Z Cam subclass, meaning that it spends quite a lot of time in a high state. RX And appeared to be on the decline from an outburst maximum during the WHT observations, deduced from the appearance of Hϵ with large absorption wings and a central emission core. Figure 5.7 shows the spectra obtained with both arms of the ISIS spectrograph on the WHT. The Balmer emission lines all have emission cores with wide absorption wings. The Paschen lines appear to be quite weak at this stage (top panel of Fig. 5.7), and the three Ca II near-IR triplet lines are more prominent, with two peaks, the larger one being on the blue side of the line profile in each case.

Figure 5.8 shows the Gaussian fit to the Ca II 8662 Å emission line. The fit is composed of two Gaussians, with the height, full-width half-maximum (FWHM), and radial velocities allowed to vary during the fitting process. Manipulating the values in Table 5.4 gives the average measured half peak-separation as $273 \pm 3\,\mathrm{km\,s^{-1}}$. Further observations of this system taken using the INT/IDS telescope/instrument combination (see section 2.2.2) caught the system in a standstill state, and cover over half an orbital period in total. The data were taken on two nights separated by two days, the weather on the second of which was much worse. The data show

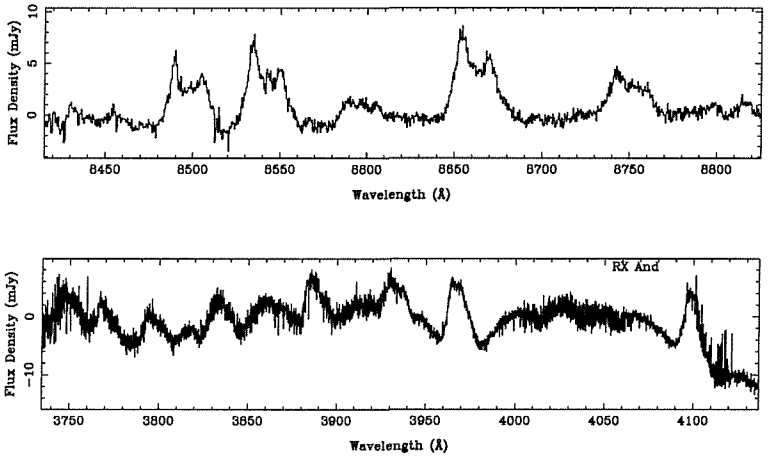

Figure 5.7: Red (top) and Blue (bottom) arm spectra of RX And. The blue spectrum indicates that the system was in outburst at the time of the observation

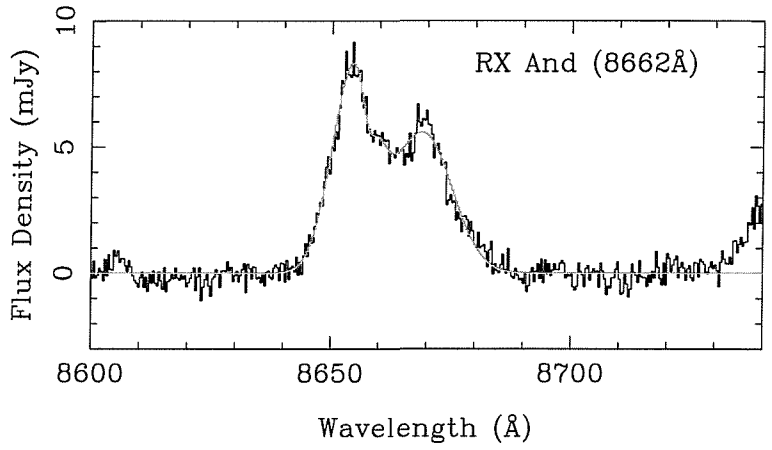

Figure 5.8: The Gaussian fit to the 8662Å calcium line

an obvious 'spike' of emission in the Ca II triplet lines (see Figs. 5.9 & 5.10), which is phased with the motion of the mass donor. As RX And doesn't have a readily available published K_2 value, this could be an excellent and sensitive new method to determine the mass donor radial velocity curve for this object, and indeed for other systems in which the contribution from the mass donor is completely dwarfed in the optical wavelength range by that from the accretion disc. Figure 5.9 shows the variation in the position of the emission spike in the Ca II line profiles, with each spectrum marked with the binary phase calculated using the ephemeris of Kaitchuck (1989) (whose zero phase point was defined as the superior conjunction of the white dwarf). The extra emission component to the Ca II line profiles (hereafter,

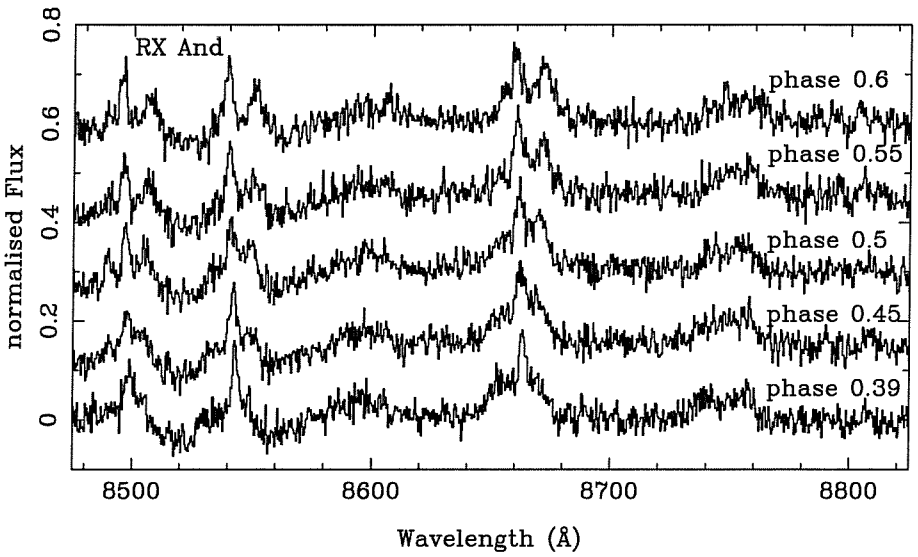

Figure 5.9: The appearance of the emission spike in the RX And spectra

spike) appears at the red-wing/centre of the line profile at phase 0.4, and moves to negative radial velocities over the next quarter of a binary orbit. Two peaks are visible at phases around 0.5-0.6, and that from the mass donor appears on the blue wing of the line. Figure 5.10 shows the trailed spectra obtained with the INT/IDS setup. The first night's data are in the bottom panel. As can be seen from the top panel, the weather had deteriorated significantly by the time the next data were obtained. This resulted in the emission spike being barely visible, and so a radial velocity analysis of the data could not reveal an unambiguous value of K_2. Figure 5.11 shows the circular orbit fit to the radial velocity measurements of the spike in the Ca II near-IR triplet. A circular orbit fit made to all the points yielded a K_2 value of $126 \pm 13\,\mathrm{km\,s^{-1}}$, which is less than half the predicted value using the previously determined emission line value – $K_1 = 117 \pm 10$ $\mathrm{km\,s^{-1}}$ (Kaitchuck et al., 1988) – and mass ratio, $q = 0.42 \pm 0.12$ (Ritter and Kolb, 1998). This may be due to the distribution of Ca II emission over the surface of the mass donor (see Fig. 5.12). It is likely to be concentrated at the face closest to the inner Lagrangian point.

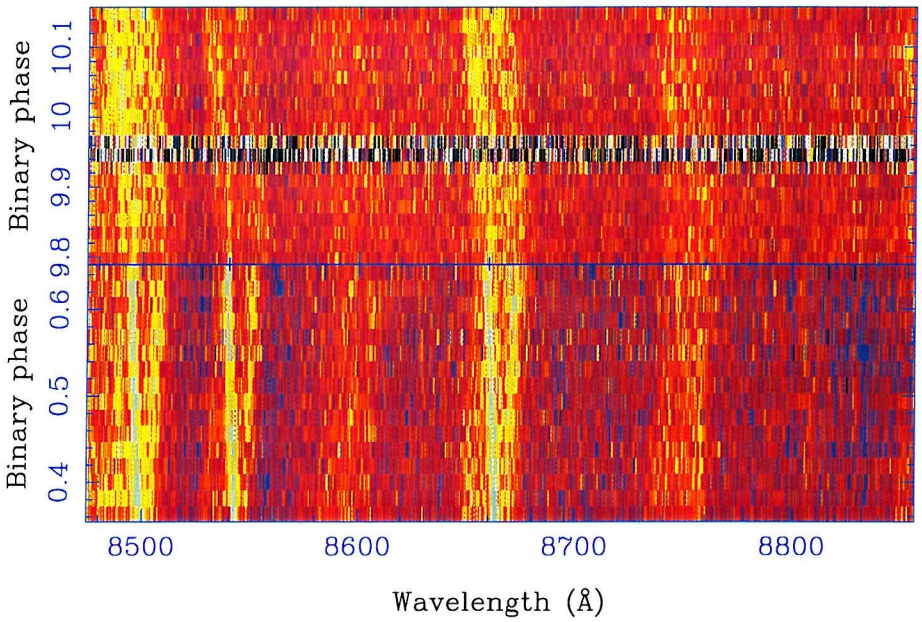

Figure 5.10: Trailed spectra of RX And. The emission spike is visible in the first nights data (bottom panel) but the data is of much worse quality two nights later (top panel) and so it is barely visible

5.4.1.4 KT Persei

KT Per is defined as another member of the Z Cam variety of dwarf novae. Figure 5.13 shows the red and blue-arm spectra. The Balmer lines (bottom panel) are broad with no obvious sign of a double-peaked profile. The Ca II lines are dominated by an emission spike right in the centre of the line profile. Towards either side of this appears to be a peak, which could be the double-peak being looked for. The Paschen lines are not very strong in this object, which was in a quiescent state at the time of observations (Mattei, 2000). The exposures were 25 minutes long and two were taken. From the first to the second spectrum there is a definite shift in the position of the spike, see Fig. 5.14. The dotted line shows the second spectrum taken, and the unbroken line shows the first spectrum, started 25 minutes before it. KT Per has no mass donor spectral type or component masses listed in Ritter & Kolb (1998), so this could be an accurate way to determine masses in this system.

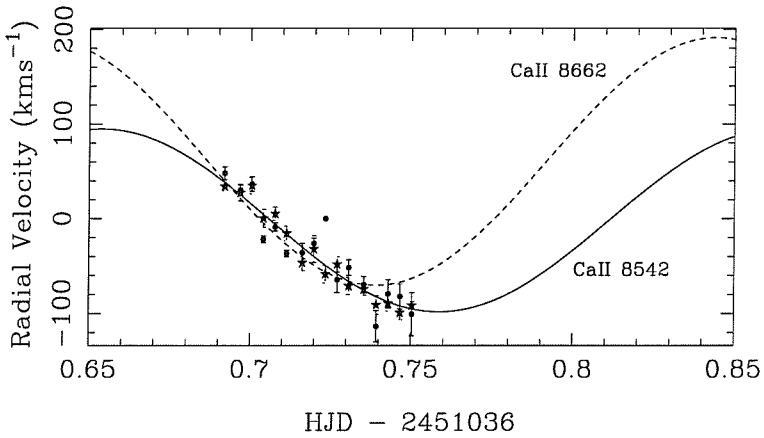

Figure 5.11: Circular orbit fit to the radial velocities of RX And. The fit derived from the 8542Å measurements is shown as a solid line, whilst the best fit to the 8662Å points is shown as a dashed line

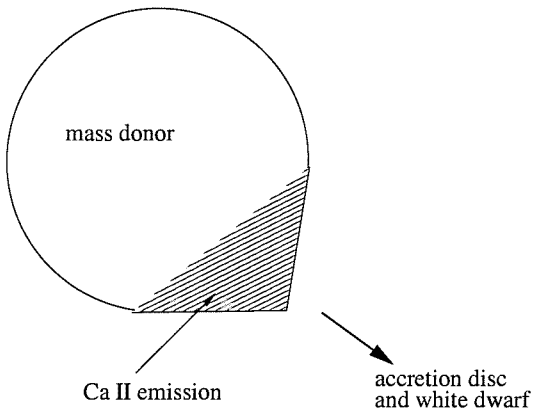

Figure 5.12: The likely distribution of Ca II over the mass donor in RX And

5.5 Discussion

Figure 5.15 plots V_d/K_2 (collected from the literature, see Tables 5.1& 5.2) versus the logarithm of the mass ratio, q – to ensure that the smaller mass-ratio objects were clearly plotted. To recap, elimination of any orbital inclination dependence is the reason for plotting the ratio V_d/K_2 on the y-axis. The points plotted as triangles are dwarf novae data, and the squares are the data for soft X-ray transients. Also plotted is the circularisation speed of the accretion disc at that particular mass ratio (given by equation (1.26)). The velocity of the last stable non-intersecting orbit, calculated following the method of Paczynski (1977) is marked on the plot

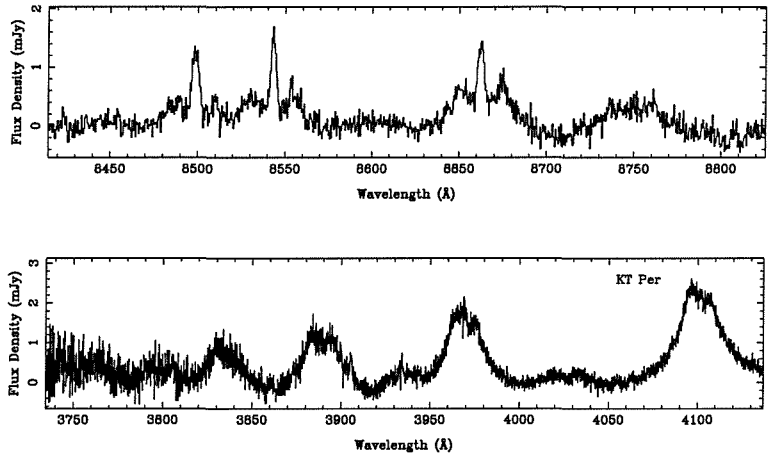

Figure 5.13: The spectra of KT Per

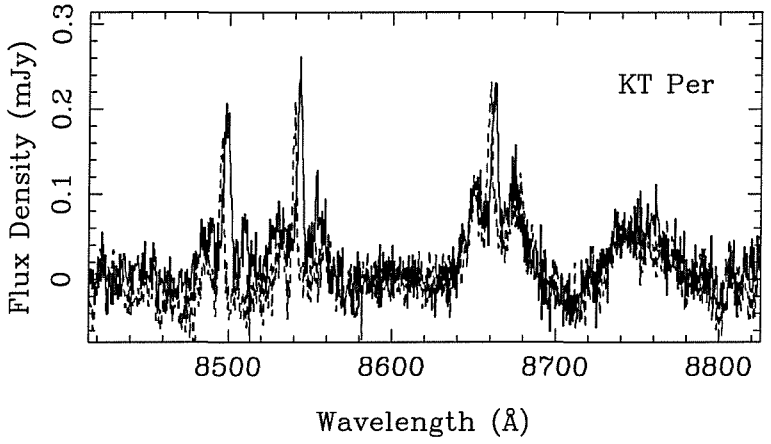

Figure 5.14: Variation in the position of the spike in KT Per from one exposure to the next

as a solid line. Systems which lie below this orbit crossing limit appear to possess large discs - those near to the circularisation speed apparently have small discs. There are two forbidden zones in Fig. 5.15; it should not be possible for a disc to have a radius smaller than the circularisation limit – so no objects should be seen in the region labelled 'small discs'. In addition, it should not be possible for discs to exceed the Paczynski limit by any significant amount, since tidal stresses are a strong function of radius; therefore no systems should be plotted in the region labelled 'large discs'.

None of the measured Ca II peaks, or any values taken from the literature indicate that we are seeing a disc close to its circularisation limit. This conclusion can only

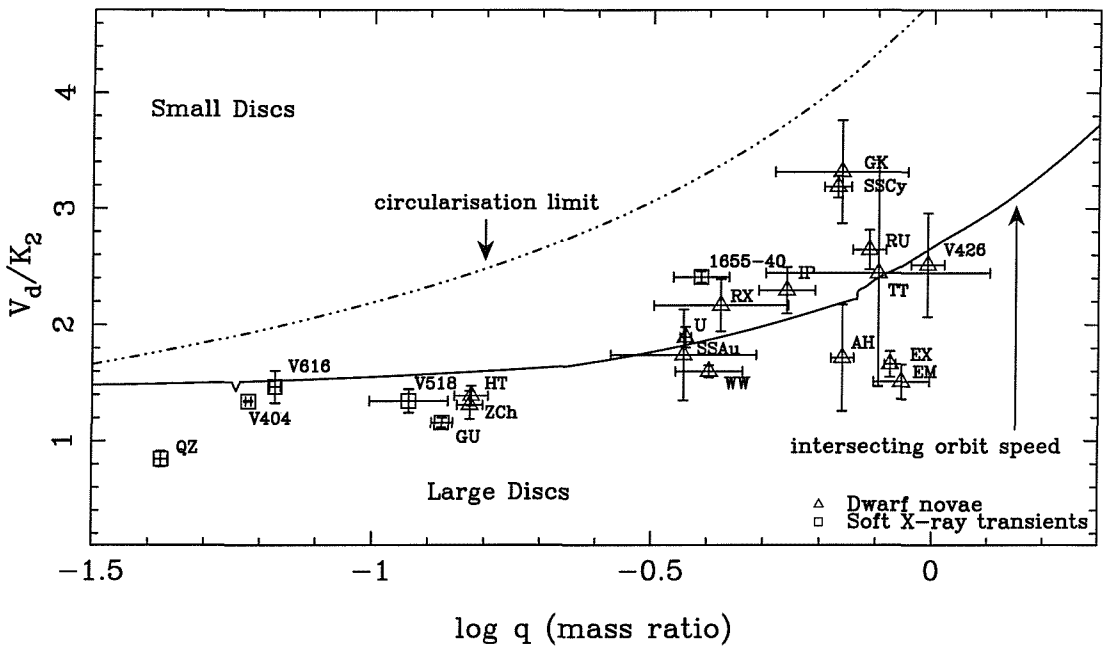

Figure 5.15: Plot of the ratio of the measured outer-disc velocity to the amplitude of the mass donor radial velocities versus the logarithm of the mass ratio for dwarf novae (triangles) and soft X-ray transients (squares). Also plotted are the circularisation velocities for each mass ratio, and the velocity of the outermost stable, non-intersecting orbit (Paczynski, 1977). Located near to each marked point is a letter code indicating the name of the object[a]

[a]see Table 5.5 for details

be altered by very erroneous mass ratios, which are very unlikely given the advances in instrument/detector combinations which have become available over the past ten years. This conclusion is evidence against significant disc shrinkage and the small disc mass which is a prediction of the irradiated disc instability model. The positions of the data in the plot pose a problem in themselves however. The double-peaks measured in many systems are closer together than a tidally-limited disc would predict. Previous explanations have invoked 'sub-Keplerian' disc velocities at the outer edges; in other words the discs are rotating more slowly than the circular speed at their outer edges. This is physically unlikely; were the disc rotating significantly below the Keplerian value, a large outward pressure gradient would be required to compensate for the short-fall in centripetal acceleration. Such a gradient can not be sustained in the quiescent discs of dwarf novae and soft X-ray transients (cool and thin). Also the idea that the discs are larger than the tidal limit has to be rejected

Table 5.5: Key to the labels given to the objects plotted in Figure 5.15

Key	Object	Alternate name	Key	Object	Alternate name
QZ	QZ Vul	GS2000+25	1655	GRO J1655-40	Nova Scorpii 1994
V404	V404 Cyg	GS2023+338	IP	IP Peg	
V616	V616 Mon	A0620-00	AH	AH Her	
V518	V518 Per	GRO J0422+32	GK	GK Per	
GU	GU Mus	GS 1124-68	SSCy	SS Cyg	
ZCh	Z Cha		RU	RU Peg	
HT	HT Cas		TT	TT Crt	
WW	WW Cet		EX	EX Dra	HS 1804+6753
SSAu	SS Aur		EM	EM Cyg	
U	U Gem		V426	V426 Oph	
RX	RX And				

outright; in some cases the size of the disc is apparently larger than the Roche lobe of the white dwarf which is just not physically plausible. Only viscous forces can keep the disc large, but these are not thought to be significant in quiescence. Other explanations need to be considered for these objects. The emission lines in dwarf novae and soft X-ray transients are well-known to be optically thick (Horne and Marsh, 1986). Marsh & Dhillon (Marsh and Dhillon, 1997) stated that these lines may well be intrinsically broad at any point in the disc, which will affect the emission line profiles by pulling in the peaks towards zero velocity, and in extreme cases, make the line profiles appear singly-peaked. There are many cases where only single-peaked emission lines can be seen (see Table 5.1 for examples). Another possible explanation is failure to account for emission components from the mass donor in the emission line profiles. In an orbitally averaged profile, these components would appear at velocities equal to $\pm K_2$, and if significant, they would pull points in Fig. 5.15 downwards along the y-axis. These are easily recognised in the line profiles, see section 5.4.1 for examples, but may not always have been removed for $V_{\rm d}$ measurements (RX And here, for example). Finally, a low instrumental resolution can have the same effect as intrinsic broadening, as demonstrated by Marsh, Robinson & Wood (1994) in their study of V616 Mon. I believe that all of these reasons could explain the apparent abundance of objects situated in the

'forbidden zone' below the Paczynski limit in Fig. 5.15.

This analysis, whilst apparently posing problems for the irradiated disc instability model needs to be refined somewhat before that conclusion can be drawn with any certainty.

5.6 Conclusions

Outer disc velocities and radial velocity amplitudes for mass donors in many dwarf novae and soft X-ray transients have been collected from data and published literature, in order that comparisons be made between the observed data and theoretical constraints. The conclusion can be drawn that the discs in most of the systems lie near the tidal limit. Many of the objects have outer disc velocities suggestive of a radius above that expected for a tidally limited disc. It is suggested that this is a result of intrinsic broadening of the line profiles from discs. For soft X-ray transients, the discs are all apparently larger than would be expected following the predictions of the irradiation model; a large fraction of the disc mass is accreted during outburst, and so addition of low angular momentum material will cause a shrinkage of the disc which would be expected to be reflected in the separation of the double peaks in the line profiles at quiescence.

Chapter 6

Doppler imaging of long-period dwarf novae in quiescence

Summary

Doppler tomography is a technique devised to image the accretion discs in Cataclysmic Variables (Marsh and Horne, 1988). In this Chapter, the Hα disc-emission is mapped for four long-period ($6 < P_{\rm orb} \leq 7$ hr) dwarf novae, EM Cyg, V426 Oph, SS Cyg and AH Her. The maps of all four systems are unusual in the sense that emission in them does not appear as predicted for dwarf novae in a quiescent state (see Fig. 6.2). In many other dwarf novae Balmer emission has been deduced to originate mainly from the accretion disc (Marsh, 2001), with perhaps some contribution from the impact site of the gas stream at the outer edge of the disc. The accretion disc appears in Doppler maps as an annulus of emission with its inner and outer limits at the velocities of the outer and inner edges of the disc respectively. None of the four maps here unambiguously display this emission pattern. The emission in EM Cyg can be interpreted as that from a disc, although it doesn't appear consistently ring-like. The emission in SS Cyg resembles a annulus (albeit a very thick one)

centred on the velocity of the white dwarf, with a very low outer-disc velocity. All the maps have emission which is apparently located at sub-Keplerian velocities (see Chapter 5). There is also unexpected emission in the bottom-central regions of the maps of SS Cyg and AH Her. V426 Oph has a peculiar region of emission around the centre-of-mass of the system, and no obvious disc. Are the appearance of these Doppler images just a result of creating them using Hα emission, which is inherently different from other members of the Balmer series? I present possible explanations for the appearances of the Doppler maps, and discuss their suitability as solutions for the Hα emission distribution observed in these four dwarf novae.

6.1 Doppler tomography: an introduction

CVs subtend a very small angle on the sky, typically of the order $\lesssim 10^{-4}$ arcsec. This means that direct imaging of the components (such as the accretion disc and gas stream) is impossible, as they behave as point-sources of light, and a resolution of 10^{-6} arc seconds is really needed to analyse the constituent components. Emission from the accretion disc results in strongly broadened spectral lines due to the high velocities in the inner disc (usually thousands of $\mathrm{km\,s^{-1}}$). Emission line profiles are dominated by Doppler broadening, and are not significantly affected by the local thermal profile (which is $\sim 10\,\mathrm{km\,s^{-1}}$), however, there may be other broadening mechanisms (Marsh & Dhillon (1997), and Chapter 5). Certain regions in the disc contribute to particular parts of the line profile at a velocity equal to that of the radial velocity of the disc region with respect to the observer. Any asymmetry in the line emissivity over the disc will enhance a specific bin in the line profile, which as the binary star rotates, will trace a sinusoidal path in the radial-velocity – orbital-phase plane, an 'S-wave' (Smak, 1985). The period of this sinusoid (see equation 6.1) will be the orbital period, P_{orb}, of the binary star. The amplitude of the sinusoidal variation gives the true velocity of the gas causing the emission, and its phasing gives the phase angle of the point of origin. Given a particular line

emissivity distribution, the corresponding phase-dependent set of line profiles can be predicted. Doppler tomography was developed in order to carry out the reverse operation – to reconstruct the emissivity distribution from a time-series sequence of line profiles covering a full binary period.

The mass donor (secondary) in CVs co-rotates with the binary star, and so the most obvious reference frame for a coordinate system is one which rotates with the system. In this rotating frame the x-axis is chosen to be in the direction from the white dwarf to the mass donor, the y-axis is in the direction of motion of the mass donor in the orbital plane, and the z-axis is defined to be perpendicular to the orbital plane of the CV. So, the radial velocity of a point in the binary at orbital phase ϕ is given by

$$v_R(\phi) = \gamma - V_X \cos(2\pi\phi) + V_Y \sin(2\pi\phi) \tag{6.1}$$

where V_X & V_Y are velocity vector components relative to the inertial frame (as seen by the observer), γ is the radial velocity of the binary system itself and i is the angle the orbital axis of the binary star makes with the line-of-sight to the observer. The line profile can be viewed then, as the sum of all contributions across the disc, each represented by a sinusoidal wave. To relate these velocities to physical areas of the disc, a velocity field must be assumed, which in this case can be a Keplerian one. A time-series sequence of line profiles can then be used to reconstruct an orbit-averaged picture of the line emission. Marsh & Horne (1988) developed Doppler tomography to enable creation of such image reconstructions using the observed disc-emission line profiles in CVs. However, due to the differing nature of the velocity fields of various components in the system it was decided that a reconstruction in velocity space should be used. The velocities are measured in the inertial frame and then projected onto the rotating frame, to make certain that steady flows are measured by phase independent coordinates. Each point (V_X, V_Y) represents a sinusoidal curve with amplitude V_X and V_Y. The centres-of-mass of the two stars perform a solid body rotation in the frame of the binary star, and their velocity vectors are

mapped onto the V_Y axis at $+K_2$ and $-K_1$ for the mass donor and white dwarf respectively. Lines of equal radial velocity in spatial coordinates map to straight lines in velocity coordinates. The wings of the line profile come from material in orbit close to the white dwarf, while the line centre comes from lower velocity gas further out. Assuming a Keplerian velocity field for the disc means that gas at particular velocities in the Doppler image can be associated with a specific spatial position within the binary frame – essentially, the place of origin of the emission can be deduced. However, because the image reconstruction is done in velocity space, a non-Keplerian steady flow occurring within the frame of the binary star can also be mapped, as any point of it will also trace out a sine wave over the course of an orbital period. This means that emission having an origin in the gas stream or on the mass donor can be identified too.

Doppler tomography does have several basic assumptions. They are:

i. All points in the binary system are equally visible at all times.

ii. The flux from any point fixed in the rotating frame is constant.

iii. Motion is confined to the orbital plane.

iv. Non-Doppler broadening is negligible.

Point (i) is very often violated in CVs. For example, the disc may be obscuring the bright spot, if the inclination is right, and it may not be visible throughout an orbital cycle. Likewise, the hemisphere of the mass donor facing the white dwarf may be partially obscured at phase 0.5. With regard to point (ii), it is not the case that the flux from any point is constant throughout an orbit of the binary star. The hemisphere of the mass donor facing the white dwarf is again here a good example, because irradiation from the white dwarf and boundary layer causes an increase of incident flux to the mass donor's face. This affects the appearance of the absorption lines from the star at phase 0.5 (Davey and Smith, 1992). With regard

to point (iii), it is perhaps a little naive to assume that all the motion in CVs is confined to the orbital plane. This may be a reasonable assumption in the case of non-magnetic CVs, but if there are substantial magnetic fields present then they will affect the motion of the gas. Since the magnetic fields are oriented out of the orbital plane, one may expect to see some motion in this direction. Finally, considering point (iv), Doppler shifting may not be the only broadening mechanisms. Effects like Stark broadening may make a considerable contribution to the line profile shape in particular emission lines (Lin et al., 1988).

The Doppler maps in this thesis were created using the 'DOPPLER' FORTRAN code (developed by Tom Marsh). It is based on the 'MEMSYS' optimiser by Skilling & Bryan (1984). The DOPPLER code helps to select the desired compromise between fitting the data and maximising the entropy. The TEST statistic (which ensures convergence) measures the angle (θ) between $\nabla\chi^2$ and ∇S;

$$TEST = \frac{1}{2}\left|\frac{\nabla\chi^2}{|\nabla\chi^2|} - \frac{\nabla S}{|\nabla S|}\right|^2 \sim 1 - \cos\theta \qquad (6.2)$$

The iterations converge when the value of this TEST statistic falls below 10^{-5}. The process is as follows:

i. The data are continuum-subtracted and placed onto a uniform velocity scale, covering only the spectral line to be mapped plus a little extra ($\sim 100\,\mathrm{km\,s^{-1}}$ either side). An accurate ephemeris is then applied, and a file created which can be handled by the DOPPLER code.

ii. The Doppler image is created. The choice of pixel size, number of pixels, number of images, number of lines, wavelength(s), instrument FWHM, and the type of default image to use are chosen at this stage.

iii. Scale the initial image to minimise χ^2. During the iterations, the image can only be tweaked by a small amount, so if the initial image choice is poor, most of the iterations are spent trying to improve it. This is very CPU intensive, and can take a long time. The best option is to make sure the initial choice of image is the best possible.

iv. Iterate the image to reach a specified χ^2. When the solution converges, the iterations are stopped (i.e. when the TEST statistic reaches a value below 10^{-5}).

These points are then repeated until the desired image is obtained. If the χ^2 is set too low, then the image becomes dominated by the noise, and looks very fragmented. If the χ^2 isn't set low enough, the image has a smeared-out appearance. For any image the predicted data can be calculated at any orbital phase. The predicted data is then compared to the observed data using the χ^2 statistic, which measures how close to the observations the predicted fit is. In theory, the χ^2 can be minimized to fit the data as closely as possible, but this is not the best image to choose. Noise in the data is amplified so much that the image becomes impossible to interpret. To get the best image, χ^2 is lowered until the predicted and observed data are consistent (e.g. $\chi^2/N = 1$). This constraint is satisfied by many images, and so to allow only one to be chosen another constraint must be used. This is where entropy comes in. The image chosen is the one of maximum entropy. The entropy, S, of an image, I, is $S = -\sum_i p_i \ln p_i$. In this equation, $p_i = I_i / \sum_j I_j$ selects the most uniform of all the images. However, the distribution of line emission is generally *not* uniform and so a revised version of the entropy is used:

$$S = -\sum_{i=1}^{n} p_i \log \frac{p_i}{q_i}$$

where p_i is defined as before and $q_i = J_i / \sum_j J_j$ and J is the default image. With no data constraints, S is maximised when $p_i = q_i$ - i.e. image I has an identical form to image J, apart from an arbitrary multiplicative constant.

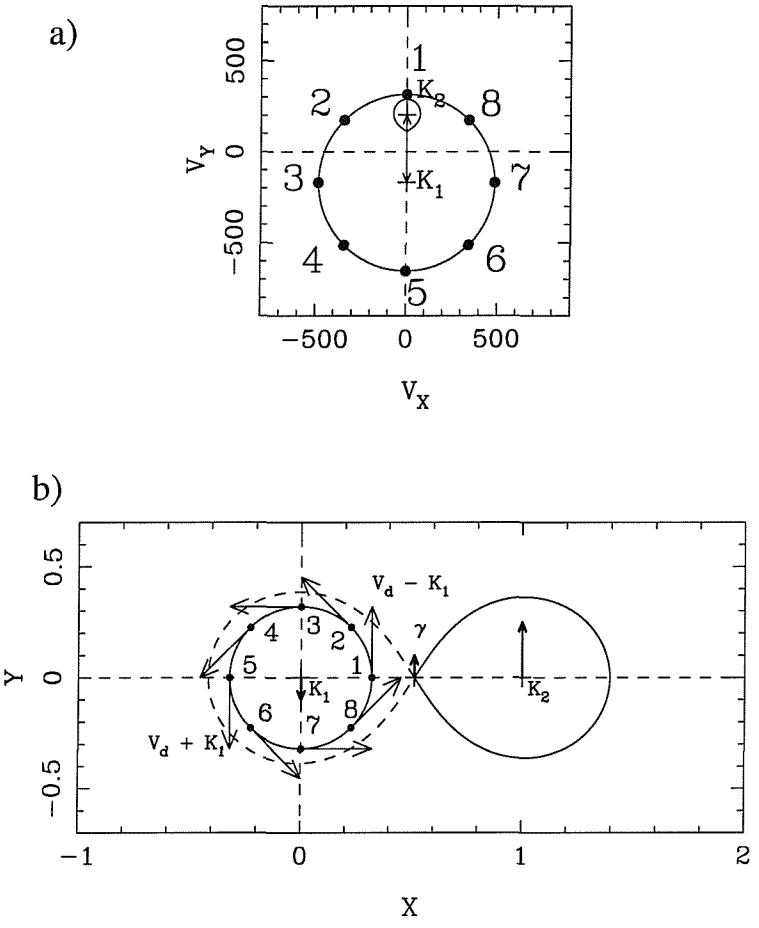

Figure 6.1: The relationship between a) velocity coordinates and b) spatial coordinates when interpreting Doppler maps. See text for explanation

6.2 Interpreting Doppler maps

Doppler maps are transformations of the line profiles into velocity space so the image does not represent the spatial distribution of the gas in the binary star, it represents the velocity distribution of the emission.

Figure 6.1 shows the relationship between an image in velocity space and one in 'normal' spatial coordinates. It must be noted that lines of constant radial velocity appear always straight in a Doppler map (a map in velocity coordinates). The orientation of these lines on the map depends on the phase angle of the binary system. With the binary star at phase 0.25, as shown in Fig. 6.1b, these lines will be oriented parallel with the V_X axis. The loci of constant radial velocity are shown

in Fig. 5.3, resembling a dipole pattern. Points 1 – 8 in Fig. 6.1b mark points of the outer edge of the accretion disc, with point 1 closest to the L_1 point and the mass donor, and point 5 furthest away. These points are again shown in Fig. 6.1a at the positions they would appear in a Doppler map. This is due to the fact that the velocity vector in a Keplerian disc is perpendicular to the radius vector, so all points are rotated anti-clockwise by 90° in the transformation. The centre-of-mass of the system appears at the origin of the velocity coordinates, and the inner Lagrangian point is located nearby. Transformation of the mass donor from spatial to velocity coordinates is also simple, as it is fixed within the rotating frame of the binary star. Each point $\mathbf{r}$ has a velocity $\mathbf{\Omega} \wedge r$, which is linear in the perpendicular distance from the axis of rotation. This means that the shape of the mass donor projected onto the plane of the orbit is preserved.

The basic features to look for when trying to interpret a Doppler reconstruction of a CV are the accretion disc and any emissions from the mass donor or gas stream. As previously explained, due to the nature of the double-peaked emission line profile caused by a rotating disc, the image in velocity space shows an annulus of emission centred on the velocity of the white dwarf. The outer limit of the 'ring' corresponds to the inner edge of the disc (high velocities), and the inner edge of the ring corresponds to the outer-disc velocity. Not assuming a velocity field means that those components whose velocities do not obey a Keplerian relation, but which are steady flows in the frame of the binary system, can be mapped by sinusoids. This means that when the Doppler map is constructed, the emission from them manifests itself as spots. This is how emission from the mass donor, and the gas stream, can be identified.

Doppler mapping has been used extensively on the Balmer emission lines, and on He I and He II emission. All these emission lines have their main source at the accretion disc (of course there will be contributions from the mass donor, and this is where obtaining a Doppler map is important). The origins of various emission components can be determined, as can relative sizes and positions of accretion disc

emission coming from differing atomic species, enabling a picture of the CV to be built up from different wavelengths. Marsh (2001) provides a review of the subject and its discoveries so far in relation to CVs. A thorough analysis of several applications of this method to real CV data are given in Marsh & Horne (1990) and Marsh et al. (1990).

6.3 Doppler images using the Hα emission line

As covered in Chapter 2, observations were made of four dwarf novae in June 1997. The resulting time-series of spectra cover a complete orbital period for each object. Once the spectra had been placed onto a uniform velocity scale, they were fed into a maximum-entropy routine, to determine the reconstructed image which minimised χ^2 whilst maximising the entropy (S) relative to a default image chosen by the user.

Figure 6.2 presents the Doppler maps obtained using the Hα emission line (at 6562.760Å) for all four dwarf novae observed. The minimum number of phases around an orbit obtained was 64 (for AH Her), and the maximum number 102 (for EM Cyg). The Doppler maps are surrounded by the observed (bottom panel) and calculated (top panel) data. The appearance of the predicted data gives a good indication of how accurate the Doppler map is. In the following sections each of the Doppler maps will be discussed, and their various characteristics noted. The surprising result of this investigation is simply that none of the four maps look as they were expected to – possible reasons are noted.

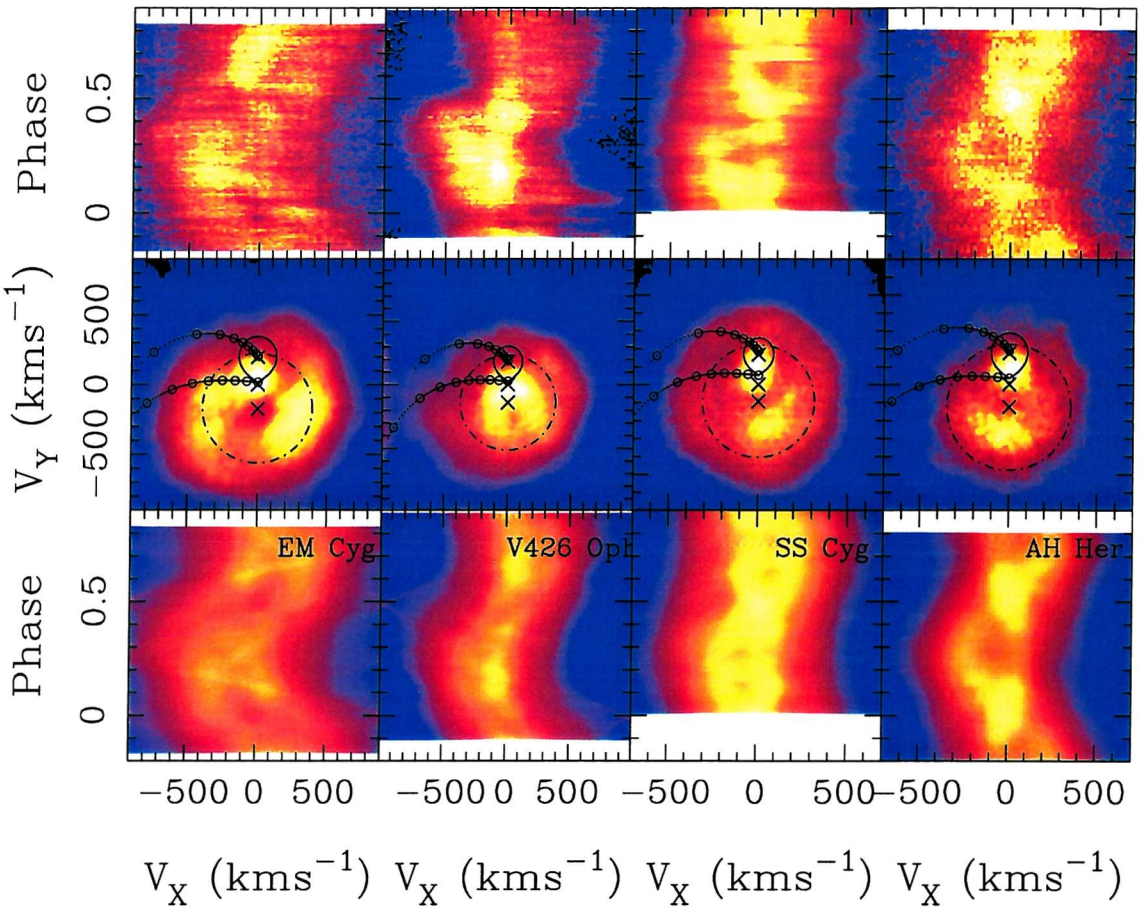

Figure 6.2: The Doppler maps of all four dwarf novae bracketed by the observed data (*top panels*), and the predicted data (*bottom panels*). The objects appear in decreasing orbital-period order from left to right. Velocities of the white-dwarf, mass donor and centre-of-mass of the system are marked with crosses. Open circles denote (in units of $0.1\,R_{L_1}$) the path of the gas stream. The rings marked on the Doppler maps represent the outer disc velocity for a disc of size $0.8R_{L_1}$

6.3.1 EM Cygni

EM Cygni is the only system classified in Ritter & Kolb (1998) as eclipsing for which we have calculated a Doppler map. It has an eclipse of the accretion disc once every orbit, but the inclination is such that the white dwarf itself is not eclipsed. The accretion disc eclipse can be seen in Fig. 6.2, leftmost column, top panel as a 'Z-shaped' feature around phase zero (see Fig. 6.4 for an expanded view). It starts in the blue wing of the emission line ($\sim 650\,\mathrm{km\,s^{-1}}$) and then goes into the red wing ($\sim 550\,\mathrm{km\,s^{-1}}$). This is the classic signature of a rotational distur-

bance, where blue-shifted material is eclipsed before red-shifted emission caused by an accretion disc (Young and Schneider, 1980; Greenstein and Kraft, 1994). The data also appears to show some sort of absorption around phase 0.5 (when the accretion disc/white dwarf is closest to the observer along the line-of-sight), which appears in the blue wing at around $750\,\mathrm{km\,s^{-1}}$, then stops in the red-wing at only $\sim 400\,\mathrm{km\,s^{-1}}$.

EM Cyg has the Doppler map which most resembles that which would be expected from a binary star of this type. Column 1 of Fig. 6.2 shows the map (centre panel) flanked by the observed data (top panel) and the predicted data (bottom panel). The dashed line marking a circle is at a velocity of $430\,\mathrm{km\,s^{-1}}$. This is the expected Keplerian velocity for the outer edge of a disc with radius $0.8\mathrm{R}_{L_1}$. This is large, quite probably much larger than the actual size of the disc in EM Cyg, and therefore it represents the lowest possible velocity at which accretion disc emission should be seen. From Fig. 6.3 this is clearly *not* the case. A significant fraction of the apparent-disc emission is coming from velocities lower than this – "sub-Keplerian" velocities.

Fig. 6.3 shows more closely the reconstructed Doppler tomogram of the Hα emission line in EM Cyg. Any spectra affected by eclipse were not included in the fit. The Doppler image shows a diffuse ring-like emission structure, representing the accretion disc, which if tracking the motion of the white dwarf should be centred at position $(0, -\mathrm{K}_1)$ in velocity space. The inner edge of this ring represents the velocity at the outer edge of the disc, which appears to be at a velocity of $\approx 200\,\mathrm{km\,s^{-1}}$, which is low compared with values of the outer disc velocities of other dwarf novae (e.g. Marsh & Horne, 1990); the dashed circle drawn is again the Keplerian velocity at the outer edge of a Keplerian disc (see section 3.2.5). The apparent 'hole' near the centre-of-mass velocity of the system is due to the third star (see Chapter 3). This was not removed from the original spectra in order to show its relative magnitude and to demonstrate that we can pick up its Hα flux.

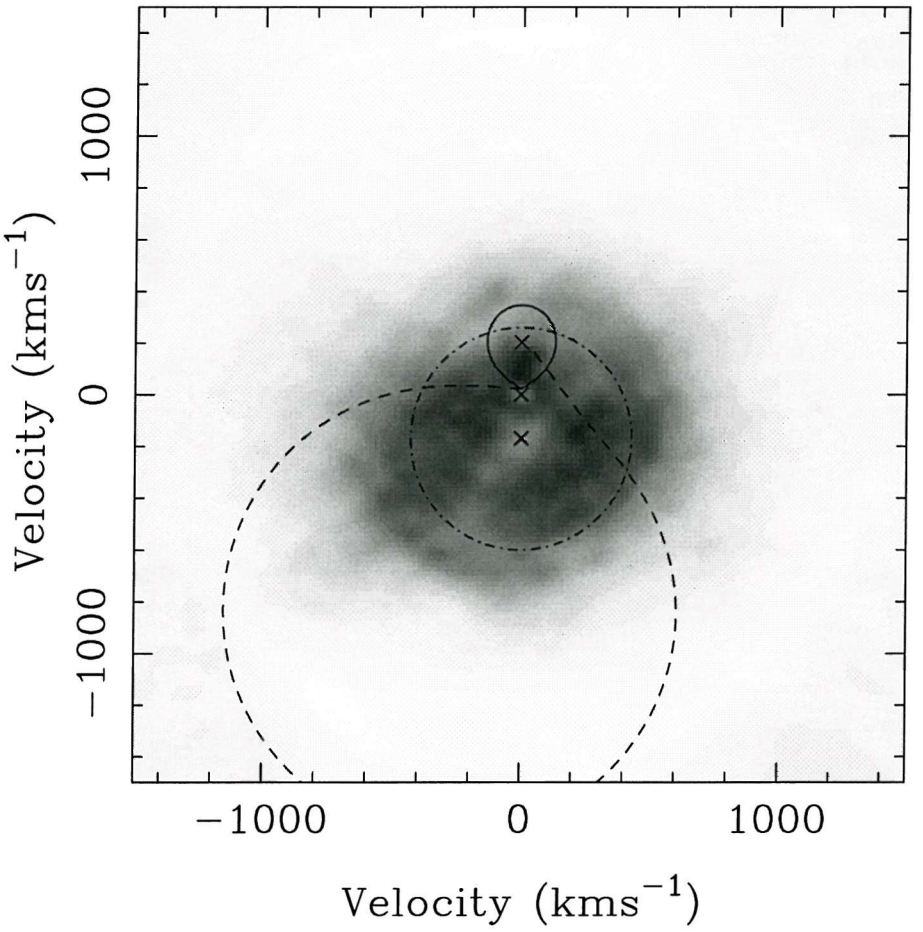

Figure 6.3: Doppler image of the Hα line. Also plotted are the centre of mass of the donor star at $V_y = 202\,\mathrm{km\,s^{-1}}$ (upper cross), the centre of mass of the system (middle cross), and the centre of mass of the white dwarf (lower cross). The Roche lobe of the mass donor star is plotted as well. The dashed line shown is the velocity path of the gas stream. The dash-dotted circle centred on (0,-K_1) is the Keplerian velocity ($430\,\mathrm{km\,s^{-1}}$) at the outer edge of a disc of outer radius $0.8R_{L_1}$.

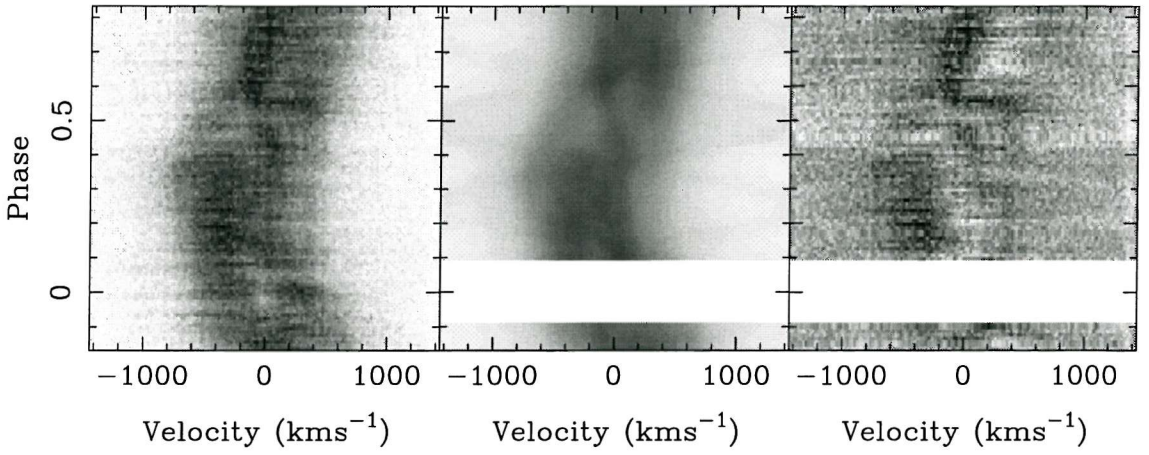

Figure 6.4: Trailed spectra of the Hα emission line. Strong emission is black on this plot. The left-hand panel shows the observed data used to calculate the Doppler tomogram. The middle panel shows the trailed spectrum reconstructed from the tomogram. Finally, the right-hand panel displays the residual image formed when the computed data is subtracted from the observed data.

The trailed spectra in the left-hand panel of Fig. 6.4 shows the set of spectra used to compute the Doppler image. Although there is no obvious sinusoidal emission from the mass donor visible in the trail, there is emission from the irradiated face of the donor visible on the Doppler map (Fig. 6.3). The central panel of Fig. 6.4 shows the data computed from the Hα Doppler map. The large region of emission around phase 0.7 apparent in the actual data, is not completely reconstructed in the predicted data. Finally, the right-hand panel shows the difference between the observed and computed data. Variations in flux from the red and blue sides of the $H\alpha$ line profile are shown the upper and lower panels of Fig. 6.5 respectively. Flux from velocities between 150 km s^{-1} and 600 km s^{-1} from each side of the profile were used to create the plot. This clearly illustrates the eclipse occurring in the blue wing first (bottom panel, marked with an arrow), then appearing in the red wing (as indicated in the top panel).

Figure 6.6 illustrates the asymmetric emission from the Hα line in EM Cyg. This plot was created by calculating the symmetrical emission in the Doppler map, and then subtracting it from the original map. The darker colours imply emission on this plot. There is a large crescent of emission in the upper-right and right-central

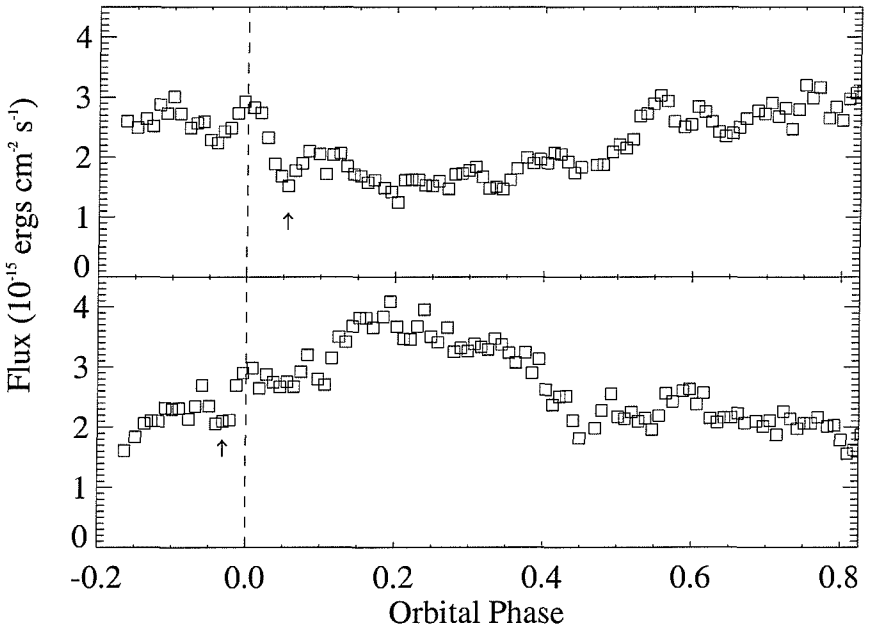

Figure 6.5: Variation of flux from the Hα emission line with orbital phase; 1) The upper plot shows the flux coming from the region between 150 and 600 kms^{-1}, 2) The lower plot shows the flux coming from the velocity region -150 – -600 kms^{-1}. The arrows indicate the eclipses of the approaching (lower plot) and receding (upper plot) limbs of a rotating disc

regions of the figure. There appears to be some emission at the inner Lagrangian point, however this may partly be an artifact from the contribution to Hα by the contaminating star. In addition, there is another crescent-like emission region in the lower-left quadrant of the plot. The crescent regions together appear almost like the characteristics of spiral shocks, which have been detected in dwarf novae during outburst (Steeghs et al., 1997). They may also be consistent with sub-Keplerian velocities. Note that EM Cyg appeared to be on its way down from a standstill state at the time of the observations (see Fig. 3.1).

6.3.2 SS Cygni and AH Herculis

SS Cyg and AH Her were both in quiescence at the time of these observations. SS Cyg appears to have been $\sim$ 10 days before the start of an outburst, whereas AH Her was just at the end of one (Mattei, 2000). In terms of the disc sizes of the

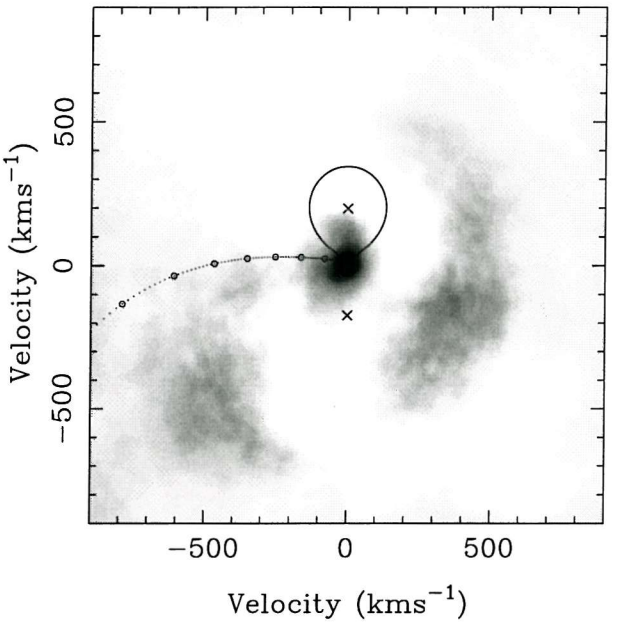

Figure 6.6: The asymmetric emission from EM Cyg. Darker regions indicate emission.

two objects, this means that the disc radius of SS Cyg should have been approaching a minimum, whilst the radius of the disc in AH Her should have been quite large. The Doppler maps of these two objects appear very similar, so will be discussed together. Fig 6.7 shows the Doppler images of left, AH Her and right, SS Cyg. That of SS Cyg (right-hand panel, Fig. 6.7) appears to show some sort of disc-like structure out to around 450 km s^{-1}, which supports the idea of a decreasing disc size because it is a larger velocity than seen in EM Cyg, for example. Emission is also present from the hemisphere of the mass donor facing the white dwarf. However, there is also a tear-drop-shaped region of emission in the bottom-central area of the image, from (~0,-300) to (200,-50) kilometres per second. A similarly shaped area of emission exists in the AH Her map, although it extends from (-300,-50) in the bottom-left quadrant on the image to (50,-300) located in the bottom-central part. A point to note on the AH Her map is that there appears to be no evidence for an annulus of emission – which is the signature of an accretion disc (left-hand panel, Fig. 6.7).

Emission is visible on the side of the mass donor facing the white dwarf in both cases. This S-wave is prominent in the trailed spectrum in column 4, bottom panel

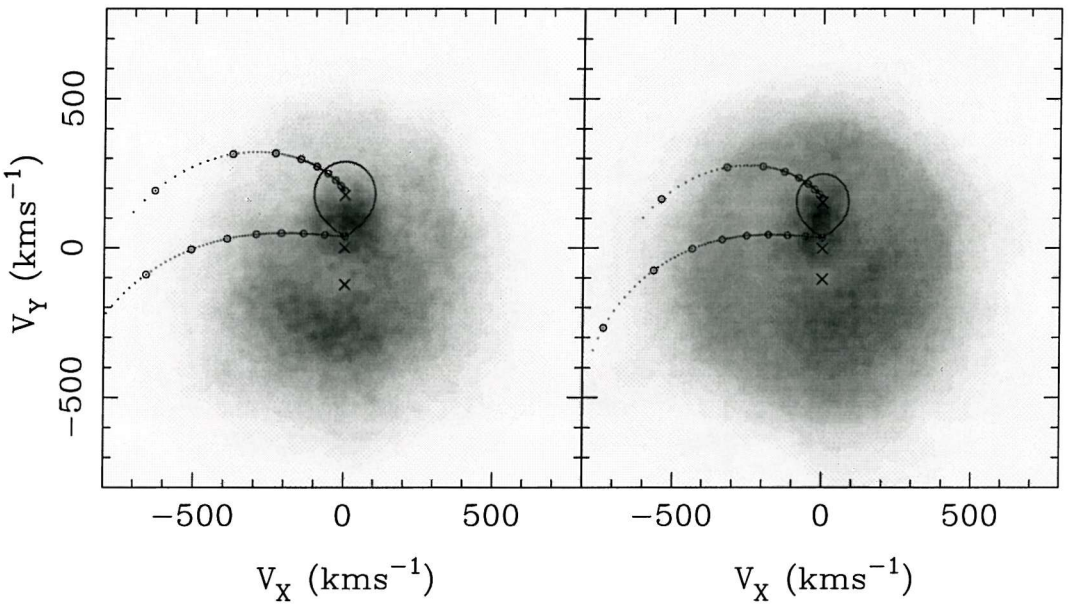

Figure 6.7: Doppler maps of *a*) AH Her, left, and *b*) SS Cyg, right from Hα emission

of Fig. 6.2. In both cases, the emission is enhanced in the trail at phase 0.5, which is what we would expect to see if the white dwarf and boundary layer illuminate the mass donor. The amplitude of these sine waves is $\sim 150\,\mathrm{km\,s^{-1}}$, which supports the suggestion that their origin is on the mass donor.

However, there is also an S-wave component moving in phase with the white dwarf in both of the maps. In both cases. it appears to move with an amplitude of $300-400\,\mathrm{km\,s^{-1}}$. This is more difficult to interpret. Horne (1999) proposes that the *magnetic propeller* theory used to explain AE Aqr could be altered to describe the presence of emission at low velocities in the lower-left quadrant of the Doppler map, which doesn't correspond to a physical position in the binary system. The idea is that even though the gas stream dumps most of its material at the impact with the disc, some of it flows over the edge on ballistic trajectories (Lubow, 1989). As a consequence, interactions between the magnetic-field anchored in the inner accretion disc and the material could occur. Closed loops near to the disc surface pull the matter toward the local Kepler speed encouraging it to impact onto the disc surface. However, the loops higher up are more open, and so drag the gas forward, upward and out of the binary system. Figure 6.8 illustrates what could

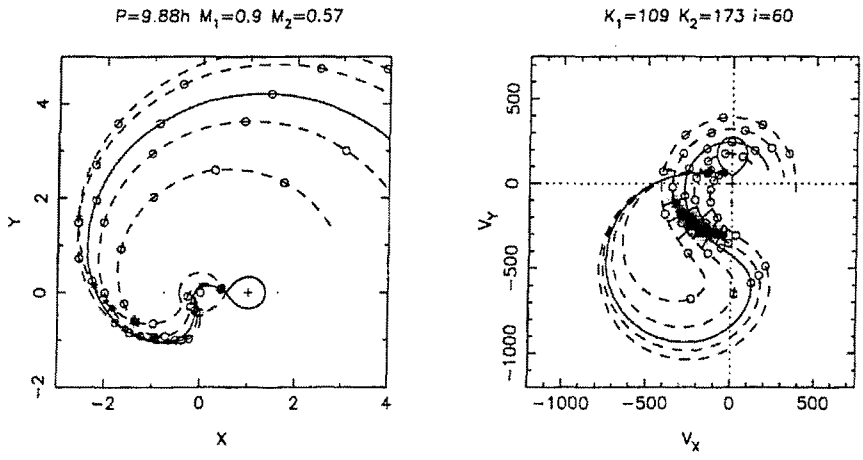

Figure 6.8: Trajectories of diamagnetic blobs interacting with a rapidly spinning white dwarf, as in the case of AE Aqr. The left panel shows them in spatial coordinates, and the right-hand panel is in Doppler coordinates. Open circles show time of flight in units of $0.1P_{\rm orb}$. Asterisks and grey Gaussian patches locate the regions where the blobs collide and produce fireballs. *From Horne (1999)*

happen in both spatial and velocity coordinates in the system AE Aqr. The emission which is visible in the lower-left quadrant of the Doppler map is due to the fireballs created because of collisions between blobs of differing sizes and densities in the exit stream. This agrees with the position of the emission in AE Aqr. It also corresponds to the location of emission seen in the Doppler map of AH Her. Whether this theory is physically possible though, is still an open question.

The dashed circles plotted on the Doppler maps of SS Cyg and AH Her in Fig. 6.2 are the Keplerian velocities an the outer edge of an accretion disc with a radius of $0.8R_{L_1}$. This is large for a dwarf nova, and so it should be very unlikely that any emission is located within its circumference on the Doppler maps. This was calculated using equation (1.11), which says

$$v_{kep} \sin i = \sqrt{K_2 \left(K_2 + K_1\right)} \left(\frac{a}{r_d}\right)^{\frac{1}{2}}$$

where v_{kep} is the disc velocity at radius r_d which is expressed in terms of the stellar separation within the binary star, a, with K_1 and K_2 being the amplitude of the motion of the white dwarf and mass donor respectively. As can be seen, all of the

emission due to the second S-wave in the plot appears within the marked circles, indicating that it is sub-Keplerian. So, either this emission is not from the accretion disc, or the gas at the outer-edge of the disc, where emission occurs, is travelling at sub-Keplerian velocities. There is no immediate explanation for why this is so. For SS Cyg and AH Her, the best explanation for the two sine waves seen in the trailed spectra is that one originates at the mass donor, and the other is due to some kind of interaction above the plane of the disc. Figure 6.9 shows the asymmetric

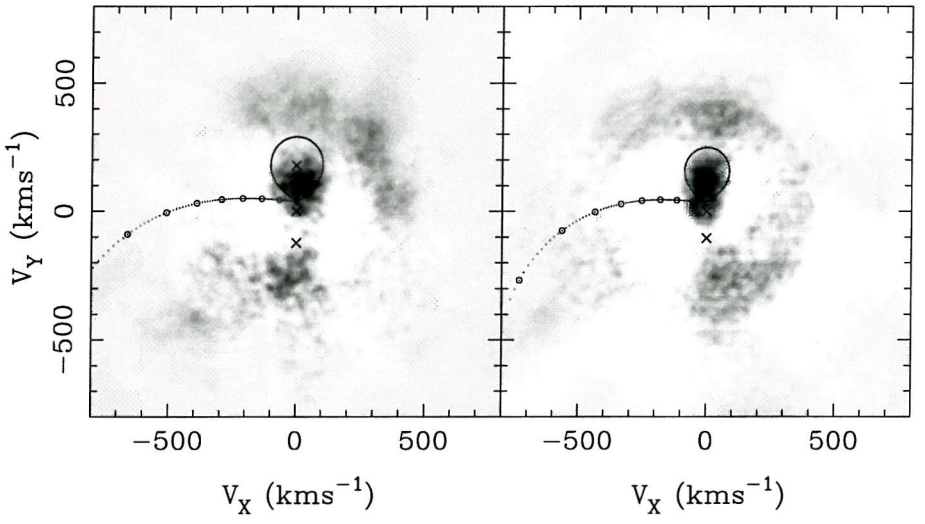

Figure 6.9: Asymmetric emission from a) AH Her, left and b) SS Cyg, right

components of Hα emission from AH Her, left-hand panel, and SS Cyg, right-hand panel. The areas of emission from the lower-central portion of the Doppler images for each object are apparent, less so for SS Cyg, but obvious for AH Her. The emission on the hemisphere of the mass donor facing the white dwarf is also present. There is also a partial annulus appearing above the velocity of the mass donor in the AH Her map, and to some extent also in the SS Cyg plot. Finally, Fig. 6.10 shows the Doppler map constructed from the Ca II near-IR triplet with data from over half an orbital period (see Chapter 2). It is dramatically different from that of Hα, with the annulus from an accretion disc being particularly prominent. The outer edge of the disc appears to have velocities around $\sim 350\,\mathrm{km\,s^{-1}}$. Oddly, there is no emission from the mass donor, which we would expect to see from a late-type star with chromospheric activity.

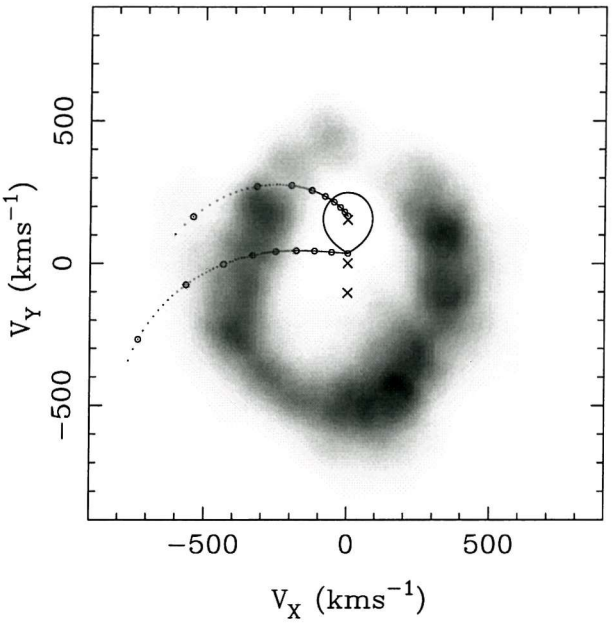

Figure 6.10: Doppler map from the Ca II lines of SS Cyg

6.3.3 V426 Ophiuchi

V426 Oph is classified as a dwarf nova of the Z Cam sub-type (Ritter and Kolb, 1998). However, the 1980s and early 1990s saw questions arise as to whether V426 Oph was actually a magnetic CV – an intermediate polar (Szkody, 1986) – because of the amplitude and shape of a one-hour modulation seen in the X-ray data. Hessman (1988) concluded that V426 Oph was a dwarf nova of the Z Cam sub-type. Szkody & Mateo (1988) conclude that the presence of a UV lag with respect to the optical (visible in dwarf novae during the rise to outburst) further strengthens this argument, but suggested that further X-ray data from the object in a quiescent state should be obtained. Hellier et al. (1990) disagree completely with the intermediate polar designation, having found no evidence for any optical modulation.

Column 2 of Fig. 6.2 shows the Doppler map and related data for V426 Oph. Starting with the trailed spectrum (bottom panel) the first thing which is immediately obvious is the enhanced absorption on the blue wing of the line leading up to phase 0.5. This is consistent with the behaviour of a group of nova-like stars,

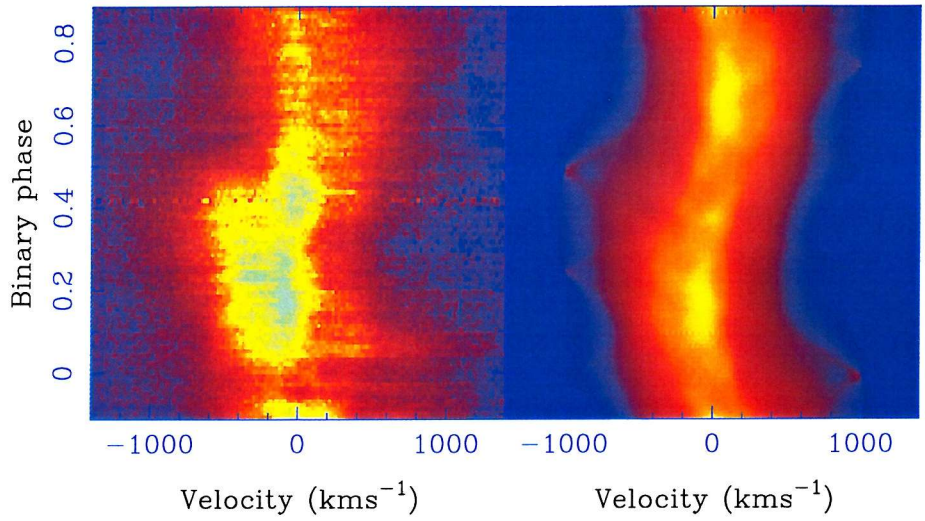

Figure 6.11: Trailed spectra of a) V426 Oph as observed (left), and b) the predicted data from the Doppler map (right)

the SW Sex systems (see section 1.2). Their spectra show a high-velocity S-wave which produces a prominent red wing to the line at phase 0, and a prominent blue wing at phase 0.5. They also show single-peaked emission lines, with shallow Balmer-line eclipses and absorption at phase 0.5. Several theories exist as to the reason for the 'SW Sex syndrome'. There have been suggestions of an accretion disc wind (Williams, 1989), and Stark broadening (Lin et al., 1988). Hellier & Robinson (1994) propose that the asymmetric emission is a result of the gas-stream overflowing the impact site at the accretion disc edge, and carrying on in a ballistic trajectory until it impacts the disc at a later point (Lubow, 1989). Emission from this point would produce a red wing at phase 0.8, and a blue wing at phase 0.3. This interpretation seems to fit the data for V426 Oph. Figure 6.11 shows the trailed spectra for V426 Oph, and there does appear to be a slightly enhanced red emission-wing around phase 0.8. However, the blue wing of the line doesn't appear until phase 0.4–0.5. It is interesting to note that the predicted data has real trouble fitting the observed data. In the observed data is a slightly sinusoidal curve of emission at very low velocities. This manifests itself in the Doppler map as a horseshoe-shaped region of emission at very low velocities, between the inner Lagrangian point and the white dwarf velocities. Steeghs et al. (1996) speculate

that 'slingshot prominences' (Collier Cameron and Woods, 1992) could be a possible interpretation of the low velocity emission, which they similarly saw in several emission lines in SS Cyg and IP Peg whilst both systems were in outburst. They propose that regions where extended magnetic loops are stable in binary stars do exist, and that the area between the inner Lagrangian point and the white dwarf in CVs is one of them. Should the mass donor have an active spot, then a magnetic loop could extend past the Roche lobe and be pulled towards the white dwarf which would cause the structure to expand. Plasma flowing along field lines to the top of the loop would then be confined by the magnetic tension of the loop in a position where it would be illuminated by both the accretion disc and the face of the mass donor. This would result in an emission source rotating with, but separated from the mass donor. The potential field of a close binary star creates a special geometry where material is only loosely-bound near the inner face of the mass donor, and the effective potential decreases as the white dwarf is approached. Therefore prominences are more likely to form at this point in a close binary (in single stars, prominences can probably form anywhere on the star) (Collier Cameron, 1999).

An estimate of the size of the emission source in V426 Oph can be made. A measurement of the velocity-width of the emission can be used to obtain an upper limit to the emission-source size. Isolating the emission due to the source at the L_1 point, and fitting a Gaussian to that emission peak resulted in a value of the velocity-width, $\Delta V = 43\,\mathrm{km\,s^{-1}}$. Using

$$\frac{\Delta V}{K_1 + K_2} = \frac{l}{a} \tag{6.3}$$

and assuming that the prominence is rotating with the mass donor, then an upper limit for the size of the emitting region of $0.14a$ is obtained. Equation 1.1 can be used to determine the length of a, with $P_{\mathrm{orb}} = 0^{\mathrm{d}}.285$ and $\mathrm{M_1}$ from section 4.5, which determines the size of the emitting region to be less than 2×10^{10} cm. Steeghs et al. (1996) calculated an estimate of 10^{10} cm for SS Cyg.

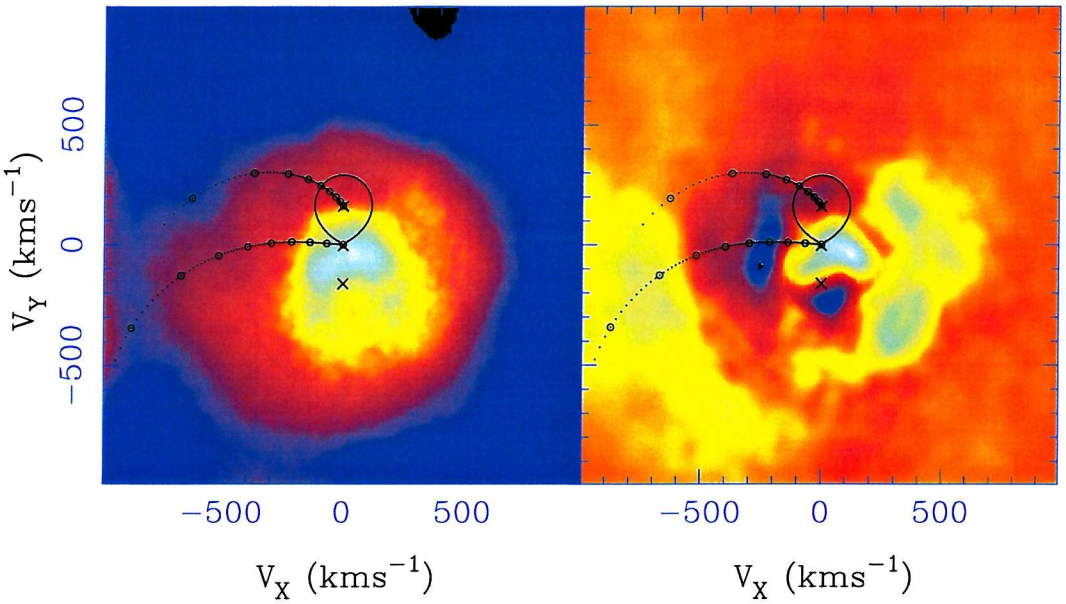

Figure 6.12: An indication of possible stream overflow in V426 Oph?

The left-hand panel of Fig. 6.12 is included to highlight the emission at high velocities in the centre-left quadrant of the map which could be attributable to stream overflow. When the gas stream leaves the inner Lagrangian point and impacts onto the side of the disc, depending on the conditions at the edge of the disc, some material may flow over and under the disc-edges and continue on its ballistic trajectory until it impacts the disc at a later time. It is at the re-impact with the disc that emission at high velocities is expected to be seen. The right-hand panel of Fig. 6.12 is included here to highlight this potential region of stream overflow. The emission extends out to velocities of $\sim 950\,\mathrm{km\,s^{-1}}$, corresponding to a position $0.2R_{L_1}$ from the white dwarf. This emission could be that from the re-impact of the gas-stream with the disc.

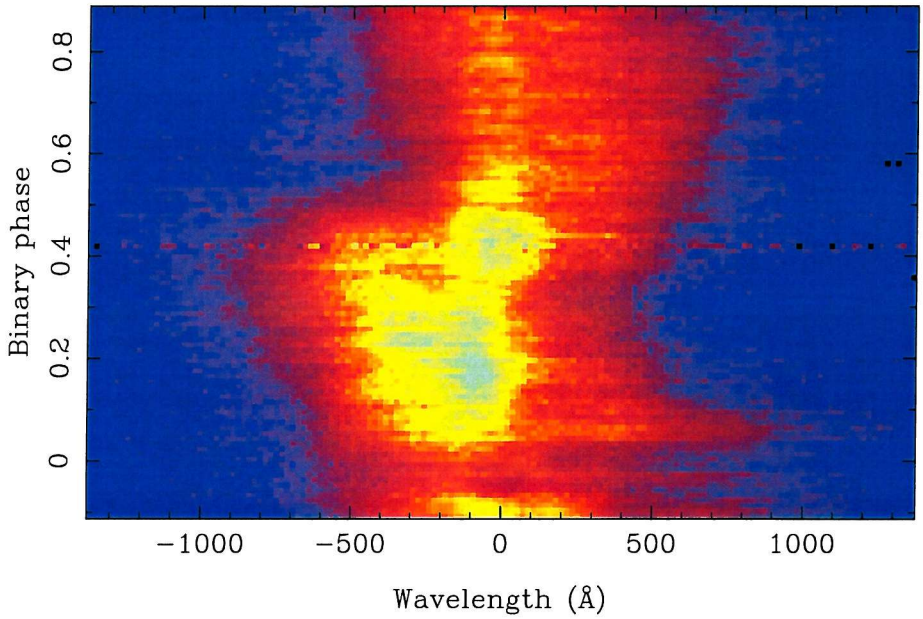

Figure 6.13: Trailed spectra of V426 Oph showing the apparent eclipse in Hα

6.3.4 Possible eclipse in Hα

Although V426 Oph is not classified as an eclipsing system in the catalogue of Ritter & Kolb (1998) the trailed spectra centred on the Hα line (Fig. 6.13) appear to reveal the presence of an eclipse.

The emission source appearing at the core of the line profile (see section 6.3.3) does appear to be affected when the Hα disc-emission is eclipsed. This implies that the source of this line-centre emission is in the same physical region as that contributing the disc emission. If the source of the Hα emission is located in the plane above the disc, then we might see an eclipse in this emission line, but not in higher excitation lines (such as He II, which originate in the plane of the disc, towards its central regions). The inclination in V426 Oph has been measured at 59$\pm$6° (Ritter and Kolb, 1998). Figure 6.14 illustrates how an eclipse in Hα might be possible without an eclipse in the disc continuum. Further observations are needed to confirm the presence of an eclipse, and if this is the case, then accurate system parameters can be deduced from a combination of photometry and spectroscopy.

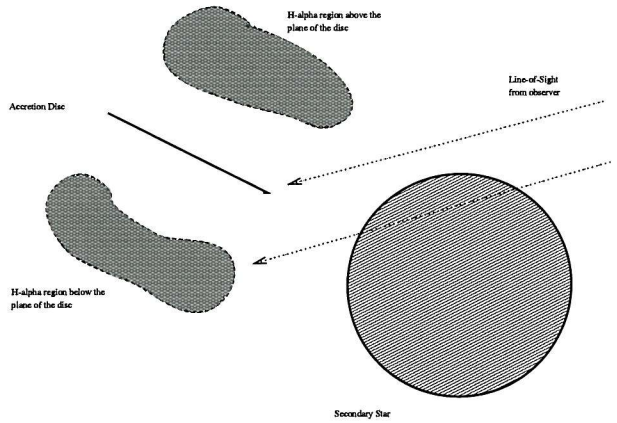

Figure 6.14: Clouds of Hα emission above the plane of the disc

6.4 Conclusions

To summarise, four Hα Doppler maps have been presented, none showing the classic 'Doppler map traits' of a ring-like emission structure (due to a rotating accretion disc) and bright spot (emission from the point where the gas-stream impacts the disc edge); instead each one appears to show emission from the hemisphere of the mass donor facing the white dwarf. Two of the systems, AH Her and SS Cyg, have a second S-wave present in the trailed spectra which is phased with the white dwarf. V426 Oph shows characteristics similar to the SW Sex class of Nova-like variable stars, and it's Doppler map has a very high velocity emission component in the region where theoretical stream overflow re-impact emission would be expected. In addition, the Hα emission appears to be eclipsed around phase 0, a feature which hasn't been noticed in this object before. EM Cyg shows the most 'classic' Doppler map, with evidence for an accretion disc, although here again, as with all the other systems emission is present at apparently sub-Keplerian velocities. These characteristics appear to be peculiar to Hα, as Doppler maps of other Balmer series members do not appear to behave in such an erratic manner, tending to show emis-

sion where expected (Marsh, 2001). Many other objects, however, show low velocity emission (Marsh, 2001) as do all the maps here. In addition, the question has to be asked, do the Doppler maps of these objects look the same in other ionization species, or do they behave in a more predictable manner? This question needs investigating.

Chapter 7

Conclusions and future work

Accurate binary star system parameters are important because they contribute to the knowledge of both stellar masses and binary evolution. However, there are still discrepancies in the literature which prevent a complete survey of CV masses being completed. In particular, the methods being used to derive the parameters are not uniform in the sense that different research groups prefer to use different techniques, which themselves introduce different forms of systematic error. In this thesis I have entered this domain, in order to measure particular system parameters to compare with theory, and I have used several methods to measure parameters for a particular type of interacting binary system, the Cataclysmic Variable stars. There is still a lot of work to be done, mainly in compiling the results, many of which do not appear to be published, and re-analysing data sets if need be, to determine other useful parameters which were not required for the aims of the original research. Advances in spectral line formation theory will enable a more informed choice of which spectral lines to use for accretion-disc velocity measurements, and perhaps take a step towards solving the problems associated with mass-determinations of the mass-losing stars in CVs which are made from these lines. This chapter concludes the thesis by providing a review of each chapter, and then gives a further insight into the work which still needs to be done with these data.

7.1 The dwarf nova EM Cygni

Chapter 3 described the results obtained for the dwarf nova EM Cygni. EM Cyg was once a puzzle to CV researchers as it was in a very small group of objects in which the mass donor was observed to be more massive than the white dwarf, a situation which given the current theory should lead to dynamically unstable mass transfer, and so should not exist. The better resolution of our observations solved this mystery: there was an additional absorption line spectrum present, which revealed itself via a narrow absorption line spectrum. The mass donor in EM Cyg should have had absorption lines which were rotationally broadened, to a value in the region of $100\,\mathrm{km\,s^{-1}}$. The narrow absorption lines obviously weren't. Once the additional ('contaminating') absorption lines were removed from the spectrum, and the cross-correlation analysis carried out on the data, a new value for the radial velocity amplitude of the mass donor in EM Cyg was deduced. The analysis produced a value of $202 \pm 3\ \mathrm{km\,s^{-1}}$, an increase of over sixty kilometres per second as compared to Stover et al.'s (1981) value of $135 \pm 3\ \mathrm{km\,s^{-1}}$. This immediately removed the problem. The mass ratio, q, shrinks down to $q = 0.84$ using this and the K_1 value from observations of the emission lines. Due to the inherent errors in obtaining K_1, however, an alternative method to calculate the mass ratio q, using a measurement of the rotational broadening of the mass donor absorption lines is favoured here. This resulted in a slightly revised value of $q = 0.88 \pm 0.05$. Once the presence of a third star was realised, high resolution echelle spectra were taken in order to detect its radial velocity variations. Further observations need to be taken however, as the current baseline is only a few weeks.

7.1.1 Future work

An application has been accepted to use the Fine Guidance Sensor (FGS) on the Hubble Space Telescope (HST) to try and resolve the binary from the third star. At

a distance of 300 pc the ground-based imaging indicates a separation smaller than 60 A.U. This is not a strong constraint upon the prior evolution of the CV. With HST+FGS this limit can be reduced to 6 A.U.; the ground-based radial-velocity measurements are then sensitive to separations below this. This will enable the entire possible range of separations to be covered and so an upper limit to the size of the progenitor to the CV can be deduced. Therefore, a combination of continued echelle observations (to obtain good radial velocities) and HST+FGS observations will complete a thorough analysis of EM Cygni, and deduce definitively whether it is only the second CV known to be in a triple system.

7.2 Systemic velocities of long-period dwarf novae

Four long period ($P_{orb} > 5$ hours) dwarf novae have been observed over one complete orbital period, in order to determine accurate systemic velocities for these objects. On this initial sample, the aim was to test thoroughly the methods being used to obtain the velocities, and to make sure that effective minimisation of any possible sources of systematic error occurred. Sources of systematic error are fairly numerous using these methods, however they are very easy to identify and minimise, and in certain cases, to eliminate altogether. A large sample of radial-velocity standard stars were observed, to ensure that so-called 'template mismatch' did not introduce any significant error. This enabled us to compile a list of reliable standard stars to use for future observing runs with the same astronomical aim and instrumental set-up. In addition, because of the high accuracy requirement for measurement of the systemic velocities, accurate measurements of other binary parameters can be made. High quality radial-velocity curves mean that good K amplitude measurements can be obtained. Existing orbital periods can also be checked, and values for the projected rotational velocity of the mass donors can be determined, which

allow a determination of the mass ratio, q. This value of q is then independent of the radial-velocity amplitude value determined from emission lines (measurements of which are uncertain and prone to error), and can then be used to determine the component masses.

Our initial results suggest that the observations agree with theory (as set out by Kolb & Stehle, (1996)). The observed velocity dispersion for the sample is $\sim 8\,\mathrm{km\,s^{-1}}$, which is a little smaller than the predicted value of $15\,\mathrm{km\,s^{-1}}$. If, with further observations, this value does not alter significantly, then we can infer that the distribution of CVs does correlate with age, provided that measurements are also made to obtain the velocity dispersion of the short-period systems too. The longer period systems are a younger subgroup, with an average predicted age of ≤ 1.5Gyrs. Further measurements of the systemic velocities of more longer period dwarf novae are necessary. However, once these have been constrained then our understanding of the kinematics and evolution of the longer-period dwarf novae will be much more complete.

7.2.1 Future work

Now a statistically significant collection of γ–velocities need to be compiled in order to directly test the magnetic braking theory. This may require use of archival data, although an initial search tends to indicate that the data are not well-sampled enough, or indeed covering a great enough fraction of the orbital period to get a reliable γ–velocity measurement. This project will therefore require further applications for telescope time if it is to be completed successfully. However, the benefits to the CV community of completing this research are obvious. In addition to the theory testing which is itself an important point to establish, many more accurate compact object masses will be determined, as will accurate mass ratios and possibly disc peak measurements (which will help to complete Chapter 5).

7.3 Radii of accretion discs in dwarf novae and soft X-ray transients

Measurements of the separation of the double peaks in the emission lines from accretion discs in dwarf novae and soft X-ray transients have been collated from the literature, in order to determine whether the observations insinuate that the discs are larger than would be expected in quiescence (from theoretical constraints) in these systems. Radial velocity amplitudes of mass donors in the same objects were also tabulated, to use in a ratio with the disc velocities in order to remove the $\sin i$ dependence which prevents many direct comparisons being made between observations and theory. Many recent publications advocate the existence of sub-Keplerian velocities in the discs of these objects. These imply that the discs are close to, or even apparently larger than, the size allowed by tidal limitations. The most likely cause of this effect is that the emission lines are intrinsically broad. Many comparisons have been made between dwarf novae and soft X-ray transients, with the larger output of X-rays from the latter being invoked to explain their longer recurrence times. Failure to find small discs in soft X-ray transients in addition poses the question as to whether the models which describe the outbursts in these systems with a large fraction of the disc mass being accreted are correct. In particular, this questions the validity of the irradiated disc model (King and Ritter, 1998) which was created to explain the light curve behaviour of these systems after outbursts.

Several peak separation measurements were made with data collected covering the Ca II triplet around 8500Å of a selection of dwarf novae. Ca II lines are assumed to form closer to the outer disc edge than the hydrogen lines, and so are thought to be a better indicator of the actual disc size (Persson, 1988). However, whilst looking for systems in quiescence, several exposures were obtained of systems in an outbursting state, which all appeared to have something in common. A narrow 'spike' of emission, apparently following the orbital motion mass donor, was visible

in most of the outbursting dwarf novae. All three of the Ca II lines showed this 'spike' if it was present. Measurements of the radial velocities of the spikes, and their motions over the two exposure times (usually of the order 40 minutes or so), indicated that their origins do lie with the mass donor. If these are in fact visible in all dwarf novae in outburst, then it presents a sensitive new way to detect the mass donors in CVs, and therefore obtain mass estimates for the compact objects; it will be especially useful for those whose mass donors are not visible in the optical spectrum. After the calcium emission was noticed, an application was made to measure the spikes in some dwarf novae, however the observing run was plagued by bad weather, and so no useful new results were obtained.

7.3.1 Future work

As further papers are published, then more data can be collected and a more complete plot created. Ideally, peak separations would be determined from Ca II measurements (as these are assumed to come from the outermost parts of the disc, thereby more accurately reflecting the disc size), however at the present time there are not many measurements of this type available. An extension to the study of Ca II spikes would benefit this work, as more radial velocity curves for mass donors in CVs could be obtained. In general, Doppler mapping the Ca II lines will determine beyond doubt the origin of the majority of the emission in these lines.

7.4 Doppler imaging of long-period dwarf novae

From this thesis, the major deduction that can be made regarding the Doppler maps is that the Hα line appears to behave in a very different way to that which is expected for emission lines in CVs. Is this due solely to the processes which cause the formation of Hα and why do they differ from those which form the higher

members of the Balmer series? Very little disc emission appears in the Hα line of the observed objects in quiescence, or at least if the disc emission is there, it is not looking like a typical annulus of emission which would expect to be seen (e.g. SS Cyg, EM Cyg). EM Cyg was caught on the way down from a standstill period. The disc emission in this object almost looks as would be expected from spiral shocks in the disc (Steeghs et al., 1997), although at sub-Keplerian velocities. These are not expected to be readily observable in quiescence, due to them being wound up rather tightly due to the prevailing Mach number in the disc at the time. However, if the standstill was just coming to an end, then the disc state might be such that the observations show the shocks dissipating. More evidence for sub-Keplerian velocities has been uncovered with this research. All four of the observed dwarf novae appear to have emission at very low velocities. The site of this emission needs to be deduced; however Doppler maps may not be the solution here. For example, if this emission were from out of the orbital plane of the accretion disc, then a Doppler image would not be able to tell us that. Several theories have been put forward to explain the emission seen in AH Her and SS Cyg. These need to be further explored, both observationally and theoretically.

7.4.1 Future work

More Doppler maps both in different elements and different ionization states need to be calculated for the longer-period dwarf novae in quiescence to create a more complete picture of the behaviour of these objects. Comparisons of maps in different lines of the same species should be compared to aid the understanding of line formation in CVs. Is Hα peculiar, in that Doppler broadening is not the dominant mechanism forming the emission line? How does this line compare to other Balmer lines in these objects, and indeed to other species (especially those in which the electron arrangement is similar to H I) and how can we develop Doppler maps in order to extract the maximum information possible? Finally, the question needs to

be answered, what exactly is the nature of V426 Oph?

Appendix A

Double-lined spectroscopic binaries

Table A.1: List of double-lined CVs in order of Right Ascension. Taken from the catalogue of Ritter & Kolb (1998)

Object	α^a (J2000)	δ^b (J2000)	V mag	Orbital Period (hours)	Type^d
WW Cet	00 11 24.7	-11 28 44	13.0	4.2	DN
GK Per	03 31 11.8	+43 54 17	10.2	47.9	Na DN IP
V363 Aur	05 33 33.4	+36 59 32	14.2	7.7	NL UX
CN Ori	05 52 07.7	-05 25 00	14.2	3.9	DN UG
SS Aur	06 13 22.4	+47 44 26	14.5	4.4	DN UG
V616 Mon	06 22 44.4	-00 20 45	17.9	7.8	XT BH
CW Mon	06 36 54.6	+00 02 15	16.3	4.2	DN UG
U Gem	07 55 05.3	+22 00 06	14.0	4.2	DN UG
Z Cha	08 07 28.6	-76 32 02	15.3	1.8	DN SU
IX Vel	08 15 19.1	-49 13 21	9.1	4.7	NL UX
Z Cam	08 25 13.2	+73 06 40	13.6	7.0	DN ZC
AC Cnc	08 44 27.2	+12 52 32	13.8	7.2	NL UX
CH UMa	10 07 00.7	+67 32 47	15.3	8.2	DN UG
RW Sex	10 19 56.6	-08 41 56	10.4	5.9	NL UX

continued.....

continued from previous page..

Object	α^a (J2000)	δ^b (J2000)	V mag	Orbital Period (hours)	Type
GU Mus	11 26 26.6	-68 40 32	20.4	10.4	XT BH
TT Crt	11 34 47.3	-11 45 31	15.9	7.3	DN
DO Dra	11 43 38.5	+71 41 19	15.6B	4.0	NL IP
WX Cen	13 12 52.5	-63 23 45	13.4	10.0	NL?
BV Cen	13 31 19.6	-54 58 34	12.6	14.6	DN UG
U Sco	16 22 30.7	-17 52 42	17.9	29.5	Nr
AH Her	16 44 09.8	+25 15 01	13.9	6.2	DN ZC
EX Dra	18 04 14.1	+67 54 12	14.5	5.0	DN UG
DQ Her	18 07 30.2	+45 51 32	14.2	4.6	Na DQ
V426 Oph	18 07 51.8	+05 51 48	11.5	6.8	DN ZC
V691 CrA	18 25 46.6	-37 06 18	15.8	5.6	DC
BD Pav	18 43 12.0	-57 30 45	15.4	4.3	DN UG
EM Cyg	19 38 40.0	+30 30 27	13.3	7.0	DN ZC
V Sge	20 20 14.8	+21 06 08	12.2	12.3	NL
AE Aqr	20 40 09.1	-00 52 16	10.7	9.9	NL DQ
SS Cyg	21 42 42.5	+43 35 10	11.4	6.6	DN UG
RU Peg	22 14 02.5	+12 42 11	12.6	9.0	DN UG
IP Peg	23 23 08.7	+18 24 59	14.0	3.8	DN UG
DX And	23 29 46.7	+43 45 05	16.5	10.6	DN UG
HX Peg	23 40 23.8	+12 37 41	12.9	4.8	DN

[a] Right Ascension; [b] Declination; [c] from Ritter & Kolb (1998)

[d] From Ritter & Kolb, 1998; DN - dwarf nova; UG - U Gem subtype; ZC - Z Cam subtype; SU - SU UMa subtype; Na - Nova; Nr - Nova remnant; NL - Nova-like; DQ - DQ Her subtype; IP - intermediate polar; UX - UX UMa subclass; XT BH - Black Hole X-ray transient;

Bibliography

Allen, C. W.: 1973, *Astrophysical Quantities*, Athlone Press, London, 3rd edition

Baptista, R., Cataln, M. S., and Costa, L.: 2000, *Mon. Not. R. Astron. Soc.* **316**, 529

Barnes, T., Moffett, T. J., and Slovak, M. H.: 1986, *Publ. Astron. Soc. Pac.* **98**, 223

Barrera, L. H. and Vogt, N.: 1989, *Astron. Astrophys.* **220**, 99

Barwig, H. and Schoembs, R.: 1983, *Astron. Astrophys.* **124**, 287

Bath, G.: 1969, *Astrophys. J.* **158**, 571

Bath, G.: 1972, *Astrophys. J.* **173**, 121

Bath, G.: 1975, *Mon. Not. R. Astron. Soc.* **171**, 311

Beavers, W. I. and Eitter, J. J.: 1986, *ApJS* **62**, 250

Beavers, W. I. and Eitter, J. J. a.: 1979, *Publ. Astron. Soc. Pac.* **91**, 698

Beuermann, K., Baraffe, I., Kolb, U., and Weichold, M.: 1998, *Astron. Astrophys.* **339**, 518

Beuermann, K. and Pakull, M. W.: 1984, *ApJS* **62**, 147

Billington, I., Marsh, T. R., and Dhillon, V. S.: 1996, *Mon. Not. R. Astron. Soc.* **278**, 673

Brady, R. A. and Herczeg, T. J.: 1977, *Publ. Astron. Soc. Pac.* **89**, 71

Bruch, A.: 1989, *Astron. Astrophys. Suppl. Ser.* **78**, 145

Bruch, A., Vrielmann, S., Hessman, F. V., Kochsiek, A., and Schimpe, T.: 1997, *Astron. Astrophys.* **327**, 1107

Burbidge, E. M. and Burbidge, G. R.: 1953, *Astrophys. J.* **118**, 349

Cannizzo, J. K.: 1993, *Accretion Disks in Compact Stellar Systems*, p. 6, World Sci. Pub. Co., Singapore

Carter, D. and Bridges, T.: 1995, *WHT Prime Focus and Auxiliary Port Imaging Manual*, http://www.ing.iac.es/~manuals/man_wht.html

Casares, J. and Charles, P. A.: 1992, *Mon. Not. R. Astron. Soc.* **255**, 7

Casares, J. and Charles, P. A.: 1994, *Mon. Not. R. Astron. Soc.* **271**, L5

Casares, J., Charles, P. A., and Marsh, T. R.: 1995, *Mon. Not. R. Astron. Soc.* **277**, L45

Casares, J., Charles, P. A., and Naylor, T. A.: 1992, *Nature* **355**, 614

Casares, J., Charles, P. A., Naylor, T. A., and Pavlenko, E. P.: 1993, *Mon. Not. R. Astron. Soc.* **265**, 834

Casares, J., Martin, E. L., Charles, P. A., Molaro, P., and Rebolo, R.: 1997, *NewA* **1**, 299

Casares, J., Martinez-Pais, I. G., Marsh, T. R., Charles, P. A., and Lazaro, C.: 1996, *Mon. Not. R. Astron. Soc.* **278**, 219

Chandrasekhar, S.: 1939, *An Introduction to the Study of Stellar Structure*, University of Chicago Press, Chicago

Clarke, J. T. and Bowyer, S.: 1984, *Astron. Astrophys.* **140**, 345

Clayton, M. J.: 1996, *Echelle Data Reduction Cookbook*, STARLINK Cookbook, 3.1 edition

Collier Cameron, A.: 1999, in C. J. Butler and J. G. Doyle (eds.), *Solar and Stellar Activity: Similarities and Differences*, No. 158 in A.S.P. Conference Series, p. 146

Collier Cameron, A. and Woods, J. A.: 1992, *Mon. Not. R. Astron. Soc.* **258**, 360

Cook, M. C. and Warner, B.: 1984, *Mon. Not. R. Astron. Soc.* **207**, 702

Crampton, D., Fisher, W. A., and Cowley, A. P.: 1986, *Astrophys. J.* **300**, 788

Davey, S. and Smith, R. C.: 1992, *Mon. Not. R. Astron. Soc.* **257**, 476

de Kool, M.: 1992, *Astron. Astrophys.* **261**, 188

Della Valle, M., Masetti, N., and Bianchini, A.: 1998, *Astron. Astrophys.* **329**, 606

Dickenson, R. J., Prinja, R. K., Rosen, S. R., King, A. R., Hellier, C., and Horne,

K.: 1997, *Mon. Not. R. Astron. Soc.* **286**, 44

Drew, J. E., Jones, D. H. P., and Woods, J. A.: 1993, *Mon. Not. R. Astron. Soc.* **260**, 803

Duqennoy, A., Mayor, M., and Halbwachs, J. L.: 1991, *Astron. Astrophys. Suppl. Ser.* **88**, 281

Echevarria, J., Diego, F., Tapia, M., Costero, R., Ruiz, E., Salas, L., Gutierrez, L., and Enriquez, R.: 1989, *Mon. Not. R. Astron. Soc.* **240**, 975

Eggen, O. J.: 1992, *Mon. Not. R. Astron. Soc.* **257**, 476

Eggleton, P.: 1983, *Astrophys. J.* **268**, 368

Eggleton, P., Bailyn, C. D., and Tout, C. A.: 1989, *Astrophys. J.* **345**, 489

Eggleton, P. and Kiseleva, L.: 1995, *Astrophys. J.* **455**, 640

Fiedler, H., Barwig, H., and Mantel, K. H.: 1997, *Astron. Astrophys.* **327**, 173

Fillipenko, A. V., Matheson, T., and Barth, A. J.: 1995, *Astrophys. J.* **455**, L139

Fillipenko, A. V., Matheson, T., Leonard, D. C., Barth, A. J., and van Dyck, S. D.: 1997, *Publ. Astron. Soc. Pac.* **109**, 461

Flannery, B. P.: 1975, *Mon. Not. R. Astron. Soc.* **170**, 325

Frank, J., King, A. R., and Raine, D. J.: 1985, *Accretion Power in Astrophysics*, Cambridge University Press, Cambridge

Friend, M. T., Martin, J. S., Connon Smith, R., and Jones, D. H. P.: 1990a, *Mon. Not. R. Astron. Soc.* **246**, 637

Friend, M. T., Martin, J. S., Smith, R. C., and Jones, D. H. P.: 1990b, *Mon. Not. R. Astron. Soc.* **246**, 654

Froning, C., Robinson, E. L., Welsh, W. F., and Wood, J. H.: 1999, *Astrophys. J.* **523**, 399

Garlick, M. A., Mittaz, J. P. D., Rosen, S. R., and Mason, K. O.: 1994, *Mon. Not. R. Astron. Soc.* **269**, 517

Gilliland, R. L.: 1982, *Astrophys. J.* **263**, 302

Goldader, J. D. and Garnavich, P.: 1989, *Inf. Bull. Variable Stars* **3361**, 1

Gotthelf, E., Halpern, J. P., Patterson, J., and Rich, R. M.: 1992, *Astron. J.* **103**, 219

Greenstein, J. L. and Kraft, R. P.: 1994, *Astrophys. J.* **130**, 99

Harlaftis, E. T., Collier, S., Horne, K., and Fillipenko, A. V.: 1999, *Astron. Astrophys.* **341**, 491

Harlaftis, E. T., Horne, K., and Fillipenko, A. V.: 1996, *Publ. Astron. Soc. Pac.* **108**, 762

Harlaftis, E. T., Steeghs, D., Horne, K., and Fillipenko, A. V.: 1997, *Astron. J.* **114**, 117

Haswell, C. A. and Shafter, A. W.: 1990, *Astrophys. J.* **359**, L47

Hellier, C.: 1996, *Astrophys. J.* **471**, 949

Hellier, C., O'Donoghue, D., Buckley, D. A. H., and Norton, A.: 1990, *Mon. Not. R. Astron. Soc.* **242**, P32

Hellier, C. and Robinson, E. L.: 1994, *Astrophys. J., Lett.* **431**, 107

Hessman, F. V.: 1988, *Astron. Astrophys. Suppl. Ser.* **72**, 515

Hessman, F. V.: 1989, *Astron. J.* **98**, 675

Hessman, F. V. and Hopp, U.: 1990, *Astron. Astrophys.* **228**, 387

Hessman, F. V., Robinson, E. L., Nather, R. E., and Zhang, E.-H.: 1984, *Astrophys. J.* **286**, 747

Hoffmeister, C.: 1928, *Astron. Nachr.* **233**, 5571

Honeycutt, ., Kaitchuck, R., and Schlegel, E.: 1987, *Astrophys. J., Suppl. Ser.* **65**, 451

Horne, K.: 1986, *Publ. Astron. Soc. Pac.* **98**, 609

Horne, K.: 1999, in C. Hellier and K. Mukai (eds.), *Proceedings of the Annapolis Workshop on Magnetic Cataclysmic Variables 13-17 July 1998*, Vol. 157 of *A. S. P. Conference Series*, p. 349

Horne, K. and Marsh, T. R.: 1986, *Mon. Not. R. Astron. Soc.* **218**, 761

Horne, K., Wade, R. A., and Szkody, P.: 1986a, *Mon. Not. R. Astron. Soc.* **219**, 791

Horne, K., Wood, J. H., and Stiening, R. F.: 1986b, *Mon. Not. R. Astron. Soc.* **219**, 791

Hoshi, .: 1979, *Prog. Theor. Phys.* **61**, 1307

Hurley, J. R., Pols, O. R., and Tout, C. A.: 2000, *Mon. Not. R. Astron. Soc.* **315**, 543

Hutchings, J. B. and Thomas, B.: 1982, *Publ. Astron. Soc. Pac.* **94**, 102

ING: 2000, http://www.ing.iac.es/, Isaac Newton Group, La Palma

Jameson, R. F., King, A. R., and Sherrington, M. R.: 1981, *Mon. Not. R. Astron. Soc.* **195**, 235

Joergens, V., Mantel, K. H., Barwig, H., Brnbantner, O., and Fiedler, H.: 2000a, *Astron. Astrophys.* **354**, 579

Joergens, V., Spruit, H. C., and Rutten, R. G. M.: 2000b, *Astron. Astrophys.* **356**, L79

Johnson, H. L.: 1966, *Astron. Astrophys. Rev.* **4**, 193

Johnston, H. M., Kulkarni, S. R., and Oke, J. B.: 1989, *Astrophys. J.* **345**, 492

Kaitchuck, R.: 1989, *Publ. Astron. Soc. Pac.* **101**, 1129

Kaitchuck, R., Mansperger, C., and Hantzios, P.: 1988, *Astrophys. J.* **330**, 305

King, A. R.: 1988, *Q. J. R. Astron. Soc.* **29**, 1

King, A. R.: 1998, *Mon. Not. R. Astron. Soc.* **296**, L45

King, A. R. and Ritter, H.: 1998, *Mon. Not. R. Astron. Soc.* **293**, L42

Kiplinger, A. L.: 1979a, *Astron. J.* **84**, 655

Kiplinger, A. L.: 1979b, *Astrophys. J.* **234**, 997

Kolb, U. and Baraffe, I.: 2000, in P. A. Charles, A. R. King, and D. R. O'Donoghue (eds.), *Proceedings of the Warner Symposium on Cataclysmic Variables*, Vol. 41 of *New Astronomy Reviews*, Elsevier Science, Amsterdam

Kolb, U. and Stehle, R.: 1996, *Mon. Not. R. Astron. Soc.* **282**, 1454

Lin, D. N. C., Williams, R. E., and Stover, R. J.: 1988, *Astrophys. J.* **327**, 234

Long, K. S. and Gilliland, R.: 1999, *Astrophys. J.* **511**, 916

Lubow, S. H.: 1989, *Astrophys. J.* **340**, 1064

Lubow, S. H. and Shu, F. H.: 1975, *Astrophys. J.* **198**, 383

Mantel, K. H., Barwig, H., Haefner, R., and Schoembs, R.: 1987, *Astrophys. Space. Sci.* **131**, 501

Marcy, G. W., Lindsay, V., and Wilson, K.: 1987, *Publ. Astron. Soc. Pac.* **99**, 385

Marsh, T. R.: 1988, *Mon. Not. R. Astron. Soc.* **231**, 1117

Marsh, T. R.: 1990, *Astrophys. J.* **357**, 621

Marsh, T. R.: 1998, in S. Howell, E. Kuulkers, and W. C. (eds.), *Wild Stars in the Old West*, Vol. 137 of *A. S. P. Conference Series*, p. 236

Marsh, T. R.: 1999, in J. A. Sellwood and J. Goodman (eds.), *Astrophysical Discs - An EC Summer School*, Vol. 160 of *A. S. P. Conference Series*, p. 3

Marsh, T. R.: 2001, in H. Boffin, D. Steeghs, and J. Cuypers (eds.), *Astro-Tomography: An International Workshop on Indirect Imaging*, Lecture Notes in Physics, Springer Verlag

Marsh, T. R. and Dhillon, V. S.: 1997, *Mon. Not. R. Astron. Soc.* **292**, 385

Marsh, T. R. and Horne, K.: 1988, *Mon. Not. R. Astron. Soc.* **235**, 269

Marsh, T. R. and Horne, K.: 1990, *Mon. Not. R. Astron. Soc.* **349**, 593

Marsh, T. R., Horne, K., Schlegel, E. M., Honeycutt, R. K., and Kaitchuck, R. H.: 1990, *Astrophys. J.* **364**, 637

Marsh, T. R., Horne, K., and Shipman, H. L.: 1987, *Mon. Not. R. Astron. Soc.* **225**, 551

Marsh, T. R., Robinson, E. L., and Wood, J. H.: 1994, *Mon. Not. R. Astron. Soc.* **266**, 137

Martin, J. S., Jones, D. H. P., Friend, M. T., and Smith, R. C.: 1989, *Mon. Not. R. Astron. Soc.* **240**, 519

Martinez-Pais, I. G., Giovanelli, F., Rossi, C., and Gaudenzi, S.: 1994, *Astron. Astrophys.* **291**, 455

Martinez-Pais, I. G., Giovanelli, F., Rossi, C., and Gaudenzi, S.: 1996, *Astron. Astrophys.* **308**, 833

Martinez-Pais, I. G., Rodriguez-Gil, P., and Casares, J.: 1999, *Mon. Not. R. Astron. Soc.* **305**, 661

Mattei, J.: 1999, *Observations from the AAVSO International Database*, Private Communication

Mattei, J.: 2000, *Observations from the AAVSO International Database*, Private Communication

McClintock, J. E. and Remillard, R. A.: 1986, *Astrophys. J.* **308**, 110

Morales-Rueda, L.: 2000, *Orbital parameters of GK Persei*, Private Communication

Morales-Rueda, L.: 2001, *Spectrum of SS Cygni in outburst*, Private Communication

Morales-Rueda, L., Still, M. D., and Roche, P.: 1996, *Mon. Not. R. Astron. Soc.* **283**, L58

Mumford, G. S.: 1974, *IBVS* 889

Mumford, G. S.: 1975, *IBVS* 1043

Mumford, G. S.: 1980, *Astron. J.* **85**, 748

Mumford, G. S. and Krzeminski, W.: 1969, *ApJS* **18**, 429

North, R. C., Marsh, T. R., Moran, C. K. J., Kolb, U., Smith, R. C., and Stehle, R.: 2000, *Mon. Not. R. Astron. Soc.* **313**, 383

Oke, J. B. and Greenstein, J. L.: 1977, *Astrophys. J.* **211**, 872

Oke, J. B. and Gunn, J. E.: 1983, *Astrophys. J.* **266**, 713

Orosz, J. A. and Bailyn, C. D.: 1997, *Astrophys. J.* **477**, 876

Orosz, J. A., Bailyn, C. D., McClintock, J. E., and Remillard, R. A.: 1996, *Astrophys. J.* **468**, 380

Orosz, J. A., Bailyn, C. D., Remillard, R. A., McClintock, J. E., and Foltz, C. B.: 1994, *Astrophys. J.* **436**, 848

Osaki, Y.: 1970, *Astrophys. J.* **162**, 621

Paczynski, B.: 1965, *Acta Astron.* **15**, 89

Paczynski, B.: 1971, *Astron. Astrophys. Rev.* **9**, 183

Paczynski, B.: 1976, in P. Eggleton, S. Mitton, and W. J. (eds.), *Structure and Evolution of Close Binary Systems*, Vol. 73 of *International Astronomical Union Symposia*, p. 75, D. Reidel Publishing Co., Dordrecht

Paczynski, B.: 1977, *Astrophys. J.* **216**, 822

Papaloizou, J. and Bath, G.: 1975, *Mon. Not. R. Astron. Soc.* **172**, 339

Persson, S. E.: 1988, *Publ. Astron. Soc. Pac.* **100**, 710

Politano, M.: 1996, *Astrophys. J.* **465**, 338

Pringle, J. E.: 1975, *Mon. Not. R. Astron. Soc.* **170**, 633

Rafanelli, P.: 1979, *Astron. Astrophys.* **76**, 365

Rappaport, S., Joss, P. C., and Webbink, R. F.: 1982, *Astrophys. J.* **254**, 616

Rappaport, S., Verbunt, F., and Joss, P. C.: 1983, *Astrophys. J.* **275**, 713

Rayne, M. W. and Whelan, J. A. J.: 1981, *Mon. Not. R. Astron. Soc.* **196**, 73

Reimers, D., Griffiths, R. F., and Brown, A.: 1988, *Astron. Astrophys.* **193**, 180

Reinsch, K.: 1994, *Astron. Astrophys.* **281**, 108

Remillard, R. A., McClintock, J. E., and Bailyn, C. D.: 1992, *Astrophys. J.* **399**, L145

Remillard, R. A., Orosz, J. A., McClintock, J. E., and Bailyn, C. D.: 1996, *Astrophys. J.* **459**, 226

Ritter, H.: 1986, *The Evolution of Galactic X-ray Binaries*, p. 271, Reidel, Dordrecht

Ritter, H. and Kolb, U.: 1998, *Astron. Astrophys. Suppl. Ser.* **129**, 83

Robinson, E. L.: 1974, *Astrophys. J.* **193**, 191

Robinson, E. L.: 1976, *Astron. Astrophys. Rev.* **14**, 119

Robinson, E. L., Barker, E. S., Cochran, A. L., Cochran, W. D., and Nather, R. E.: 1981, *Astrophys. J.* **251**, 611

Robinson, E. L., Wood, J. H., Bless, R. C., Clemens, J. C., Dolan, J. F., Elliot, J. L., Nelson, M. J., Percival, J. W., Taylor, M. J., van Citters, G. W., and Zhang, E.: 1995, *Astrophys. J.* **443**, 295

Robinson, E. L., Wood, J. H., and Wade, R. A.: 1999, *Astrophys. J.* **514**, 952

Robinson, E. L., Zhang, E. H., and Stover, R. J.: 1986, *Astrophys. J.* **305**, 732

Schneider, D. P. and Young, P.: 1980, *Astrophys. J.* **238**, 946

Shafter, A. W.: 1983, *Ph.D. thesis*, University of California, Los Angeles

Shakura, N. I. and Sunyaev, R. A.: 1973, *Astron. Astrophys.* **24**, 337

Silber, A. D.: 1992, *Ph.D. thesis*, Massachusetts Institute of Technology

Skidmore, W., Welsh, W. F., Wood, J. H., and Stiening, R. F.: 1997, *Mon. Not. R. Astron. Soc.* **288**, 189

Skilling, J. and Bryan, R. K.: 1984, *Mon. Not. R. Astron. Soc.* **211**, 111

Skillman, D. R., Patterson, J., and Thorstensen, J. R.: 1995, *Publ. Astron. Soc. Pac.* **107**, 545

Smak, J.: 1971, *Acta Astron.* **21**, 15

Smak, J.: 1981, *Acta Astron.* **31**, 395

Smak, J.: 1985, *Acta Astron.* **35**, 351

Smak, J.: 1989, *Acta Astron.* **39**, 41

Smith, D., Mateo, M., and Szkody, P.: 1995, *Astron. Astrophys. Suppl. Ser.* **186**, 1003

Smith, D. A. and Dhillon, V. S.: 1998, *Mon. Not. R. Astron. Soc.* **301**, 767

Smith, D. A., Dhillon, V. S., and Marsh, T. R.: 1998, *Mon. Not. R. Astron. Soc.* **296**, 465

Soria, R., Wu, K., and Hunstead, R. W.: 2000, *Astrophys. J.* **539**, 445

Spruit, H. C. and Ritter, H. S.: 1983, *Astron. Astrophys.* **124**, 267

Steeghs, D., Harlaftis, E. T., and Horne, K.: 1997, *Mon. Not. R. Astron. Soc.* **290**, L23

Steeghs, D., Horne, K., Marsh, T. R., and Donati, T. F.: 1996, *Mon. Not. R. Astron. Soc.* **281**, 626

Steining, R. F., Dragovan, M., and Hildebrand, R. H.: 1992, *Publ. Astron. Soc. Pac.* **94**, 672

Stover, R. J.: 1981a, *Astrophys. J.* **249**, 673

Stover, R. J.: 1981b, *Astrophys. J.* **248**, 684

Stover, R. J., Robinson, E. L., and Nather, R. E.: 1981, *Astrophys. J.* **248**, 696

Stover, R. J., Robinson, E. L., Nather, R. E., and Montemayor, T. J.: 1980, *Astrophys. J.* **240**, 597

Szkody, P.: 1976, *Astrophys. J.* **207**, 824

Szkody, P.: 1986, *ApJL* **301**, 29

Szkody, P. and Mateo, M.: 1988, *Publ. Astron. Soc. Pac.* **100**, 1111

Szkody, P., Williams, R. E., Margon, B., Howell, S. B., and Mateo, M.: 1992, *Astrophys. J.* **387**, 357

Tappert, C., Wargau, W. F., Hanuschik, R. W., and Vogt, N.: 1997, *Astron. Astrophys.* **327**, 231

Taylor, C. J., Thorstensen, J. R., and Patterson, J.: 1999, *Publ. Astron. Soc. Pac.*

111, 184

Thorstensen, J. R.: 1986, *Astron. J.* **91**, 940

Thorstensen, J. R., Ringwald, F. A., Wade, R. A., Schmidt, D. G., and Norsworthy, J. E.: 1991, *Astron. J.* **102**, 272

Tonry, J. and Davis, M.: 1979, *Astron. J.* **84**, 1511

van Paradijs, J., Augusteijn, T., and Stehle, R.: 1996, *Astron. Astrophys.* **312**, 93

Verbunt, F.: 1982, *Space Sci. Rev.* **32**, 379

Verbunt, F.: 1984, *Mon. Not. R. Astron. Soc.* **209**, 227

Vogt, N. and Breysacher, J.: 1980, *Astrophys. J.* **235**, 945

Wade, R. A.: 1981, *Astrophys. J.* **246**, 215

Wade, R. A. and Horne, K.: 1988, *Astrophys. J.* **324**, 411

Warner, B.: 1995, *Cataclysmic Variable Stars*, No. 28 in Cambridge Astrophysics Series, Cambridge University Press, Cambridge

Webbink, R. F.: 1990, *Absolute Parameters of Cataclysmic Binaries*, Cambridge University Press, Cambridge

White, J. C., Schlegel, E. M., and Honeycutt, R. K.: 1996, *Astrophys. J.* **456**, 777

Wielen, R.: 1977, *Astron. Astrophys.* **60**, 263

Wielen, R., C., D., Fuchs, B., Jahreiss, H., and Radons, G.: 1992, *The Stellar Populations of Galaxies*, Vol. 149 of *I. A. U. Symposium*, Kluwer, Dordrecht

Williams, R. E.: 1989, *Astron. J.* **97**, 1752

Wolf, S., Barwig, H., Bobinger, A., Mantel, K. H., and Simic, D.: 1998, *Astron. Astrophys.* **332**, 984

Wolf, S., Mantel, K. H., Horne, K., Barwig, H., Schoembs, R., and Baernbantner, O.: 1993, *Astron. Astrophys.* **273**, 160

Wood, J. H. and Crawford, C. S.: 1986, *Mon. Not. R. Astron. Soc.* **222**, 645

Wood, J. H., Horne, K., Berriman, G., Wade, R. A., O'Donoghue, D., and Warner, B.: 1986, *Mon. Not. R. Astron. Soc.* **219**, 629

Wood, J. H., Horne, K., and Vennes, S.: 1992, *Astrophys. J.* **385**, 294

Wood, J. H., Marsh, T., Robinson, E., Steining, R., Horne, K., Stover, R., Schoembs, R., Allen, S., Bond, H., Jones, D., Grauer, A. D., and Ciardullo, R.: 1989, *Mon.*

Not. R. Astron. Soc. **239**, 809

Young, P. and Schneider, D. P.: 1980, *Astron. J.* **238**, 955

Young, P., Schneider, D. P., and Shectman, S. A.: 1981, *Astrophys. J.* **245**, 1035